

**CHARACTERIZATION OF COMMERICALLY AVAILABLE  
CONDUCTIVE FILAMENT AND THEIR  
APPLICATIONS IN SENSORS  
AND ACTUATORS**

by

Fraser Joseph Daniel, B.S.

A Dissertation Presented in Partial Fulfillment  
of the Requirements of the Degree  
Doctor of Philosophy

COLLEGE OF ENGINEERING AND SCIENCE  
LOUISIANA TECH UNIVERSITY

November 2021

LOUISIANA TECH UNIVERSITY

GRADUATE SCHOOL

**August 18, 2021**

Date of dissertation defense

We hereby recommend that the dissertation prepared by

**Fraser Joseph Daniel, B.S.**

entitled **CHARACTERIZATION OF COMMERCIALY AVAILABLE**

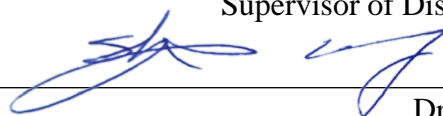
**CONDUCTIVE FILAMENT AND THEIR APPLICATION IN SENSORS AND  
ACTUATORS**

be accepted in partial fulfillment of the requirements for the degree of

**Doctor of Philosophy in Engineering, Micro & Nanoscale Systems Conc.**

Dr. Adarsh Radadia

Supervisor of Dissertation Research



Dr. Shengnian Wang

Head of Molecular Sciences and Nanotechnology

**Doctoral Committee Members:**

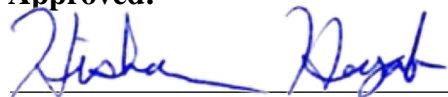
Dr. Xiang Chen

Dr. Leland Weiss

Dr. Hamzeh Bardaweel

Dr. Arden Moore

**Approved:**



Hisham Hegab

Dean of Engineering & Science

**Approved:**



Ramu Ramachandran

Dean of the Graduate School

## ABSTRACT

The primary aim of this study is to contribute to the field of additives that would enable the fabrication of electrical sensors and actuators completely via Material Extrusion based Additive Manufacturing (MEAM). The second aim of the study is to provide the necessary characterization to facilitate the development of applications that predicts electrical part performance. The electrical characterization of two conductive poly-lactic acid (PLA) filaments, namely, c-PLA with carbon black and graphene PLA was performed to study the temperature coefficient of the resistance. Resistivity of carbon black filament was compared to a printed single layer and with that of a cube. The raw and printed c-PLA showed a positive temperature coefficient of resistance ( $\alpha$ ) ranging from  $\sim 0.03$ - $0.01$   $^{\circ}\text{C}^{-1}$  while its counterpart in the study, graphene PLA, did not exhibit significant ( $\alpha$ ). Parts from graphene PLA with multilayer MEAM exhibited a negative  $\alpha$  to a certain temperature before exhibiting positive  $\alpha$ . The resistivity of the printed parts was 300 times higher for c-PLA and 1500 times for graphene PLA. However, no microstructural or chemical compositional changes were observed between the raw filaments and the printed parts. Due to the high  $\alpha$  of the c-PLA, it was deemed as the better material for constructing electro thermal sensors and actuators using MEAM.

First, c-PLA was used to fabricate and package a completely 3D printed flow meter that operates on the principle of Joule heating and hotwire anemometry. When the designed flowmeter was simulated using a finite element package, a flow sensitivity of

-2.33  $\Omega$  sccm<sup>-1</sup> and a relative change in resistivity of 0.036 sccm<sup>-1</sup> was expected. For an operating voltage of 12-15 V, the experimental results showed a flow sensitivity within the range of 0.014-0.032 sccm<sup>-1</sup> and the relative change in resistivity ranged from 0.039 – 0.065 sccm<sup>-1</sup>. Thus, a completely 3D printed flowmeter was demonstrated. Second, using the same principle of Joule heating, an actuator inspired from MEMS chevron grippers was designed, simulated, and fabricated. Simulation showed the feasibility of the structure and further predicted a displacement of a few hundred microns with a potential as low as 3 V with a cooling time as little less than 120 seconds. Experimentally, a displacement of 120.04, 97.05, and 88.96  $\mu\text{m}$  were achieved in 15, 10, and 5 seconds with actuation potentials of 12.7, 13.8, and 17.9 V, respectively. As predicted by the simulation results, it took longer for the gripper to cool (close to 180 seconds) when compared to actuation times.

During the above studies, we discovered the printing parameters altered the part resistance. Our final study examined how extrusion temperature and printing speed affects the impedance of the MEAM printed parts. Further, anisotropy in the impedance was observed and the influence of the interface to it was examined. From the experimental results, the anisotropy was quantified with a Z/F ratio and was found to be nearly constant,  $\sim 2.15 \pm 0.23$ . Impedance scaling with the number of interfaces was measured and showed conclusively that the interlayer bonding was the sole source for the observed Z/F ratio. Scanning electron microscope images shows the absence of air gaps at the interface, and energy dispersion spectroscopy shows the absence of oxidation at the interface. By investigating the role of print parameters and scaling of impedance with

interfaces, a framework to model and predict electrical behavior of electro thermal sensors and actuators made via MEAM can be realized.

## **APPROVAL FOR SCHOLARLY DISSEMINATION**

The author grants to the Prescott Memorial Library of Louisiana Tech University the right to reproduce, by appropriate methods, upon request, any or all portions of this Dissertation. It is understood that “proper request” consists of the agreement, on the part of the requesting party, that said reproduction is for his personal use and that subsequent reproduction will not occur without written approval of the author of this Dissertation. Further, any portions of the Dissertation used in books, papers, and other works must be appropriately referenced to this Dissertation.

Finally, the author of this Dissertation reserves the right to publish freely, in the literature, at any time, any or all portions of this Dissertation.

Author: Fraser Joseph Daniel

Date: 18.08.2021

## **DEDICATION**

To my loving father, Joseph Daniel;

To my caring mother, Sumangala Daniel;

To my creative genius brother, Joshua Daniel;

To my family away from home, the Swaffords and Lotts.

## TABLE OF CONTENTS

ABSTRACT.....	iii
APPROVAL FOR SCHOLARLY DISSEMINATION .....	vi
DEDICATION .....	vii
LIST OF FIGURES .....	xi
LIST OF TABLES .....	xvii
ACKNOWLEDGMENTS .....	xviii
CHAPTER 1 INTRODUCTION .....	1
1.1    Background and Motivation .....	1
1.1.1    Statement of Problem.....	1
1.2    Research Objectives.....	2
1.2.1    Identifying Suitable Conductive Filaments for Electronic Application .....	2
1.2.2    Electrical Characterization for Explaining Anisotropy and Studying the Role of Interfaces .....	3
1.2.3    Application of Conductive Polylactic Acid (c-PLA): Flowmeter using Anemometer Wire.....	4
1.2.4    Application of Conductive Polylactic Acid (c-PLA): MEAM Chevron based Gripper .....	4
1.3    Structure of the Dissertation .....	5
CHAPTER 2 TEMPERATURE DEPENDENT ELECTRICAL RESISTANCE OF CONDUCTIVE POLYLACTIC ACID FOR MATERIAL EXTRUSION BASED ADDITIVE MANUFACTURING .....	6
2.1    Introduction.....	6
2.2    Methodology and Materials .....	8



2.2.1	Sample Design and Fabrication using MEAM .....	8
2.2.2	Characterization Setup .....	8
2.2.3	SEM and Raman Spectroscopy .....	9
2.3	Results and Discussion .....	9
2.4	Conclusion .....	20
CHAPTER 3 INFLUENCE OF INTERFACE ON THE ELECTRICAL PERFORMANCE OF MEAM STRUCTURES .....		22
3.1	Introduction.....	22
3.2	Methodology .....	26
3.2.1	Sample Preparation .....	26
3.2.1	Electrical Impedance Spectroscopy .....	26
3.2.2	Microscope Imaging .....	28
3.2.3	Modeling and Simulation.....	28
3.3	Results and Discussion .....	28
3.3.1	Impact of Printer Settings on Impedance.....	29
3.3.2	Comparing Impedance in F- and Z- Direction.....	36
3.3.3	Understanding the Structure of the Interface .....	41
3.4	Conclusion .....	45
CHAPTER 4 HOT WIRE ANEMOMETER MADE COMPLETELY VIA MEAM .....		47
4.1	Introduction.....	47
4.2	Material and Methodology.....	48
4.2.1	Modeling and Simulation.....	48
4.2.2	MEAM for Empirical Experimentation .....	49
4.2.3	Thermal Imaging.....	50
4.2.4	Flow Calibration .....	50

4.3	Results and Discussion .....	51
4.3.1	Multiphysics Simulation .....	51
4.3.2	Flowmeter Experimental Investigation .....	54
4.4	Conclusion .....	66
CHAPTER 5 CHARACTERIZATION OF AN ELECTROTHERMAL CHEVRON GRIPPER FABRICATED BY EXTRUSION-BASED ADDITIVE MANUFACTURING .....		67
5.1	Introduction.....	67
5.2	Methodology .....	70
5.2.1	Modeling and Simulation.....	70
5.2.2	Fabrication by MEAM Sample .....	71
5.2.3	Electrical Actuation by Source Measurement Unit (SMU) .....	71
5.2.4	Thermal Imaging.....	72
5.2.5	Laser Doppler Vibrometer .....	73
5.3	Results and Discussion .....	74
5.3.1	Multiphysics: Steady-State Analysis .....	74
5.3.2	Multiphysics: Transient Analysis .....	76
5.3.3	Experimental Analysis: Proof of Concept .....	76
5.3.4	Hysteresis Study.....	80
5.3.1	Application.....	83
5.4	Conclusion .....	84
CHAPTER 6 CONCLUSIONS AND FUTURE WORK.....		87
6.1	Conclusions.....	87
6.2	Future Work Recommendation.....	89
Bibliography .....		91

## LIST OF FIGURES

<b>Figure 2-1:</b> Micro-Raman spectrum for (a) PLA-carbon black filament (b) PLA-graphene filament as-recieved and after MEAM.....	10
<b>Figure 2-2:</b> SEM images of the PLA-graphene before (a-c) and after MEAM (d-f).....	10
<b>Figure 2-3:</b> SEM images of the PLA-carbon black before (a-c) and after MEAM (d-f). 11	
<b>Figure 2-4:</b> Characterization of PLA-graphene composite filament as-received (a, b), and after MEAM (c, d). (a) and (c) indicate the resistance of a 7.5 cm long filament and printed wire measured at temperatures from 25 °C to 45 °C with 5 °C increments. Red triangles and open diamonds indicate the results form temperature ramps from 25 °C to 45 °C. Blue circles and open squares indicate results from cool down from 45 °C to 25 °C. (b) and (d) are differential scanning calorimetry (DSC) measurements on the PLA-graphene raw filaments and printed wire, respectively.....	12
<b>Figure 2-5:</b> Characterization of the raw PLA-carbon black filament (a-c), and printed PLA-carbon black wire (d-f). (a) and (d) indicate the resistance of a 7.5 cm long filament and printed wire measured at temperatures from 25 °C to 45 °C with 5 °C increments in a cyclical manner. Blue triangles indicate results for temperature ramp from 25 °C to 45 °C. Open circles indicate the results of ramp-down from 45 °C to 25 °C. Considering the measurements at 25 °C as the reference, fractional change in resistance is plotted against the change in temperature in (b) and (e). The slope of this graph (b and e) gives the temperature coefficient of resistance. (c) and (f) are DSC measurements on the raw PLA-carbon black filament and printed PLA-carbon wire, respectively. ....	14
<b>Figure 2-6:</b> Temperature-dependent behavior of resistance for a 4 mm, and a 5 mm thick 3D printed solid blocks using the PLA-graphene filament. The panel of graphs represents the results from different temperature sweeps between 25 °C to 45 °C; the arrow in the graph indicates the direction of the temperature sweep. The graphs are arranged left-to-right in the sequence the temperature sweeps were carried out. The vertical dash line indicates when a one-hour break was taken between experiments. ....	16
<b>Figure 2-7:</b> Temperature-dependent behavior of resistance for a 4 mm, and a 5 mm thick 3D printed solid blocks using the PLA-carbon black filament. The panel of graphs represents results from different temperature sweeps between 25 °C to 45 °C; the arrow in the graph indicates the direction of temperature sweep. The graphs are arranged left-to-right in the sequence the temperature sweeps were carried out. The vertical dash line indicates when an hour-break was taken between experiments. ....	18

- Figure 3-1:** The representation of the interface as the intersection of the subsequent layer deposition during the MEAM process. .... 23
- Figure 3-2:** (a) Example of hollow box, a four-wall structure, printed for this research with a layer thickness of 0.2 mm. Samples, 13 mm x 13 mm, were trimmed from the walls prior to sputtering Au. (b) Z-specimen with approximately 30 bond interfaces between the two gold coated areas. The blue arrow points the direction of the fibers. (c) F-specimen. The gold electrodes patterned perpendicularly in comparison to Z-specimen. (d) Sample for probing single bond interface. .... 27
- Figure 3-3:** (a) Equally spaced jig with razor blades to cut the wall, 39 mm x 39 mm, into smaller samples, 13 mm x 13 mm. (b) Jig with twines to mask a single bond interface during sputtering coating of the sample with a 50 nm gold layer. .... 27
- Figure 3-4:** (a) Sample cross-section images of the 3D printed samples in the F-direction via optical microscopy. (b) Example of the processed cross-section obtained via thresholding in ImageJ. .... 35
- Figure 3-5:** Plot of impedance obtained with F-specimen against A/L for the samples. The red circle indicates data points corresponding to low extrusion temperature. The blue circle indicates data points corresponding to medium extrusion temperature. Data represented from 3 samples for each of the 12 printing conditions, and 3 images from each sample were analyzed using ImageJ. Error bars represent standard deviation. .... 35
- Figure 3-6:** The ratio of impedance measured between Z-specimen and F-specimen plot against print parameters. Individual impedance data is shown in **Figure 3-2**. The error bars were calculated in Python using ‘uncertainties’ package. Specimen printed at 750 mm/min (low), 1000 mm/min (med), 1500 mm/min (med), or 2000 mm/min (high), and with a nozzle temperature of 190 °C (high), 210 °C (med), or 230 °C (high). .... 36
- Figure 3-7:** Finite element analysis of the sample geometry recreated using microscopy images of the sample cross-section. (a) and (b) show electric potential distribution when the sample was biased along the F- and Z- directions, respectively, and (c) and (d) show respective normalized current density at the sample cross-section containing bond interfaces. The structure results in a resistance of ~50 Ohms in both F- and Z- directions. .... 38
- Figure 3-8:** Scaling of impedance with several bond interfaces. In the legend, HT stands for high extrusion temperature 230 °C, LT for low extrusion temperature 190 °C, HS for high print speed 2000 mm/min, and LS for low print speed 750 mm/min. Vertical and horizontal error bars indicate standard deviation in impedance recorded and the number of interfaces probed, respectively, over three independent trials for three samples in each case. .... 43

**Figure 3-9:** Scanning electron microscope images of the interface obtained after liquid nitrogen-assisted fracturing of a) a high temperature, high speed sample, and b) a low temperature, low speed sample. .... 44

**Figure 3-10:** Studying the interface to identify surfactants (a) EDS spectrum of the carbon black doped PLA filament. (b) EDS line across the interface for a high temperature, high speed sample. .... 45

**Figure 4-1:** Steady-state simulation of the flow sensor design. (a) Sensor design simulated in COMSOL with the sensor consisting of ABS and c-PLA domains, surrounded by Air, and nitrogen flowing through the conduit. (b) The steady-state temperature distribution along the horizontal cross-section of the sensor with a 3.9 V applied across the sensor element and a 10 sccm of nitrogen flowing through the conduit. (c) A similar steady-state solution with 100 sccm of nitrogen flow. (d) The relative change in sensor wire temperature obtained as a function of the flow rate at different bias (3.9 V– red dots, 3.2 V– blue dots, and 2.5 V– green dots) applied across the sensor element. (e) The corresponding relative change in sensor resistance obtained at different flow rates. (f) The resulting fluid temperature at the outlet as a function of the flow rate and operational voltage. The dashed lines in (d-f) indicate a linear regression of the data with slope value indicated by text in respective color. .... 52

**Figure 4-2:** Transient simulation of the flow sensor. (a) The sensor core temperature and (b) the sensor resistance as a function of time for different operational voltages (3.3 V – red, 3.5 V – blue, 3.7 V – green, 3.9 V – orange, 4.1 V – magenta) and a fixed flow rate of 20 sccm. (c) The sensor core temperature (in blue) and sensor resistance (in red) at 10 s plot as a function of operation voltage. (d) The sensor core temperature and (e) the sensor resistance as a function of time for varying flow rates (20 sccm – red, 40 sccm – blue, 60 sccm – green, 80 sccm – orange, 100 sccm – magenta) and a fixed operational voltage of 3.9 V. (f) The sensor core temperature (in blue) and sensor resistance (in red) obtained at 10 s plot as a function of the flow rate. The dashed lines in (c and f) indicate a linear regression of the data with slope value indicated by text in respective color. .... 53

**Figure 4-3:** A completely 3D printed flow sensor. (a) Model parts that were imported into the 3D printer software (Simplify 3D). The non-conductive sensor top (A) contains a trench, 1 mm wide and 0.7 mm deep running along the length on the bottom face. The conductive sensing element (B) consists of a 1x1 sq. mm hot-wire. The non-conductive sensor bottom (C) also consists of a trench (1 mm wide and 0.3 mm deep). (b) 3D printing the sensor with MakerGear M2 V4 Rev. E with the left extruder printing cPLA and the right extruder printing ABS. The raft at the bottom ensured better adhesion to the print bed. (c) Completely 3D printed flow sensor alongside a US quarter. .... 54

**Figure 4-4:** Thermal image observing the Joule heating of the flow sensor. (a) Half printed sensor with stainless steel electrodes providing electrical contact as pointed by the red squares. (b) Setup for thermal imaging with the FLIR A325sc thermal camera clamped on a tripod pointed to the half-printed flow sensor. The source-measurement unit (SMU) was used to supply bias and record the current across the sensing element. Image capture and analysis of thermal data was performed on a portable computer. (c) Resistance as a function of time shows that the resistance steadies out in less than a minute. Thermal image obtained (d) 1 minute, and (e) 11 minutes. (f) A proof-of-concept sensing shown notes the resistance while air was blown at specific time points..... 55

**Figure 4-5:** Flow sensing with the 3D printed sensor 1 at 12 V. (a) The current passing through the sensor during warm-up/stabilization with no flow and when the flow is stepped up to 100 sccm. (b) The relative change in sensor resistance recorded as a function of the flow rate from three different step-up trials (1st in blue circle, 2nd trial green triangle and 3rd trial in red square). The values used in the graph were obtained 45 s after the change in flow. (c) The current passing through the sensor during the stabilization phase with no flow and when the flow is stepped down from 100 sccm to 20 sccm. (d) The relative change in sensor resistance recorded as a function of flow rate from three different step-down trials (1st in blue circle, 2nd trial green triangle and 3rd trial in red square). Data provided in (a-d) was obtained using sensor 1. Similar data for sensors 2 is shown in **Figure 4-7** and **Figure 4-8**. .... 58

**Figure 4-6:** Flow sensing with the 3D printed sensor 1 at 15 V. (a) The current passing through the sensor during warm-up/stabilization with no flow and when the flow is stepped up to 100 sccm. (b) The relative change in sensor resistance recorded as a function of the flow rate from three different step-up trials (1st in blue circle, 2nd trial green triangle and 3rd trial in red square). The values used in the graph were obtained 45 s after the change in flow. (c) The current passing through the sensor during the stabilization phase with no flow and when the flow is stepped down from 100 sccm to 20 sccm. (d) The relative change in sensor resistance recorded as a function of the flow rate from three different step-down trials (1st in blue circle, 2nd trial green triangle and 3rd trial in red square). Data provided in (a-d) was obtained using sensor 1..... 59

**Figure 4-7:** Flow sensing with the 3D printed sensor 2 at 12 V. .... 60

**Figure 4-8:** Flow sensing with the 3D printed sensor 2 at 15 V. .... 60

**Figure 4-9:** King's law relationship for the experimental value and the projected fitting value demonstrated..... 62

**Figure 5-1:** Gripper design and measurement setup. (a) Design and dimensions of the gripper; the grey colored parts were printed with c-PLA and the blue colored parts with ABS. The whole sample is ~ 6.6 mm tall and 3.4 mm wide. (b) A 3D printed electric gripper alongside a U.S. quarter dollar coin. The electrical contacts were achieved via nickel paint and soldering. (c) Test setup consisting of an SMU, laser Doppler vibrometer and a thermal camera was used to study the gripper actuation and recovery. .... 73

**Figure 5-2:** Gripper actuation demonstrated with steady-state solution. (a) Distribution of current density (A/m<sup>2</sup>) and (b) temperature (°C) across the gripper with the resistivity of c-PLA set to 1.8  $\Omega$ -cm and an actuation voltage of 4.5 V. The arm movement is exaggerated 10x to aid visualization. (c) The maximum temperature achieved with variation in bias applied across the gripper. (d) Maximum displacement achieved with variation in bias applied across the gripper. The different curves in (c) and (d) represent solutions when the resistivity of c-PLA was set to 1  $\Omega$ -cm – blue, 1.8  $\Omega$ -cm – brown, 6  $\Omega$ -cm – orange, 11  $\Omega$ -cm – grey, 16  $\Omega$ -cm – yellow, 21  $\Omega$ -cm – light blue, 26  $\Omega$ -cm – green, or 31  $\Omega$ -cm – navy blue. .... 75

**Figure 5-3:** Transient simulation results for maximum temperature and displacement: (a) The maximum temperature in the chevrons, and (b) the tip displacement plot against time from when the potential was applied across the gripper. For (a) and (b), 5 V – orange, 6 V – dark grey, 7 V – brown, 8 V – navy blue, 9 V – green, 10 V – yellow, 11 V – light blue, 12 V – grey, 13 V – light orange, and 14 V – light grey. (c) The maximum temperature and (d) tip displacement plot against time from when the potential was turned off across the gripper after being heated to 45 °C using different voltages. For (c) and (d), 5V – orange, 6V – grey, 7V – yellow, 8V – blue, 9V – green, 10V – navy blue. Resistivity of c-PLA was set to 1.8  $\Omega$ -cm at 300 K. .... 77

**Figure 5-4:** Displacement and temperature curve of the actuator (S1). (a) Tip displacement and (d) maximum temperature in the chevrons recorded when gripper was actuated using 12.7 V to achieve a response time of 15 s thrice (blue). Similarly, (b) tip displacement and (e) maximum temperature was obtained using 13.8 V to achieve a response time of 10 s (orange), and (c) tip displacement and (f) maximum temperature was obtained using 17.9 V to achieve a response time of 5 s (green). .... 79

**Figure 5-5:** Temperature distribution at 45 °C for S3 with (a) 11.5 V, (b) 13.0 V, and (c) 17.5 V. .... 80

**Figure 5-6:** Maximum temperature overshoot observed for S3 with (a) 11.5 V, (b) 13.0 V, and (c) 17.5 V. Presented video frame observed right before turning off the power supply. .... 80

- Figure 5-7:** Hysteresis in electro thermal actuation. Displacement of single arm is plotted against the maximum temperature observed in the chevron of actuators (a) S1, (b) S2, and (c) S3. The solid circles denote the actuation (heating or opening) of the tweezer. The red, green, and yellow markers denote data when the tweezer was opened with response times of 15, 10, and 5 s, respectively. The corresponding voltages are annotated in the legend. The crosses denote the recovery (cooling or closing) of the tweezer for the corresponding actuation voltage and response times. The black arrow points to the trend in the actuation cycle and the red arrows point to the trend during the cooling cycle..... 81
- Figure 5-8:** Linear trends in actuation for sensor S1. a) actuation in 15 s with a potential of 12.7 V, b) actuation in 10 s with a potential of 13.8 V, and c) actuation in 5 s with a potential of 17.9 V..... 81
- Figure 5-9:** Linear trends in actuation for sensor S2. a) actuation in 15 s with a potential of 12.3 V, b) actuation in 10 s with a potential of 14.6 V, and c) actuation in 5 s with a potential of 19.7 V..... 82
- Figure 5-10:** Linear trends in actuation for sensor S3. a) actuation in 15 s with a potential of 11.5 V, b) actuation in 10 s with a potential of 13.0 V, c) actuation in 5 s with a potential of 17.5 V. .... 82
- Figure 5-11:** Thermal imaging of sample for S3 (a) at the beginning of the cooling phase, (b) 60 s into the cooling phase, and (c) 120 s into the cooling phase. .... 83
- Figure 5-12:** Displacement and temperature plotted against resistance for S1 (a), S2 (b), and S3 (c). Blue diamond represents displacement and the red crosses represent temperature. .... 84



## LIST OF TABLES

<b>Table 3-1:</b> The p-values comparing the impedance when measured in the F-direction from the samples printed with varying extrusion temperatures. The p-values were calculated using an unpaired unequal variance t-test and represent probability for the hypothesis that the impedance due to varying extrusion temperatures are different. A p-value > 0.05 indicates the hypothesis is nullified. ....	30
<b>Table 3-2:</b> The p-values comparing the impedance when measured in the Z-direction from samples printed with varying extrusion temperatures. The p-values were calculated using an unpaired unequal variance t-test and represent probability for the hypothesis that the impedance due to varying extrusion temperatures are different. A p-value > 0.05 indicates the hypothesis is nullified. ....	30
<b>Table 3-3:</b> The p-values comparing the impedance when measured in the F-direction from the samples printed with varying speeds. The p-values were calculated using an unpaired unequal variance t-test and represent probability for the hypothesis that the impedance due to varying print speeds are different. A p-value > 0.05 indicates the hypothesis is nullified. ....	31
<b>Table 3-4:</b> The p-values comparing the impedance when measured in the Z-direction from the samples printed with varying speed. The p-values were calculated using an unpaired unequal variance t-test and represent probability for the hypothesis that the impedance due to varying print speeds are different. A p-value > 0.05 indicates the hypothesis is nullified. ....	32
<b>Table 3-5:</b> The Z/F ratio of Zhang <i>et al.</i> work with variation in raster width with variation and their corresponding standard deviation. ....	40
<b>Table 3-6:</b> The Z/F ratio of Zhang <i>et al.</i> work with variation in layer height with variation and their corresponding standard deviation. ....	40
<b>Table 4-1:</b> Flow sensitivity recorded for sensors 1-3 operate with 12 V or 15 V bias. Values represent average and standard deviation from results recorded in three different ramp-up or ramp-down trials. The p-values were calculated using an unpaired unequal variance t-test and represent the probability for the hypothesis that the flow sensitivities for the ramp-up and ramp-down trials are different. A p-value > 0.05 indicates the hypothesis is nullified. ....	65

## **ACKNOWLEDGMENTS**

First, I want to thank God for His Grace, Love, and Provision during my time at Louisiana Tech. I am very grateful for my parents who have constantly provided me with financial, emotional, and moral support for my work. They have genuinely put my interest above theirs for my well-being in leading a very sacrificial life. Without their sacrifice and hard work through all these years, I would not be the person that I am today. I am extremely indebted to Dr. Radadia for always pushing me beyond what was expected and encouraging me to strive for excellence. Throughout my time in his lab, he has worked so hard to make sure that my work was nothing short of perfection. I would also like to thank Davis Bailey who deserves an honorary doctorate for the experience and knowledge he has of the lab facilities. He made himself available for my experiments and provided me with excellent insights and advice on running tests and various analyses.

# **CHAPTER 1**

## **INTRODUCTION**

### **1.1 Background and Motivation**

#### **1.1.1 Statement of Problem**

During the past decades, material extrusion based additive manufacturing (MEAM) has gone from being a prototyping technology to a manufacturing technology because of the growing resolution of printers and wide range of novel printing material. Specifically, MEAM has immense potential as an alternate for manufacturing sensors and actuators. Reasons for the crossover of MEAM from prototyping to manufacturing are cost-efficiency, ease of fabrication, and environmental friendliness. According to the UN, close to 50 million tons of electronic components that are not biodegradable are produced every year; if the current rate continues, 120 million tons of non-biodegradable electronic waste will be produced in 2050 [1]. With the availability of biodegradable conductive filaments, MEAM stands as a viable alternative to manufacturing conventional electronics. In addition to being environmentally friendly, complete MEAM sensors and actuators can be manufactured on-demand for applications in settings like universities around the world, especially in places that are rural and lack resources for conventional electronic fabrication.

Despite the immense potential and advantage of MEAM fabrication over traditional electronics, there is inadequate study on the development of complete MEAM sensors and actuators. MEAM has been demonstrated to fabricate sensors, however, primarily for packaging purposes utilizing electronic components from the market. So far, MEAM has not demonstrated complete sensors. To fabricate sensors and actuators completely through MEAM involves using electrically conductive materials. Further, it becomes an important and interesting challenge to be able to predict part performance before it is printed. Currently, part performance is only tested after fabrication, which is efficient because of the expense of time and money involved. The existing frameworks are only available for predicting mechanical part performance; they are also computationally intense. As far as we are aware, currently there exists no framework to predict electrical performance of printed structures that is fast and computationally efficient.

## **1.2 Research Objectives**

The research objectives of this work can be summarized as follows: electrical characterization of commercially available filaments, fabrication of electro thermal sensors and actuators completely via MEAM, and to develop a framework to predict electrical performance of MEAM parts before printing them based on the print parameters.

### **1.2.1 Identifying Suitable Conductive Filaments for Electronic Application**

In the last few decades, there has been wide scale testing and adoption of additive manufacturing in areas like aerospace, biomedical, automobile, electronics, robotics, and microfluidics. With a wide selection of custom made and commercially available

filaments, MEAM technique has been employed for mechanical and electrical applications. Using electrically conductive filaments—circuits, sensors, and actuators potentially can be 3D printed. Our goal was to choose two electrically conductive filaments and characterize the electrical properties to measure the temperature coefficient of resistance (TCR). Conductive filament with TCR comparable to metals can be used to achieve electro thermal sensors and actuators completely via MEAM that operate on the principal of Joule heating. In the study, a printed wire and a printed block using conductive poly-lactic acid (c-PLA) and graphene PLA are characterized.

### 1.2.2 Electrical Characterization for Explaining Anisotropy and Studying the Role of Interfaces

As MEAM technology moves from prototyping to manufacturing, prediction of part performance is of paramount importance. Currently, part performance—be it mechanical or electrical—is determined by trial-and-error methods, costing money and time. The existing literature shows a correlation between print settings and part performance. Hence, being able to predict the performance based on print setting can reduce the cost and time involved in MEAM fabrication. Available techniques to predict part performance requires high computational power and processing time. The first step towards building a reliable and computationally less demanding system is to characterize the part performance of an electrically conductive structure. In our study, our goal is to characterize electrical impedance (or resistance), examine the anisotropy, and the role of interfaces in causing anisotropy.

### 1.2.3 Application of Conductive Polylactic Acid (c-PLA): Flowmeter using Anemometer Wire

Hot-wire anemometry is conventionally done with metal wires that change the resistance of the hot-wire, either through cooling or heating, to measure the flow of gases. Though MEAM has been used to fabricate electric circuits, they have not been used to print sensors. For the most part, sensors that use MEAM only do so to create a package for providing enclosure to the electronic sensor. The cost of producing such packaging is drastically reduced by 3D printing it. However, the cost can be further reduced by fabricating even the sensor using conductive filament. The goal here is to fabricate a complete MEAM hot-wire anemometer to measure the flow of nitrogen gas and calibrate the variation of resistance of the hot-wire with respect to the nitrogen flow.

### 1.2.4 Application of Conductive Polylactic Acid (c-PLA): MEAM Chevron based Gripper

Soft robotics is an emerging field where robotic actions are achieved through mimicking biological systems. It has become a major field of research interest because of the tender, softer materials that it uses, especially where invasive movements are required. There are places, however, where there is a compromise between tender parts and retaining the rigid aspects of robotic parts. The existing soft robotics uses a mechanism that requires air, light, or heat to actuate, resulting in wire-intensive systems. On the other hand, there is a wide pool of research in MEMS actuators that are electrothermally actuated. The goal of this work is to produce a robot end effector that is MEMS inspired, completely MEAM fabricated, and strikes a balance between soft and rigid aspects of conventional robotics.

### **1.3 Structure of the Dissertation**

The dissertation is organized thematically. The following two initial chapters discuss the various characterizations that were performed in filaments and MEAM printed structures. The last two chapters show the studies done on fabricating sensors and actuators via MEAM that were developed as a product of these characterizations.

Chapter 2 discusses the electrical characterization of two electrically conductive thermoplastic filaments, namely, graphene-PLA and carbon black PLA (c-PLA). The temperature coefficient of resistance is measured to determine the filament most suitable for electronic application.

Chapter 3 studies the impedance of a MEAM wall printed along and the occurring anisotropy. Using simulation and experimental data, the role of interfaces is studied. By measuring the p-values between resistance and the two varying factors, namely, temperature and printing speed, the relationship between them is established.

Chapter 4 exhibits the development of a hot-wire anemometry completely via MEAM that measures the flow of nitrogen gas through a small channel. c-PLA is used as the hot-wire element which is heated up by Joule heating.

Chapter 5 demonstrates a robot end effector, which is designed after a MEMS chevron using MEAM techniques. Joule heating to expand the arm of the gripper actuates the device. The operational voltage ranges are predicted using simulation. Hysteresis of the actuator over many trials is also studied.

Chapter 6 summarizes the major findings from the entire work, its contribution to the existing body of work in the field in which the studies are undertaken and discusses the future direction in which the research can lead.

## **CHAPTER 2**

# **TEMPERATURE DEPENDENT ELECTRICAL RESISTANCE OF CONDUCTIVE POLYLACTIC ACID FOR MATERIAL EXTRUSION BASED ADDITIVE MANUFACTURING**

### **2.1 Introduction**

Over the last decade, material extrusion based additive manufacturing (MEAM), or more commonly referred to as 3D printing, has been revolutionizing the way 3D objects are being prototyped and fabricated. These scale from a few centimeters to several meters [2-4]. MEAM is finding applications in electronics [5-10], RF electronics [11-14], microfluidics [15-19], medical [20-25], and robotics [26-28]. The expansion of MEAM has been possible because it is cost-effective for prototyping or producing parts in small scale, and most importantly, the availability of a wide range of thermoplastic filaments with different textures, colors, electrical and mechanical properties. Our research group is investigating the fabrication of a variety of sensors via MEAM; specifically, sensors that leverage outstanding temperature-dependent electrical properties, like resistance thermometers, thermal conductivity detectors, and flow meters. The findings on the temperature dependent resistance of commercially available conductive thermoplastic filaments for MEAM are reported.

Conductive plastic composites of a wide variety have been reported previously; however, very few have been translated for application to MEAM. Thus, lately there have



been some efforts to prepare conductive plastic composites specifically for MEAM to print electrical circuits and sensors. Wei *et al.* (2015) prepared and characterized electrical properties of conductive acrylonitrile butadiene styrene (ABS) filament doped with varying amounts of graphene and its application to MEAM; their work presented a best conductivity of  $\sim 105$  ohm-cm at 5.6 wt% graphene content [29]. To make an economically viable conductive filament, Wei *et al.* (2017) prepared and characterized electrical properties of conductive polypropylene filaments doped with varying concentration of carbon black and demonstrated its application to build modular 2D and 3D printed circuits including a temperature sensor [30].

Despite the large-scale efforts to make several electrically conductive MEAM-compatible materials, presently, there are only two commercially available MEAM filaments, but their electrical properties in as-received filament form and 3D printed form have not been characterized to utilize them to design and fabricate sensors and electronics. This characterization is significant because when 3D printing is used for fabricating devices, the effect of extrusion on the filament becomes vital. The manufacturer information on the properties might not apply after extrusion.

In this chapter, the temperature dependence of resistance for commercially available PLA-graphene and PLA-carbon black MEAM filaments is reported. The difference in behavior of the filaments as received and after 3D printing a wire and a solid block was studied.

## 2.2 Methodology and Materials

### 2.2.1 Sample Design and Fabrication using MEAM

Two types of features were printed: a 0.3 mm thick wire and rectangular blocks, 1"x1" (l x w) with thicknesses of 2, 3, 4, 5, and 7 mm. A CAD file was created using Autodesk Fusion 360 and printed using a MakerGear M2 (version 4) MEAM tool. PLA-carbon black was obtained from Proto-pasta Inc., and PLA-graphene was obtained from Graphene 3D Lab Inc. Nozzles of 0.35 mm for PLA-carbon black and 0.5 mm for PLA-graphene was found to be best suited. The extruder and the platform, while printing, were maintained at  $220 \pm 5$  °C and 70 °C, respectively. The platform was a borosilicate glass covered with painter's tape. Simplify 3D, a slicer software, was utilized to print rectangular blocks with 100% infill, no floor or ceiling, 0.25 mm thick layers, single perimeter, and rectangular pattern.

### 2.2.2 Characterization Setup

Rectangular block samples were sandwiched between two 1 mil-thick, 2" x 1" copper electrodes and microscope slides, which were held together using anodized binder clips. The samples were placed inside a forced convection oven to regulate temperature within  $\pm 1$  °C. The copper electrodes were connected to a portable electrochemical analyzer (Ivium CompactStat). A 1 mV sinusoidal signal was applied with frequency ranging from 100 Hz to 10 kHz. The native data collection software, Iviumsoft® was used to fit the impedance and phase data to an equivalent circuit. An R-L circuit fits the data the best as opposed to an R-C or R||C circuit. The inductance was found to be in range of  $10^{-9}$  H.

### 2.2.3 SEM and Raman Spectroscopy

SEM was performed using a Hitachi field-emission S-4800 microscope. Charging was minimized using an extraction voltage of 3 kV. Micro-Raman was performed using a Horiba Xplora™ Plus confocal Raman microscope equipped with a 532 nm laser, 1200 gratings/mm, a slit size of 200 microns and a hole size of 300 microns. The optical bench was aligned to the 520 cm<sup>-1</sup> peak for silicon. With a 10x objective, micro-Raman was obtained from a spot size of 10 microns.

## 2.3 Results and Discussion

Micro-Raman spectra for the conductive filaments as-received and after MEAM are shown in **Figure 2-1**. In **Figure 2-1a**, the Raman spectra for PLA-carbon black filament as-received and after MEAM shows the typical D (internally phonon and defect scattering) and G (primary in-plane vibration) bands at 1350 cm<sup>-1</sup> and 1573 cm<sup>-1</sup>, respectively, for a graphitic system. The 2D band (a second-order overtone of a different in-plane vibration), which is usually observed around 2690 cm<sup>-1</sup>, was relatively weak. In **Figure 2-1b**, the Raman spectra for PLA-graphene filament as-received and after MEAM both show the typical D (1350 cm<sup>-1</sup>), G (1573 cm<sup>-1</sup>) and 2D bands (2690 cm<sup>-1</sup>) associated with graphene. The intensity of the D-band indicates extensive damage of the graphene plane and the ratio of G-peak to 2D-peak varied between 0.17 to 0.2, which confirms the presence of few-layer graphene [31, 32]. A major change in the micro-Raman spectra for the conductive PLA filaments before and after MEAM was not observed. The SEM images of PLA-graphene and PLA-carbon black filament as-received and after MEAM are shown in **Figure 2-2** and **Figure 2-3**, respectively.

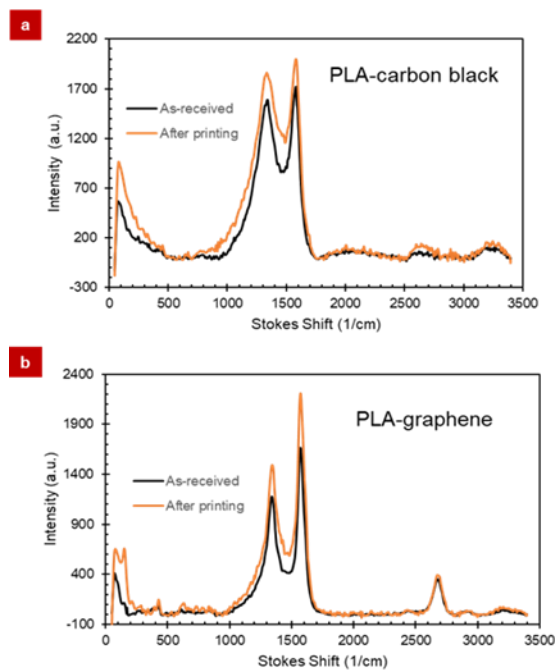


**Figure 2-1:** Micro-Raman spectrum for (a) PLA-carbon black filament (b) PLA-graphene filament as-received and after MEAM

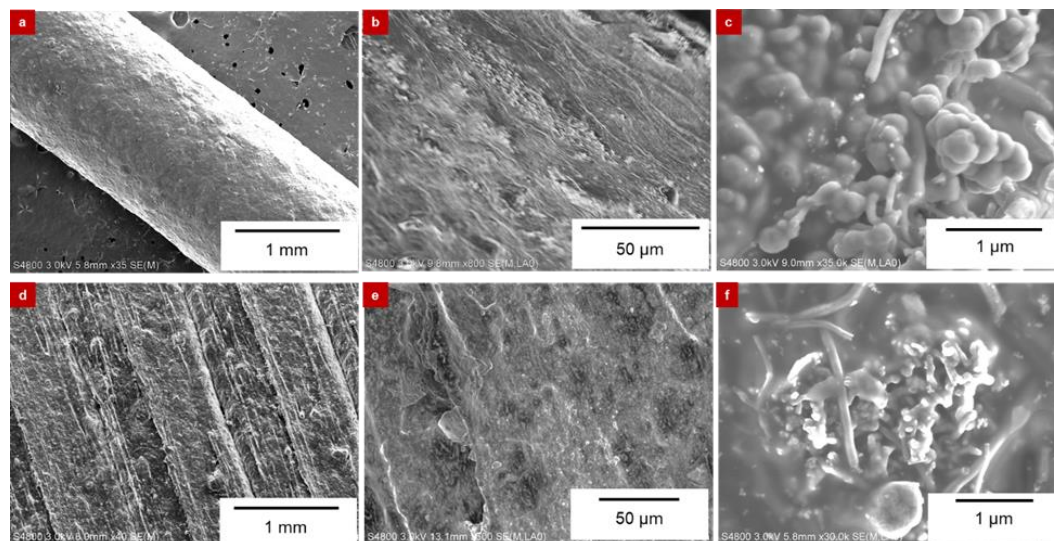


**Figure 2-2:** SEM images of the PLA-graphene before (a-c) and after MEAM (d-f).

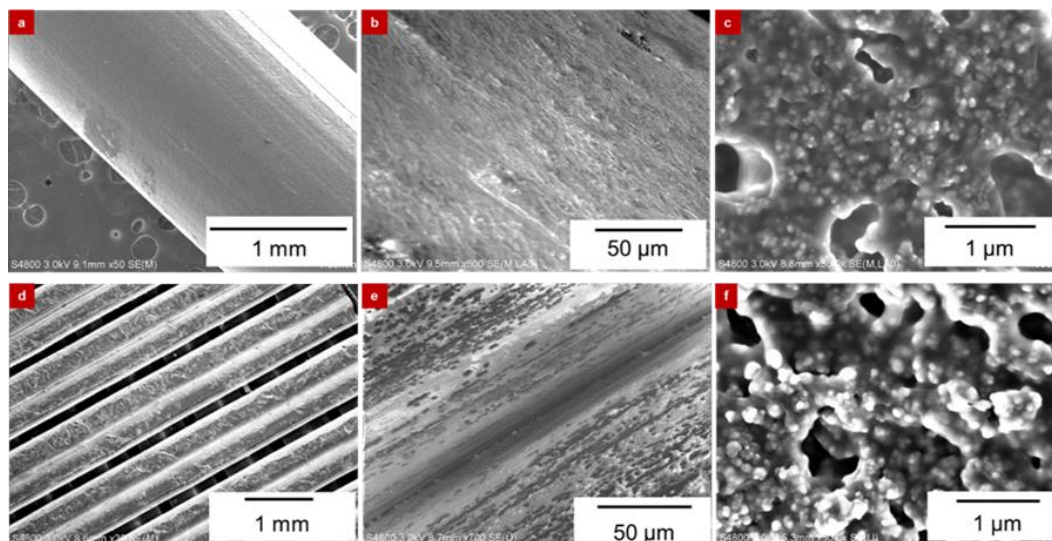


**Figure 2-3:** SEM images of the PLA-carbon black before (a-c) and after MEAM (d-f)

It can be seen from **Figure 2-3a** that the outer surface of the filament was smooth compared to the PLA-graphene filament. The surface at the 50-micron scale was smooth, and it had fewer ridges that can be seen more precisely in **Figure 2-3b**. At the 1-micron scale, the surface was porous and the filler particles between 100-300 nm were evident (**Figure 2-3c**). Print pattern on the top surface of the printed rectangular block can be seen in **Figure 2-3d**; the print pattern shows that there is spacing between the lines. The center of one of the lines was composed of a ridge is seen in **Figure 2-3e**. The printed line surface composed of voids at the micron scale and the filler particles were evident as observed in **Figure 2-3f**. The temperature-dependence of resistance for the raw PLA-graphene filament and printed PLA-graphene wire is plotted in **Figure 2-4a** and **Figure 2-4c**.

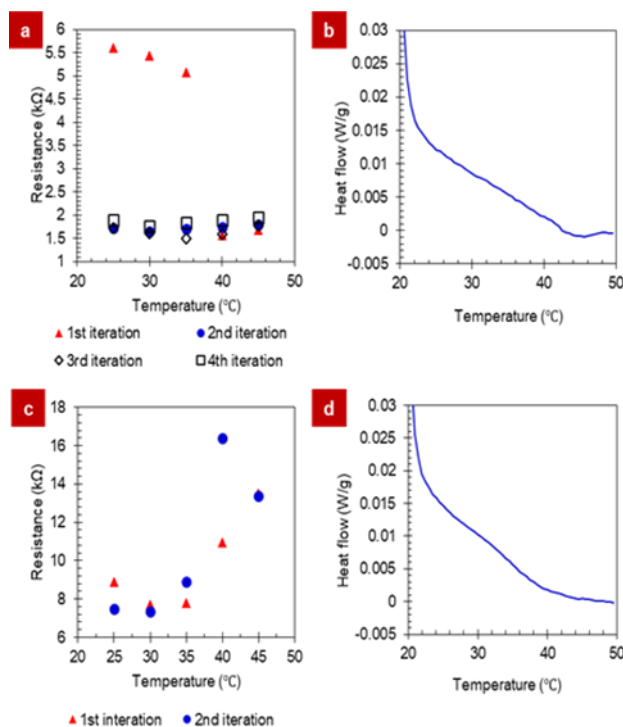


**Figure 2-4:** Characterization of PLA-graphene composite filament as-received (a, b), and after MEAM (c, d). (a) and (c) indicate the resistance of a 7.5 cm long filament and printed wire measured at temperatures from 25  $^{\circ}$ C to 45  $^{\circ}$ C with 5  $^{\circ}$ C increments. Red triangles and open diamonds indicate the results form temperature ramps from 25  $^{\circ}$ C to 45  $^{\circ}$ C. Blue circles and open squares indicate results from cool down from 45  $^{\circ}$ C to 25  $^{\circ}$ C. (b) and (d) are differential scanning calorimetry (DSC) measurements on the PLA-graphene raw filaments and printed wire, respectively.

When the raw PLA-graphene filament was first heated from 25  $^{\circ}$ C to 45  $^{\circ}$ C, the resistance dropped from 5.61  $\Omega$  to 1.59 k $\Omega$  at 40  $^{\circ}$ C. During subsequent temperature cycling, the resistance remained steady between 1.60 - 2 k $\Omega$ . The differential scanning calorimetry (DSC) of the raw filament (**Figure 2-4b**) shows a heat flow between 40 and 45  $^{\circ}$ C, which could be due to a phase change or reorganization of the graphene within the PLA matrix.

In contrast, the printed PLA-graphene wire does not show such a decrease in resistance during the first iteration. The resistance of the printed PLA-graphene wire

changes with the temperature, similar for iterations 1 and 2 (**Figure 2-4c**). The resistance value is relatively constant between 7.4 – 8.9 k $\Omega$  between 25 - 35 °C and then increases with temperature. The DSC analysis of the printed PLA-graphene wire (**Figure 2-4d**) does not indicate a sharp phase change that can explain the noticeable increase in resistance past 35 °C. Using the expression,  $\rho = \frac{RA}{l}$ , the resistivity was calculated, where  $R$  is the resistance,  $A$  is the cross-sectional area, and  $l$  is the length of the sample. The resistivity of the raw PLA-graphene filament ranged from 5.51 to 4.81  $\Omega$ -cm as temperatures varied from 25 to 45 °C, while that of the printed wire ranged from 1.29 to 0.71  $\Omega$ -cm.

The resistance of the raw PLA-carbon black filament was seen to rise linearly from 1.4 to 2.1 k $\Omega$  as the temperature was increased from 25 °C to 45 °C, and vice versa (**Figure 2-5a**). The plot of  $(R-R_{\text{ref}})/R_{\text{ref}}$  ratio against relative temperature  $(T-T_{\text{ref}})$  is linear with the slope demonstrating a positive temperature coefficient of resistance ( $\alpha$ ) of 0.0215 and 0.0204 °C<sup>-1</sup> for the ramp-up and ramp-down, respectively (**Figure 2-5b**). The graph should not be understood to mean that the TCR ( $\alpha$ ) changes as a function of temperature change. The resistance of the PLA-carbon black wire plotted against temperature is shown in **Figure 2-5d**. Like the raw filament, the resistance of the printed wire also rose linearly from 15.2 to 22.8 k $\Omega$  as the temperature changed from 25 to 45 °C. An  $\alpha$ -value of 0.0284 and 0.0242 °C<sup>-1</sup> is demonstrated for the ramp-up and ramp-down, respectively (**Figure 2-5e**). The measured  $\alpha$  is five times that of tungsten (0.0045 °C<sup>-1</sup>), which indicates the suitability of PLA-carbon black filaments for building sensitive

resistance temperature detectors on or within 3D printed parts. Further, the  $\alpha$ -value of the printed wire was found to be like that of the raw filament.

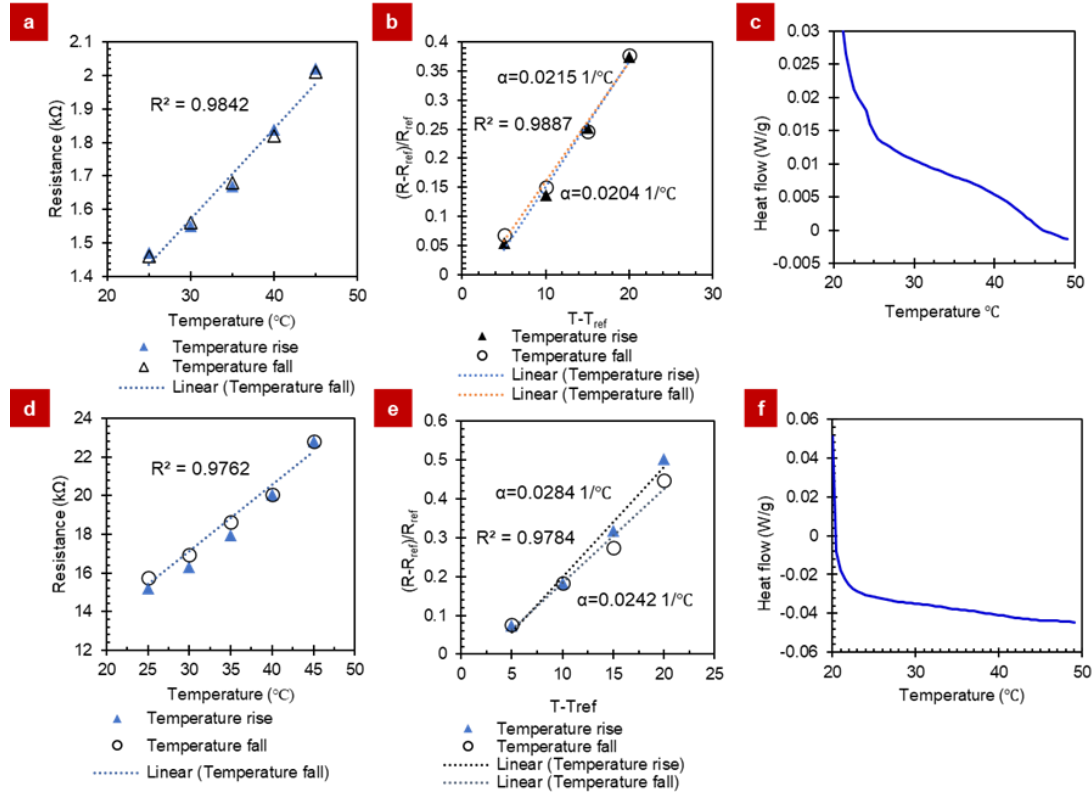


**Figure 2-5:** Characterization of the raw PLA-carbon black filament (a-c), and printed PLA-carbon black wire (d-f). (a) and (d) indicate the resistance of a 7.5 cm long filament and printed wire measured at temperatures from 25 °C to 45 °C with 5 °C increments in a cyclical manner. Blue triangles indicate results for temperature ramp from 25 °C to 45 °C. Open circles indicate the results of ramp-down from 45 °C to 25 °C. Considering the measurements at 25 °C as the reference, fractional change in resistance is plotted against the change in temperature in (b) and (e). The slope of this graph (b and e) gives the temperature coefficient of resistance. (c) and (f) are DSC measurements on the raw PLA-carbon black filament and printed PLA-carbon wire, respectively.

The resistivity of the raw filament was found to range from 5.51 to 4.81  $\Omega$ -cm as temperatures varied from 25 to 45 °C, while that of the printed wire ranged from 1.29 to 0.71  $\Omega$ -cm. It shows that the filament extrusion process does lower the resistivity of the material. The resistivity values for our printed wire are in the same range as that reported



previously in the literature. Kwok *et al.* have previously studied the temperature-dependence of resistance of polypropylene doped with 15-32% carbon black from 25 to 125 °C. The resistivity ranged from 0.65 to 26.65  $\Omega$ -cm, and the  $\alpha$ -value ranged from 0.0034 to 0.0153  $^{\circ}\text{C}^{-1}$  varying non-linearly with the carbon black composition [29].

Kiraly *et al.* studied the effects of temperature on the resistivity for various polymers (PP, PBT, and PC) with carbon black or graphite. The polymer and carbon black were mixed in the composition of polymer ranging from 96.8% to 91.8% and from 3.2% to 6.7% of carbon black. In the case of graphite filler, the composition ranged from 78.0% to 40.4% of polymer and from 22% to 49.6% of graphite. It was found that the relative resistivity increased as a function of temperature [33].

The plotting of variation of resistance with respect to temperature for a 4 mm and a 5 mm thick 3D printed PLA-graphene block subjected to a temperature cycling between 25 and 45 °C is shown in **Figure 2-6**. The resistance behavior during the first cycle was found to be different from the rest of the cycles for both blocks. When the 3D printed PLA-graphene blocks were first heated from 25 to 45 °C, the resistance dropped from 135  $\Omega$  at 25 °C to 52  $\Omega$  at 45 °C for the 4 mm thick block. This indicated a negative  $\alpha$  value of 0.0226  $^{\circ}\text{C}^{-1}$ , and from 299  $\Omega$  at 25 °C to 38  $\Omega$  at 45 °C for the 5 mm thick block, indicating a negative  $\alpha$  value of 0.0486  $^{\circ}\text{C}^{-1}$ . However, during subsequent temperature cycling, it was observed that the temperature dependent behavior of resistance was different in two ways. First, the resistance at 25 °C for 4 mm and 5 mm thick blocks was found to be higher during the first temperature sweep than that during the subsequent temperature sweeps. Secondly, we found the resistance decreased systematically until 40 °C exhibiting a negative  $\alpha$  value of 0.016  $^{\circ}\text{C}^{-1}$  for the 4 mm block and 0.017  $^{\circ}\text{C}^{-1}$  for

the 5 mm block, but the resistance was found to increase at 45 °C. This is radically different from the results for the raw filament and printed wire.

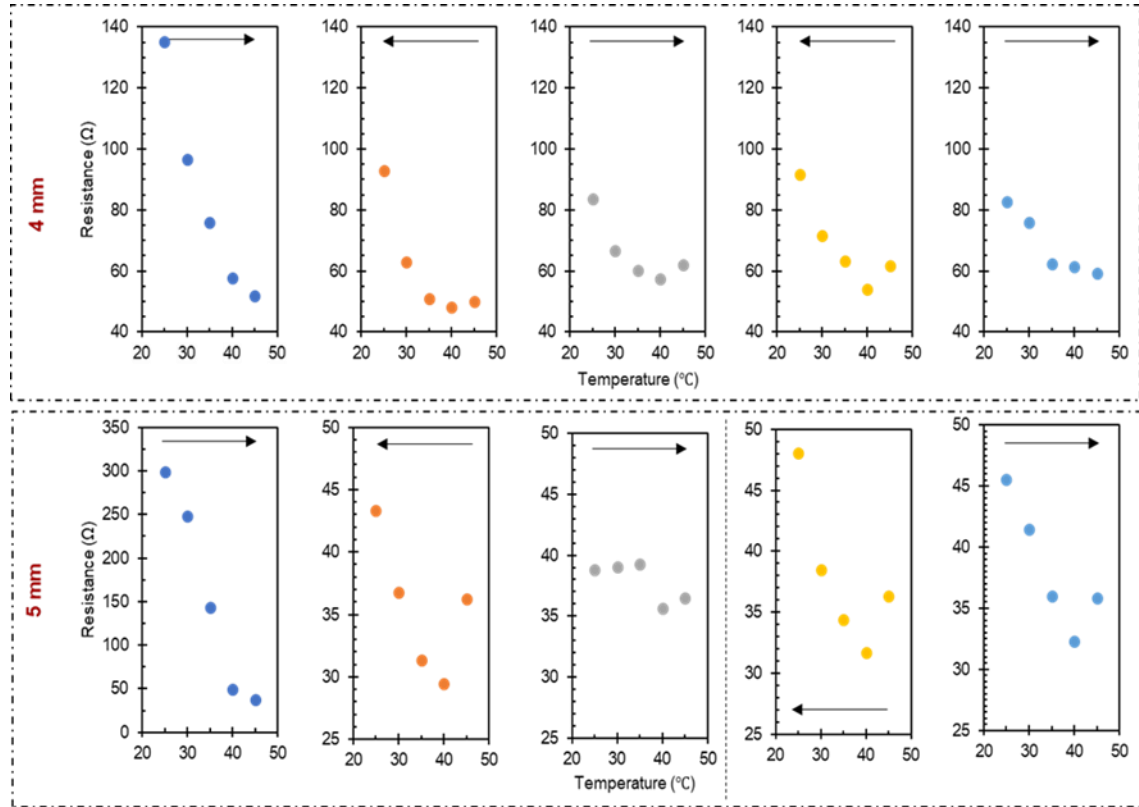


**Figure 2-6:** Temperature-dependent behavior of resistance for a 4 mm, and a 5 mm thick 3D printed solid blocks using the PLA-graphene filament. The panel of graphs represents the results from different temperature sweeps between 25 °C to 45 °C; the arrow in the graph indicates the direction of the temperature sweep. The graphs are arranged left-to-right in the sequence the temperature sweeps were carried out. The vertical dash line indicates when a one-hour break was taken between experiments.

At 25 °C, using the data for the thermocycles 2-4, the resistivity of the 4 mm thick block was found to range from 1497.73 to 1350.32  $\Omega\cdot\text{cm}$  as temperature varied from 25 to 45 °C, while that of the 5 mm thick block ranged from 559.35 to 500.39  $\Omega\cdot\text{cm}$ . In comparison, the as-received PLA-graphene filament and printed PLA-graphene wire had a lower resistivity of 5.51  $\Omega\cdot\text{cm}$  and 0.838  $\Omega\cdot\text{cm}$ , respectively. Another block that was 3 mm thick was printed, the resistivity was found to range from 795.69 to 548.60  $\Omega\cdot\text{cm}$

from 25 to 45 °C. No correlation between the numbers of 3D print layers in the block to the resistivity was found; however, a more controlled experiment on a wire-like feature would be more suitable for elucidating the effect of interlayer adhesion.

Further, the effect of an hour-long break on the resistance of the 5 mm thick PLA-graphene block was studied. During this break, the oven in which the samples were placed was turned off and the whole set-up was cooled down to room temperature. This was done to see if the initially seen higher resistance of 299  $\Omega$  at 25 °C is recoverable. After the break, the resistance measured close to 50  $\Omega$  at 25 °C, which is slightly higher compared to 39-45  $\Omega$  measured for the second, third and fifth cycle. It was found that such hour-long breaks had no effect on the results for the raw filament and printed wire.

The variation of resistance with respect to temperature for a 4 mm and a 5 mm thick 3D printed PLA-carbon black block subjected to a temperature cycling between 25 °C and 45 °C is shown in **Figure 2-7**. Like the 3D printed PLA-graphene blocks, the PLA-carbon black blocks exhibited a decrease in resistance over the first temperature sweep and showed a different trend for subsequent thermocycles. For the 5 mm thick block, the resistance decreased from 24.64 to 20.08  $\Omega$  and for the 4 mm block, it dropped from 17.81 to 15.80  $\Omega$  with a negative  $\alpha$  of 0.0073 °C<sup>-1</sup> and 0.0052 °C<sup>-1</sup>, respectively. During the subsequent temperature cycles, two things were noticed.

First, the resistance is higher at 25 °C for the first sweep. However, the resistance decreased for subsequent temperature cycles. Secondly, the resistance was found to either remain constant or decrease between 25 to 35 °C, and then increase as temperature was ramped to 45 °C with a positive  $\alpha$  of ~0.009 °C<sup>-1</sup> for the 5 mm block and ~0.009 °C<sup>-1</sup> for

4 mm. This is not in agreement with the results for the raw PLA-carbon filament and the printed PLA-carbon wire where a positive  $\alpha$  value was obtained.

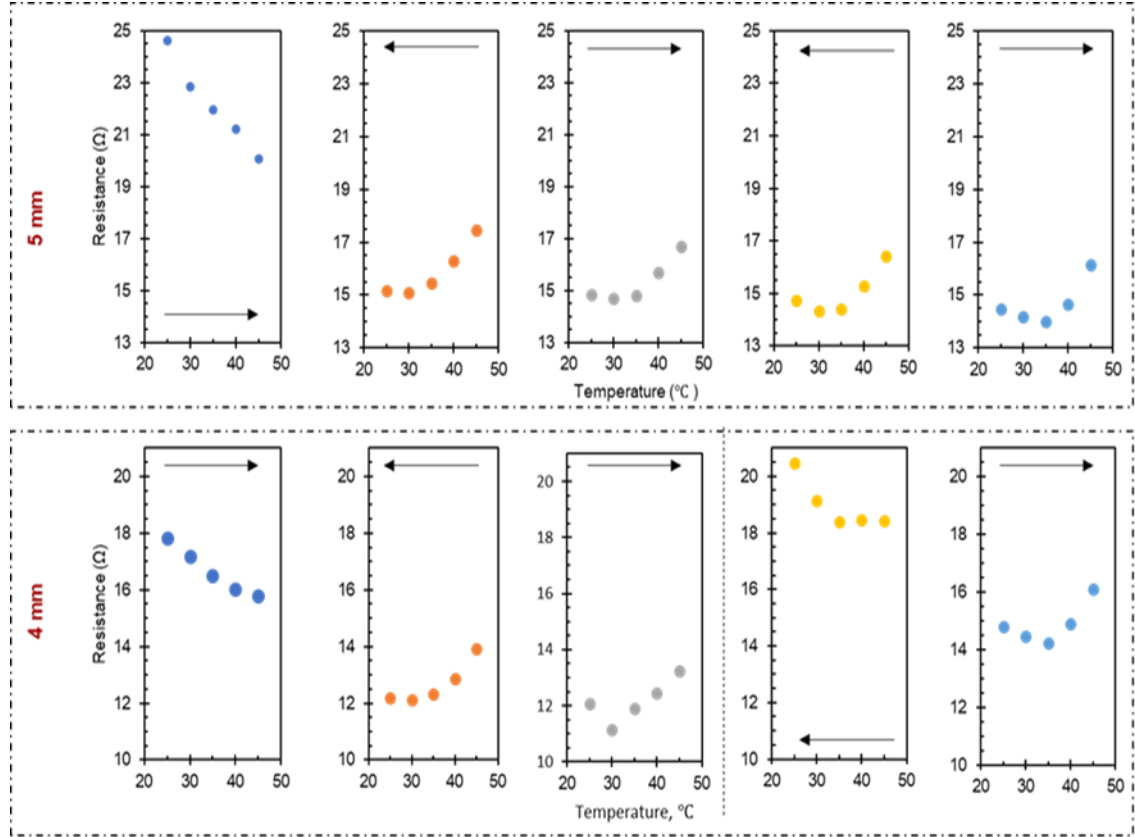


**Figure 2-7:** Temperature-dependent behavior of resistance for a 4 mm, and a 5 mm thick 3D printed solid blocks using the PLA-carbon black filament. The panel of graphs represents results from different temperature sweeps between 25 °C to 45 °C; the arrow in the graph indicates the direction of temperature sweep. The graphs are arranged left-to-right in the sequence the temperature sweeps were carried out. The vertical dash line indicates when an hour-break was taken between experiments.

The decrease in resistance of 3D printed blocks after first thermocycling could be explained either by, (1) the increase in interlayer adhesion, which further improves the electrical contact between the several print layers during the first temperature cycling, or (2) the desorption of moisture during the first temperature cycling. Because the 3D printing was carried out with a bed temperature of 110 °C, we believe that the

temperature ramp to 45 °C will not improve the interlayer adhesion further. The desorption of moisture from the 3D printed blocks is most likely the cause for the observed drop in resistance at 25 °C due to temperature cycling.

Typically, in conductive polymer composites, a positive  $\alpha$  value has been observed. The anomalous negative  $\alpha$  value of the 3D printed PLA-graphene blocks is difficult to explain. One explanation could be the thermal expansion forces the elastic reduction of void volume incorporated within the 3D printed block and the resulting increase in volume to surface area leads to lowered resistance. In the case of PLA-graphene, the few-layer thick graphene phase is expected to have a lower thermal expansion in comparison to the carbon black phase in PLA-carbon black. This could be the reason an increase in resistance for the 3D printed PLA-carbon black at 30 or 35 °C is seen, while such an increase is only seen at 40 °C for PLA-graphene.

The effect of a break on the restoration of resistance for the 4 mm thick PLA-carbon black block was more apparent. During the first temperature sweep, the resistance first measured was  $\sim 18 \Omega$  at 25 °C. After the break, the first measurement of resistance was  $\sim 20.5 \Omega$  at 25 °C. This is less than a 13% change from the original resistance value. However, since TCR characteristics of the printed block are retained, they can be used for temperature sensitive application. The break was not long enough for moisture to increase the resistance; also, such moisture absorption effects would have been noticeable during the testing of the raw filament and printed wire. The decrease in interlayer

adhesion seems to be a more probable cause for the restoration of the resistance in case of PLA-carbon black blocks.

## 2.4 Conclusion

In summary, the microstructure and temperature dependence of resistance was characterized for electrically conductive PLA-carbon black and PLA-graphene composites, in the form of a filament before MEAM and in the form of a wire and a rectangular block made via MEAM. Microstructural investigations using SEM and Raman did not indicate microstructural changes between the filament and the printed parts. Electrical resistivity of the filament and printed wire measured using impedance spectroscopy exhibited 4-6 times decrease due to MEAM: for PLA-graphene, from 5.5-4.8  $\Omega$ -cm before extrusion to 1.3-0.7  $\Omega$ -cm after extrusion, for PLA-carbon black, from 6.4-4.6  $\Omega$ -cm before extrusion to 2.2-1.4  $\Omega$ -cm after extrusion. However, the resistivity of the printed rectangular block, which is composed of multiple layers, was significantly higher than that of the extruded wire; 1497.7-1350.3  $\Omega$ -cm and 539.4-500.4  $\Omega$ -cm for a PLA-graphene printed block of thickness 4 mm and 5 mm, respectively, and 330.2-179.9  $\Omega$ -cm and 225.2-180.5  $\Omega$ -cm for a PLA-graphite printed block of thickness 4 mm and 5 mm, respectively. The as-received PLA-carbon black filament and the printed wire showed a positive temperature coefficient of resistance ( $\alpha$ ) between  $\sim 0.03$ - $0.01$   $^{\circ}\text{C}^{-1}$ , which makes it more suitable for sensor development. The as-received and the extruded PLA-graphene wire did not exhibit a significant  $\alpha$ , which makes it more suitable for printing wires.

In contrast, the MEAM parts obtained with these filaments exhibited a negative or a negligible  $\alpha$  up to a certain temperature prior to exhibiting a positive  $\alpha$ ; furthermore,

these  $\alpha$  values were significantly lower than those obtained for the filaments before or after extrusion. These findings will enable an informed design and modeling of MEAM electronics and sensors, including making a choice between conductive filaments and the design of single-layer versus multi-layer element.

## **CHAPTER 3**

### **INFLUENCE OF INTERFACE ON THE ELECTRICAL PERFORMANCE OF MEAM STRUCTURES**

#### **3.1 Introduction**

Additive Manufacturing technology has advanced to being a major player in the field of manufacturing in the last two decades. It has been used for multiple applications including manufacturing mechanical parts for aerospace and automotive applications [34], prosthetics [35], and dentistry [36]. The application of additive manufacturing in the production of passive and active electronic components is fascinating. An in-depth review of 3D printed electronic sensors reported so far has been provided by Yuanyuan *et al.* [37]. Material extrusion-based additive manufacturing (MEAM) is an additive manufacturing technique that is uniquely suited for cost-effective printing electronic components with multiple materials. Recent developments in the MEAM materials have allowed for realizing various kinds of sensors including pressure sensor [38], temperature sensor [30], tactile sensor [39], displacement sensor [40], accelerometer [41], angular sensor [42], acoustic sensor [43], electromagnetic sensor [44], chemosensor [45], food quality sensor [46], flow sensor [47], and EEG sensor [48], antennas [49], and appliances such as a coffee warmer [5].



MEAM builds 3D structures in a layer-by-layer manner, by extruding a thermoplastic material through a nozzle heated above the melting point of the plastic. The extruded fiber in each layer is laid out in a specific manner as instructed by the g-code (**Figure 3-1**). The extrusion process relies on the push exerted by the stepper motor and toothed gears, as well as on the adhesion between the extruded fiber and the bed; the latter often heated for improved fiber-bed adhesion. Several parameters including extrusion (nozzle) temperature, print speed, bed temperature, part orientation, layer height, raster angle, and infill can be varied in MEAM. These have shown to be correlated directly to the resulting part dimension, residual stress, and mechanical part performance [50-58].

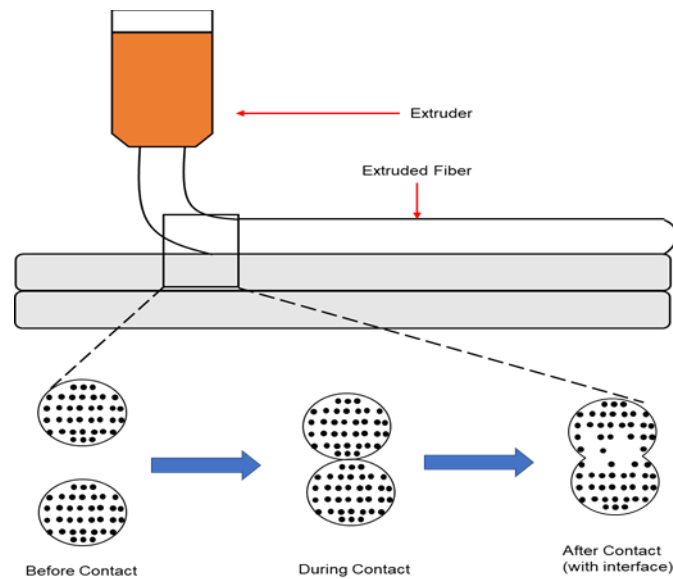


**Figure 3-1:** The representation of the interface as the intersection of the subsequent layer deposition during the MEAM process.

In the current literature, there is preponderance of research on the effects of MEAM print parameters on mechanical performance of the 3D printed structure. These are either experimental investigations varying the print parameters systematically to

examine their effects on printed part performance [59-64], or simulation efforts examining the effect of the print parameters on the resulting meso-structure material properties. For instance, simulation of thermal history can be obtained by modeling the extruded fiber with a temperature gradient using the William-Landel-Ferry equation [65]. Further, the inclusion of viscous forces of the molten plastic allows reconstructing the mesostructure and measuring the mechanical strength [66-72]. Understanding how the print parameters affect the thermal history and the resulting part's shape has allowed researchers to model the MEAM process and predict the mechanical part performance.

Contemporary simulation models and experimental studies show the importance of interlayer bonding in creating anisotropy in mechanical strength of the printed parts. Coogan *et al.* printed hollow box structures to determine a correlation between interlayer bond strength and print parameters including wall position, bed temperature, extrusion temperature, print speed, fiber width, and layer height [73]. It was found that the fiber width, layer height, and extrusion temperature play a significant part in bond strength compared to the speed or the wall position. Recently, Allum *et al.* used a similar hollow box geometry and showed that the anisotropic strength of the printed structures can be explained by cross-sectional geometry and the resulting load-bearing effectiveness for a range of fiber widths and layer heights [74].

To develop MEAM into an industrially feasible technique for 3D printing electronic components, similar fundamental studies are necessary to predict electrical part performance based on the known print parameters. The existing two studies with conductive MEAM materials also point to the impact of bond interfaces (shown in **Figure 3-1**) on electrical resistance; however, the extent of scientific investigation is

limited. Using a custom synthesized electrically conductive material composed of 15 wt% carbon black in acrylonitrile butadiene styrene, Zhang *et al.* point out the existence of anisotropy in resistivity of MEAM samples, and show that resistivity across layers can be tuned by three factors, namely, layer height, voids, and raster angle [75]. Our prior work using a commercial composite of carbon black in polylactic acid shows that an extruded fiber has lower resistivity compared to the raw material; however, the resulting MEAM cube exhibits a drastically increased resistivity [76]. For better characterization of the conductive MEAM structures, a more fundamental study needs to be conducted, in which the complications of layer height, infill, and raster angles are avoided.

In the study laid out in this chapter, a prior reported hollow box structure was used to examine the effect of extrusion temperature and print speed on the electrical characteristics of the bond interfaces, specifically those between two subsequent layers. The walls of the hollow box compose of single extruded fibers stacked on top of each other. The electrical characteristics are measured using small signal impedance spectroscopy to avoid Joule heating effects. The impact of varying the extrusion temperature and print speed on electrical impedance was examined in two directions, across the interlayer bond interfaces (Z-specimen or Z-direction), and along the interlayer bond interfaces (F-specimen or F-direction). The results quantify anisotropy in electrical property as the extrusion temperature and print speed were varied. Further, electrical characterization of single and multiple bond interfaces was performed to understand the scaling law of electrical resistance across bond interfaces. By investigating the bond interfaces and the role they play in determining the electrical behavior, a framework to model and predict electrical behavior based on print parameters is sought.

## 3.2 Methodology

### 3.2.1 Sample Preparation

A customized g-code for a hollow box was written using FullControl GCode Designer as shown in **Figure 3-2a** [77-79]. Each wall was one extruded fiber wide. Such boxes were printed with printing speeds of 750, 1000, 1500, or 2000 mm/min, and extrusion temperatures of 190, 210, or 230 °C. Printing was performed using Protopasta conductive polylactic acid (c-PLA) of width 1.75 mm on a MakerGear M3 ID with a 0.35 mm nozzle, layer height of 0.2 mm, bed set to 70°C, bed lines with Kapton tape, and part cooling fan set at 65% of its max capacity.

For testing, a face of the cube was isolated and trimmed with shears to a 39 mm x 39 mm square, which was then cut into 13 mm x 13 mm samples using a 3D printed jig shown in **Figure 3-3**. A 6.35-, 5.56-, or 4.78-mm wide copper tape with acrylic adhesive was used to mask varying number of interfaces during sputter coating the samples with 50 nm gold thin film. To probe single bond interfaces, a jig as shown **Figure 3-3** was used to mask three isolated bond interfaces when sputter coating 39 mm x 39 mm face and then trimming 13 mm x 13 mm samples from it.

### 3.2.1 Electrical Impedance Spectroscopy

An Ivium CompactStat was used to perform impedance spectroscopy with a 5-mV sinusoidal signal with frequency ranging from 100 Hz to 600 kHz. We found that the stress on the sample due to the alligator clips affected the readings. The stress was reduced by laying the samples flat on a 1 mm thick microscope glass slide.

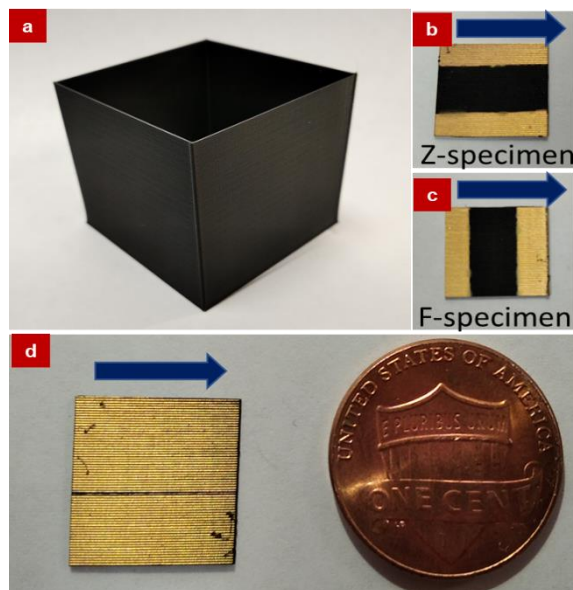


**Figure 3-2:** (a) Example of hollow box, a four-wall structure, printed for this research with a layer thickness of 0.2 mm. Samples, 13 mm x 13 mm, were trimmed from the walls prior to sputtering Au. (b) Z-specimen with approximately 30 bond interfaces between the two gold coated areas. The blue arrow points the direction of the fibers. (c) F-specimen. The gold electrodes patterned perpendicularly in comparison to Z-specimen. (d) Sample for probing single bond interface.

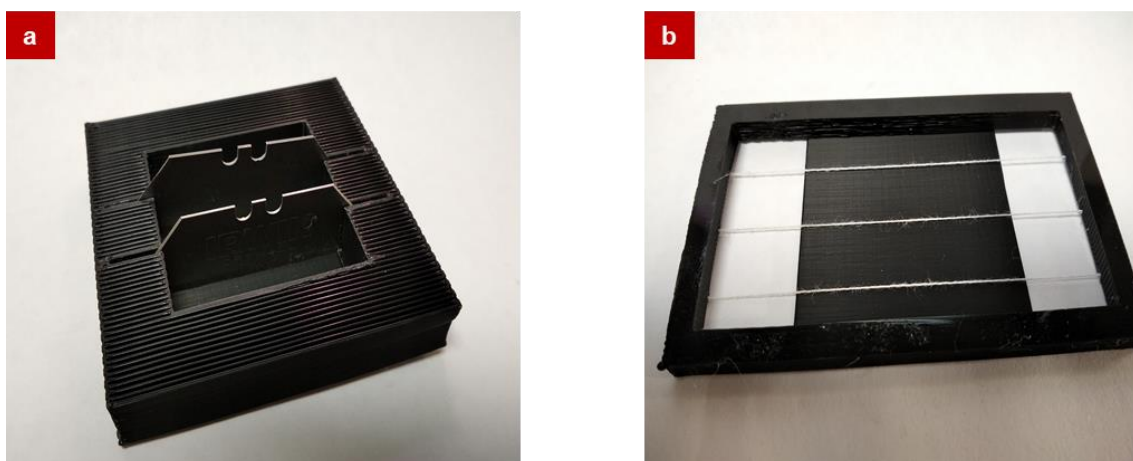


**Figure 3-3:** (a) Equally spaced jig with razor blades to cut the wall, 39 mm x 39 mm, into smaller samples, 13 mm x 13 mm. (b) Jig with twines to mask a single bond interface during sputtering coating of the sample with a 50 nm gold layer.

### 3.2.2 Microscope Imaging

The cross-section images of the samples were measured using a Leica compound microscope and a special sample holder for cross-section analysis.

### 3.2.3 Modeling and Simulation

The microscopy images of the sample cross-section were imported into Inkscape to outline the sample's cross-section. The outline was saved in '.dxf' format, imported into Autodesk Fusion 360 and extruded to reflect the sample dimensions accurately. Thus, the generated 3D object was saved to a '.stl' file and imported into COMSOL Multiphysics 5.4. The 3D object was modeled with the properties of cPLA, whose material properties were specified based on our prior work [76]. For cPLA, the density, heat capacity, and thermal conductivity were set to  $1210 \text{ kg m}^{-3}$ ,  $1536 \text{ J kg}^{-1} \text{ K}^{-1}$ , and  $0.366 \text{ W m}^{-1} \text{ K}^{-1}$ , respectively [80]. Relative permittivity, reference resistivity, and temperature coefficient of resistivity for the cPLA were set to 9 [81],  $0.018 \text{ } \Omega \cdot \text{m}$  at  $298.15 \text{ K}$  [76], and  $0.02 \text{ K}^{-1}$  [76], respectively. The resistivity of the cPLA was modeled linearly as a function of temperature. The convective heat loss from the overall geometry to the surrounding air ( $298.15 \text{ K}$ ) was modeled using an approximate heat transfer coefficient of  $10 \text{ W m}^{-2} \text{ K}^{-1}$ . A small voltage of  $5 \text{ mV}$  was used to determine the resistance in the F- or Z-direction.

## 3.3 Results and Discussion

In the following sections, the results from testing the impedance for different printing settings in the F- and Z-directions, then test the scalability of the impedance over multiple interfaces, and lastly characterize the morphology and elemental analysis of the interface region are discussed.

### 3.3.1 Impact of Printer Settings on Impedance

The magnitude of the impedance was measured across approximately 30 bond interfaces printed with varying extrusion temperatures and print speeds. The obtained mean and the respective standard deviation are shown in Error! Reference source not found.. First, the effect of the print settings on the impedance was examined, and then we compared the impedance between the F- and Z-specimen. In the Z- and F-specimen alike, the impedance was found to have an inverse relationship with the extrusion temperature, that is, the samples printed at higher temperature exhibited lower impedance as shown in Error! Reference source not found. **a**; p-value is the measurement of the likelihood of the observed results given a null hypothesis if it is true. In this case, the p-values would show the influence of the extrusion temperature and print speed on the electrical resistance. The p-values calculated using an unpaired unequal variance t-test is shown in **Table 3-1** and **Table 3-2** for the F- and Z-specimen. No clear trend was seen in the impedance's magnitude with variations of print speed in the case of Z- or F-specimen. The p-values in **Table 3-3** and **Table 3-4** do identify scenarios where statistically a significant difference was seen with variations in print speed, but the overall trend was not found to be consistently ascending or descending.

We performed multiple linear regression to correlate impedance magnitude and printing variables using an expression as reported earlier [73]. Below, the correlations were determined by **Eq. 3-1** and **Eq. 3-2**.

**Table 3-1:** The p-values comparing the impedance when measured in the F-direction from the samples printed with varying extrusion temperatures. The p-values were calculated using an unpaired unequal variance t-test and represent probability for the hypothesis that the impedance due to varying extrusion temperatures are different. A p-value > 0.05 indicates the hypothesis is nullified.

	Low	Medium Temperature	High Temperature
750 mm/min	$9.75 \times 10^{-30}$		
	$1.82 \times 10^{-37}$		
		$9.75 \times 10^{-30}$	
1000 mm/min	$2.03 \times 10^{-14}$		
	$1.95 \times 10^{-15}$		
		$4.38 \times 10^{-6}$	
1500 mm/min	$5.82 \times 10^{-11}$		
	$9.15 \times 10^{-26}$		
		$1.77 \times 10^{-27}$	
2000 mm/min	$2.33 \times 10^{-31}$		
	$7.02 \times 10^{-41}$		
		0.0003	

**Table 3-2:** The p-values comparing the impedance when measured in the Z-direction from samples printed with varying extrusion temperatures. The p-values were calculated using an unpaired unequal variance t-test and represent probability for the hypothesis that the impedance due to varying extrusion temperatures are different. A p-value > 0.05 indicates the hypothesis is nullified.

	Low	Medium Temperature	High Temperature
750 mm/min	$1.07 \times 10^{-27}$		
	$1.49 \times 10^{-51}$		
		$1.06 \times 10^{-27}$	
1000 mm/min	$2.33 \times 10^{-7}$		
	$1.32 \times 10^{-16}$		
		0.003	
1500 mm/min	$4.67 \times 10^{-37}$		
	$5.38 \times 10^{-47}$		
		$5.75 \times 10^{-27}$	
2000 mm/min	$3.48 \times 10^{-42}$		
	$1.03 \times 10^{-44}$		
		$3.65 \times 10^{-8}$	



**Table 3-3:** The p-values comparing the impedance when measured in the F-direction from the samples printed with varying speeds. The p-values were calculated using an unpaired unequal variance t-test and represent probability for the hypothesis that the impedance due to varying print speeds are different. A p-value > 0.05 indicates the hypothesis is nullified.

	750 mm/min	1000 mm/min	1500 mm/min	2000 mm/min
High Temperature	0.17			
	0.01			
	0.51			
		0.27		
		0.45		
			0.05	
Medium Temperature	$2.16 \times 10^{-13}$			
	$2.17 \times 10^{-11}$			
	$4.17 \times 10^{-6}$			
		$2.33 \times 10^{-33}$		
		0.43		
			$5.80 \times 10^{-16}$	
Low Temperature	$8.58 \times 10^{-6}$			
	$8.58 \times 10^{-6}$			
	0.03			
		1		
		$2.06 \times 10^{-6}$		
			$2.06 \times 10^{-6}$	

**Table 3-4:** The p-values comparing the impedance when measured in the Z-direction from the samples printed with varying speed. The p-values were calculated using an unpaired unequal variance t-test and represent probability for the hypothesis that the impedance due to varying print speeds are different. A p-value > 0.05 indicates the hypothesis is nullified.

	750 mm/min	1000 mm/min	1500 mm/min	2000 mm/min
High Temperature	0.51			
	$9.71 \times 10^{-9}$			
	0.002			
		0.003		
		0.099		
			0.001	
Medium Temperature	0.27			
	$3.34 \times 10^{-8}$			
	$9.75 \times 10^{-7}$			
		0.0002		
		0.27		
			$1.32 \times 10^{-26}$	
Low Temperature	$3.73 \times 10^{-5}$			
	$1.40 \times 10^{-14}$			
	0.12			
		$1.63 \times 10^{-11}$		
		$5.17 \times 10^{-6}$		
			$1.29 \times 10^{-10}$	

For Z-specimen,  $R^2 = 0.76$

$$\text{Impedance} = -5.01T + 0.01S + 1353.11 \quad \text{Eq. 3-1}$$

For F-specimen,  $R^2 = 0.59$

$$\text{Impedance} = -2.04 - 0.004S + 578.22 \quad \text{Eq. 3-2}$$

where,  $T$  is the extrusion temperature in °C, and  $S$  is the print speed in mm/min.

Correlations for both F- and Z-specimen show that the extrusion temperature plays an important role as opposed to the print speed. This can be evidenced by the higher value of the coefficient as well as the p-values in the fit details. The  $R^2$ -value may seem low for the correlation (2) to be significant; however, closer inspection of the fit details shown in the four tables above shows that the low  $R^2$  arises due to a noticeable percentage error in the coefficient for print speed when compared to the coefficient for the extrusion temperature and the constant. A similar observation also holds true when examining the fit details for correlation (1). This indicates that the impact of the print speed was minimal within the range tested.

An important observation was the variation of the impedance with the extrusion temperature, specifically within the F-specimen. This could be attributed to either the sample's cross-section, or the electrical conductivity of the material changing with the extrusion temperature. To characterize the differences in the cross-sectional area in F-direction, optical microscope images of the cross-section were acquired and analyzed via the thresholding method [74]. **Figure 3-4:** (a) Sample cross-section images of the 3D printed samples in the F-direction via optical microscopy. (b) Example of the processed cross-section obtained via thresholding in ImageJ. shows the example cross-section

images obtained due to thresholding. Quantification of the sample cross-section area ( $A$ ) with respect to sample length ( $L$ ) showed that the  $A/L$  ratio obtained with different extrusion temperatures were found to be within one standard deviation (ref. **Figure 3-5**). If the electrical conductivity ( $\sigma$ ) remained constant regardless of the extrusion temperature, the resistance ( $R = \frac{\rho L}{A}$ ), and thus the impedance of F-specimen linearly decreased with  $A/L$  ratio.

However, that is not the case. Low extrusion temperature leads to a higher impedance compared to medium and high extrusion temperatures as shown in Error! Reference source not found.. This implies that the electrical conductivity of the carbon black doped polylactic acid changes as a function of extrusion temperature. These results agree with the trend reported by Watschke *et al.*, that the resistivity of the extruded conductive PLA was found to decrease with the extrusion temperature [82].

While the trends for variations of the impedance in relation to print speed and extrusion temperature were similar for F- and Z-specimens, the impedance for Z-specimen were found to be greater than that for F-specimen as shown in Error! Reference source not found., thus indicating anisotropic electrical resistance or impedance in MEAM prints. To understand if the anisotropy in electrical resistance or the impedance changes with extrusion temperature or print speed, the ratio of the impedances in Z- over F-direction, here onwards referred to as the Z/F ratio, is plotted in **Figure 3-6**. The Z/F ratio allows us to

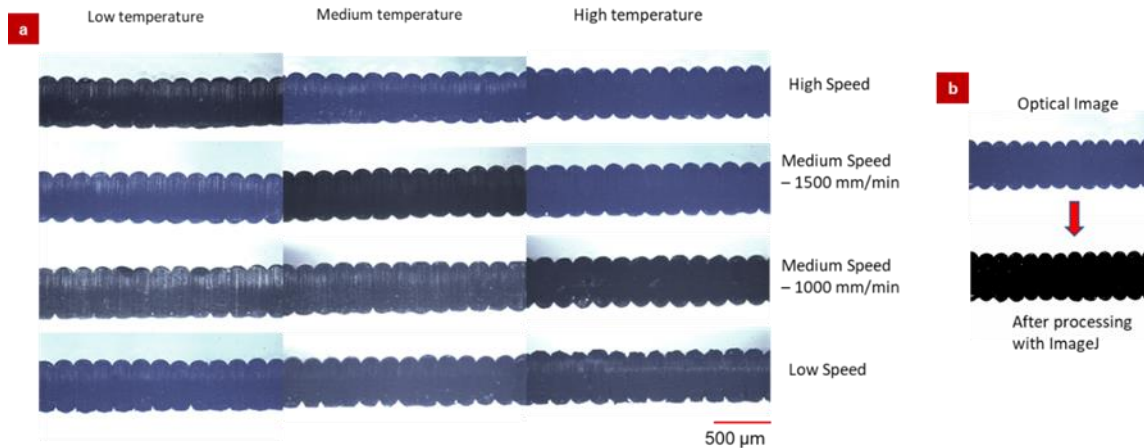


**Figure 3-4:** (a) Sample cross-section images of the 3D printed samples in the F-direction via optical microscopy. (b) Example of the processed cross-section obtained via thresholding in ImageJ.

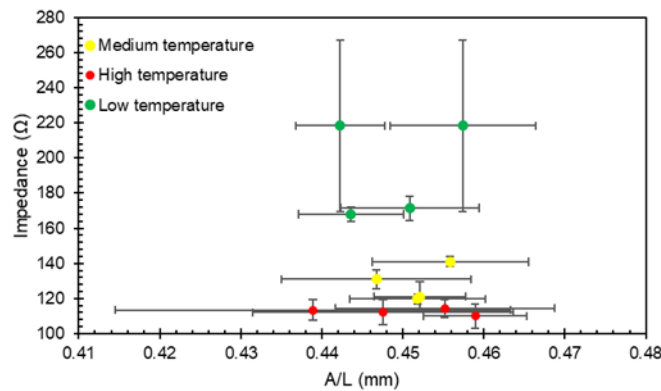


**Figure 3-5:** Plot of impedance obtained with F-specimen against A/L for the samples. The red circle indicates data points corresponding to low extrusion temperature. The blue circle indicates data points corresponding to medium extrusion temperature. Data represented from 3 samples for each of the 12 printing conditions, and 3 images from each sample were analyzed using ImageJ. Error bars represent standard deviation.

understand if the electrical impedance of the bond interfaces depends on the extrusion temperature or print speed, while allowing mitigating the effect of the variations in resistivity due to the extrusion temperature as found above. Aside from normal experimental variation, the Z/F ratio was found to be constant, as shown in **Figure 3-6**, with a mean value of 2.15 and a standard deviation of 0.23.

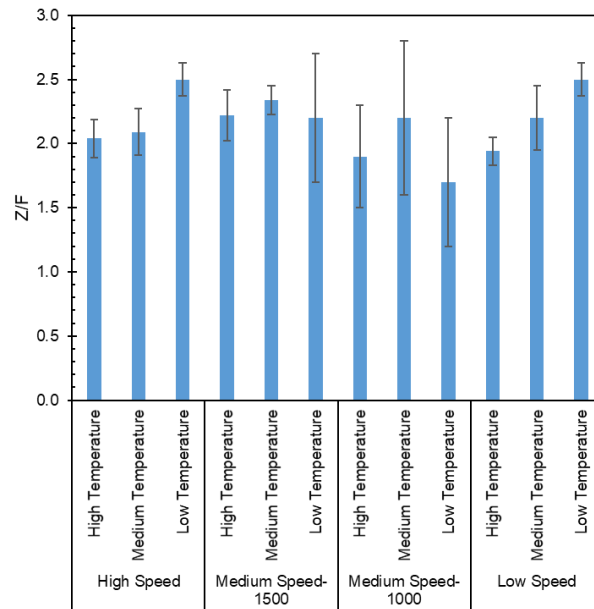


**Figure 3-6:** The ratio of impedance measured between Z-specimen and F-specimen plot against print parameters. Individual impedance data is shown in **Figure 3-2**. The error bars were calculated in Python using ‘uncertainties’ package. Specimen printed at 750 mm/min (low), 1000 mm/min (med), 1500 mm/min (med), or 2000 mm/min (high), and with a nozzle temperature of 190 °C (high), 210 °C (med), or 230 °C (high).

### 3.3.2 Comparing Impedance in F- and Z- Direction

Next, we investigated the cause of the higher impedance in the Z-direction. Could it be attributed to the cross-sectional area being different in the Z- and F-directions? On the other hand, could it be attributed to the presence of bond interfaces in the Z-direction? In the Z-direction, the cross-sectional area of the specimen changes due to the geometric narrowing at the interface between the two layers. Thus, the cross-sectional area ( $A$ ) for electrical charge transport would change with the travelled length in the Z-direction, and thus increase the resistance ( $R = \frac{\rho L}{A}$ ).

In contrast, the cross-sectional area would be constant for charge transport in the F-direction. To find out if the differences in the cross-sectional area were responsible for

the observed anisotropy in the electrical impedance, 3D model of the samples were reconstructed in a finite element package COMSOL Multiphysics using optical images of the sample cross-section. In this manner, the impact of print speed and extrusion temperature on the sample cross-section was accounted, and current constriction at the interface due to geometric narrowing was examined. The COMSOL simulations showed that the voltage drop across the cross-section was uniform as shown in **Figure 3-7(a-d)** and the impedance of the sample in the Z- and the F-directions calculated to be similar. This suggests that the geometric narrowing at the interfaces was not responsible for the observed anisotropy in electrical impedance (Z/F).

Through the combination of specimen design, controlled manufacturing, and careful characterization, it is shown here that the anisotropy in electrical impedance in MEAM prints is constant regardless of the extrusion temperature and the print speed. The process of MEAM causes repeated heating and cooling of the structure with the addition of subsequent layers. Using a layer length of ( $L = 4 \times 45 \text{ mm}$ ) 180 mm, a reasonable underestimation of convection coefficient ( $h$ ) of  $10 \text{ W m}^{-2} \text{ K}^{-1}$  when part cooling fan is employed, and a thermal conductivity ( $k$ ) of  $0.366 \text{ W m}^{-1} \text{ K}^{-1}$  for conductive PLA, the Biota number,  $Bi = \frac{hL}{k}$  is estimated to be 4.92. For a poor thermal conductor like conductive PLA, this suggests that the interior resistance to heat flow will exceed that of the air-PLA boundary. The extrusion temperature varied from 190 °C to 230 °C, which is 17 °C to 47 °C above the melting point of c-PLA, 173 °C. This shows the extremes of heating and cooling that has been attempted in our experiments. Furthermore, the print speed has been increased from 750 mm/min to 2000 mm/min; this decreases the layer time by 266%, from 14.4 s to 5.4 s, which means a lot faster cyclic heating and cooling,

and a relatively larger difference in layer temperature on which freshly extruded fiber was laid down.

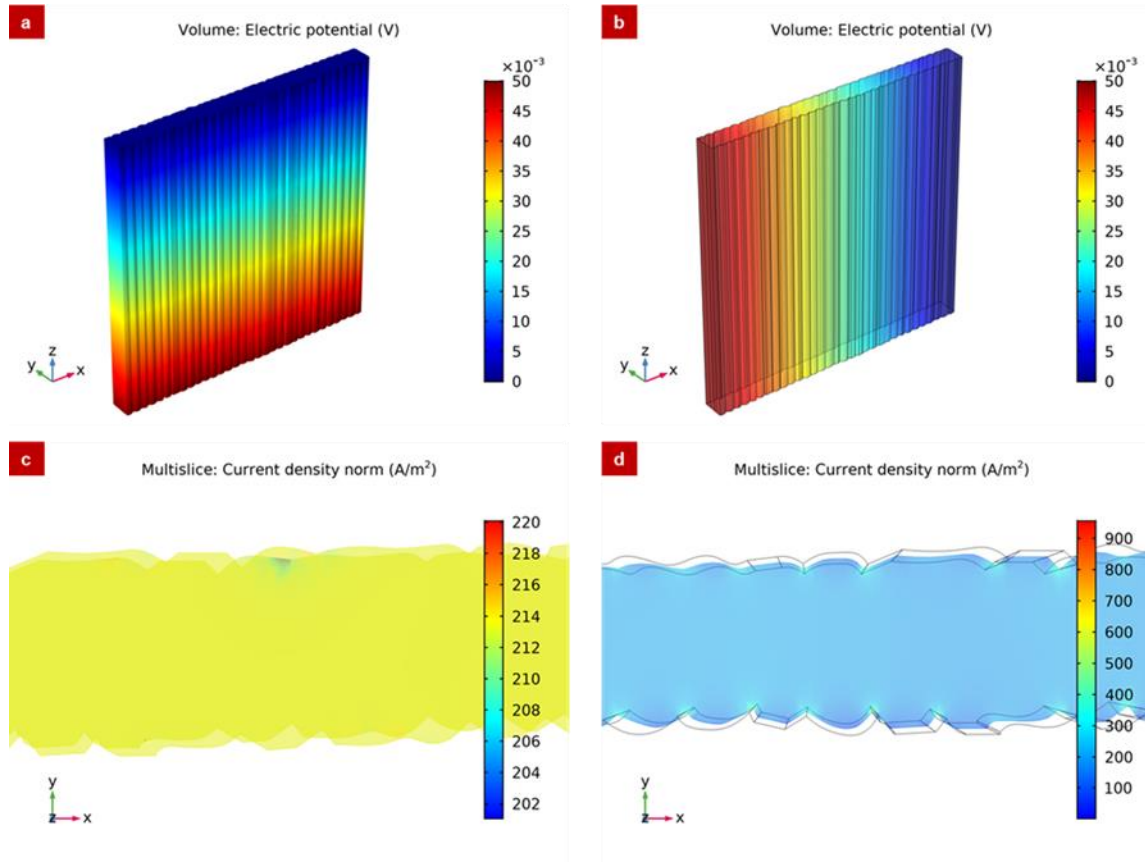


**Figure 3-7:** Finite element analysis of the sample geometry recreated using microscopy images of the sample cross-section. (a) and (b) show electric potential distribution when the sample was biased along the F- and Z- directions, respectively, and (c) and (d) show respective normalized current density at the sample cross-section containing bond interfaces. The structure results in a resistance of ~50 Ohms in both F- and Z- directions.

Similarly, the formation of the bond and alignment of polymer chains would be hugely different at different speeds and different extrusion temperatures, but apparently, this has no effect on the anisotropy ratio Z/F. This was only feasible through the excellence in the design of the specimen, choice of material and control over manufacturing and detailed characterization. While previously, Zhang *et al.* have used a



cube sample geometry to demonstrate the effect of the layer's height, layer's width and air gap on anisotropy, to the best of our knowledge, the present study is the first work reporting the effect of the layer's time and extrusion temperature on anisotropy in electrical impedance. Also, the Z/F values obtained in our work were in the similar range as calculated from results reported by Zhang *et al.* using an extrusion temperature of 230 °C at 6000 mm/min, and a completely different material, 15 wt% carbon black-doped acrylonitrile butadiene styrene (**Table 3-5** and **Table 3-6**). When the layer's width was changed from 0.3 mm to 0.5 mm, the Z/F ratio was found to change from  $2.99 \pm 0.2$  to  $1.75 \pm 0.16$ . In addition, when the layer's height was changed from 0.14 mm to 0.26 mm, the Z/F ratio was constant; Z/F ratio of  $2.26 \pm 0.21$  and  $2.22 \pm 0.19$  was obtained for 0.14 mm and 0.26 mm, respectively. These values are in proximity to  $2.15 \pm 0.23$  that were reported here using carbon black-doped PLA.

However, if the geometry is complex, consisting of varying cross-section, then predicting electrical impedance becomes a difficult task. Presently, mechanical properties of complex 3D geometries can be estimated by combining voxelization to define material property at an individual voxel level with commercial finite element analysis such as ANSYS and ABAQUS. Alternatives such as Digimat AM and Genoa 3DP integrate this in to one commercial design solutions. Similarly, electrical impedance of complex 3D geometries could be estimated if the scaling law for impedance with the number of bond interfaces was known along with how it varied with the change in print parameters.

**Table 3-5:** The Z/F ratio of Zhang *et al.* work with variation in raster width with variation and their corresponding standard deviation.

W	Vertical	Horizontal	Z/F	p-value		
0.3	154±10	51.5±1	2.99±0.2	0.004		0.001
0.4	108±7	50.2±1.2	2.15±0.15		0.03	
0.5	89±8	50.7±1.2	1.75±0.16			

**Table 3-6:** The Z/F ratio of Zhang *et al.* work with variation in layer height with variation and their corresponding standard deviation.

h	Vertical	Horizontal	Z/F	p-value		
0.14	111±10	49±1	2.26±0.21	0.572		0.819
0.2	121±19	49.8±1.2	2.42±0.4		0.477	
0.26	119±10	53.6±1	2.22±0.19			

To understand how the impedance scales with the number of interfaces, Z-samples that allowed probing different number of bond interfaces in samples printed with extreme parameters - high/low print speed and high/low extrusion temperatures were created. **Figure 3-8** shows the impedance measurements obtained using these Z-samples. Like the observations made above, the single bond interfaces printed with a high extrusion temperature showed lower impedance compared to interfaces printed with a low extrusion temperature; the variation of print speeds was found to have negligible impact on the impedance. A good linear fit ( $R^2 \geq 0.98$ ) was found between the impedance and the number of interfaces. This implies that the tests of single interfaces can be used to predict the results over multiple interfaces, thus allowing us to study the effects of multiple parameters in a relatively short time. The slopes in **Figure 3-8** indicate how the

impedance scales with a number of interfaces and the intercept indicates the contact resistance. The slopes were found to be significantly different for samples printed with different extrusion temperature; low extrusion temperature had a slope of 12.42-12.68  $\Omega$  per interface, while high extrusion temperature had a slope of 6.30-6.69  $\Omega$  per interface. From **Figure 3-6**, we also learned that the interface contributes two-thirds while the fiber bulk contributes one-third of the impedance. This shows that the impedance due to the interface is also inversely proportional to the extrusion temperature and not a function of the print speed. Furthermore, the doubling of slopes from high to low extrusion temperatures implies that printing an electrical bus or wire with low extrusion temperature would require twice the cross-section area compared to printing with high extrusion temperature.

### 3.3.3 Understanding the Structure of the Interface

The anisotropy in electrical property can also be addressed through materials engineering approach, where if one understands what leads to the high impedance at the bond interfaces, one could engineer the composition or using additives that reduce the impedance at the bond interfaces. The high impedance at the bond interface could be attributed to either the existence of large voids or also called air pockets at the interface resulting from air being trapped during 3D printing [83], altered distribution of carbon black between the fiber bulk and the interface, or oxidation of the interface during MEAM. To locate voids, the morphology using scanning electron microscopy (SEM) is studied. To probe the distribution of carbon particles or identify extensive oxidation at the interface, elemental distribution using energy dispersive spectroscopy (EDS) is studied. The samples were prepared by freeze-fracturing using liquid nitrogen. The interface in a

freshly fractured surface under an SEM (see **Figure 3-7**) shows the PLA matrix that resembles a foam-like structure, and the carbon black particles occupying the pores in the foam-like structure. Comparing the samples printed with high and low extrusion temperature in **Figure 3-9**, large voids ( $>5\ \mu\text{m}$ ) were not seen at the interfaces, and the morphology along the bond line was almost identical.

Next, alteration in the distribution of carbon black at the interface was studied, which will alter the percolation network, change the contact area between adjacent carbon black particles relative to their sizes and increase resistance locally similar to constriction resistance observed in sintered materials. In composite filaments containing microparticles such as carbon black, the particles are typically suspended in the PLA matrix using coupling agents containing either silicon, titanium, or zirconium to improve adhesion between polymers and filler-particles and achieve homogeneous suspension. Since the conductive PLA adopted here is a proprietary blend of conductive carbon black in PLA, efforts to reverse engineer were minimized during this study. The EDS measurements in **Figure 3-10** show negligible amount of silicon, but no titanium (4.5 keV) and zirconium (2.05 keV) were detected; hence, no other element was used as a coupling agent. A line scan across the interface shows even distribution of oxygen and silicon as seen from the Oxygen/Carbon (O/C) ratio plot across the interface in **Figure 3-10b**. This shows that the interface does not show extensive oxidation at the interface. Our group is currently working on using chemical characterization techniques such as FTIR and Raman spectroscopy to provide further insights to the root cause of increase impedance at the interface. Meanwhile, a parallel approach needs to be taken to reduce the interfacial impedance using additives such as surfactants for carbon black, metal

nanoparticles, and electrically conductive thermoplastics. Such additives could not only reduce the Z/F ratio, but also address the observed change in resistivity with extrusion temperature.

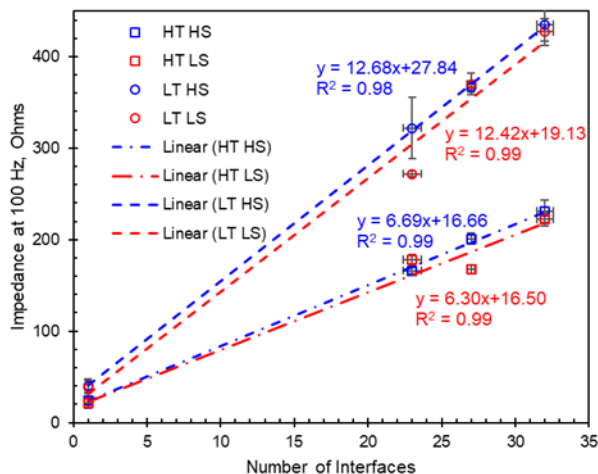


**Figure 3-8:** Scaling of impedance with several bond interfaces. In the legend, HT stands for high extrusion temperature 230 °C, LT for low extrusion temperature 190 °C, HS for high print speed 2000 mm/min, and LS for low print speed 750 mm/min. Vertical and horizontal error bars indicate standard deviation in impedance recorded and the number of interfaces probed, respectively, over three independent trials for three samples in each case.

To probe the distribution of carbon particles or identify extensive oxidation at the interface, elemental distribution using energy dispersive spectroscopy (EDS) is studied. The samples were prepared by freeze-fracturing using liquid nitrogen. The interface in a freshly fractured surface under an SEM (see **Figure 3-7**) shows the PLA matrix that resembles a foam-like structure, and the carbon black particles occupying the pores in the foam-like structure. Comparing the samples printed with high and low extrusion temperature in **Figure 3-9**, large voids ( $>5\ \mu\text{m}$ ) were not seen at the interfaces, and the morphology along the bond line was almost identical.

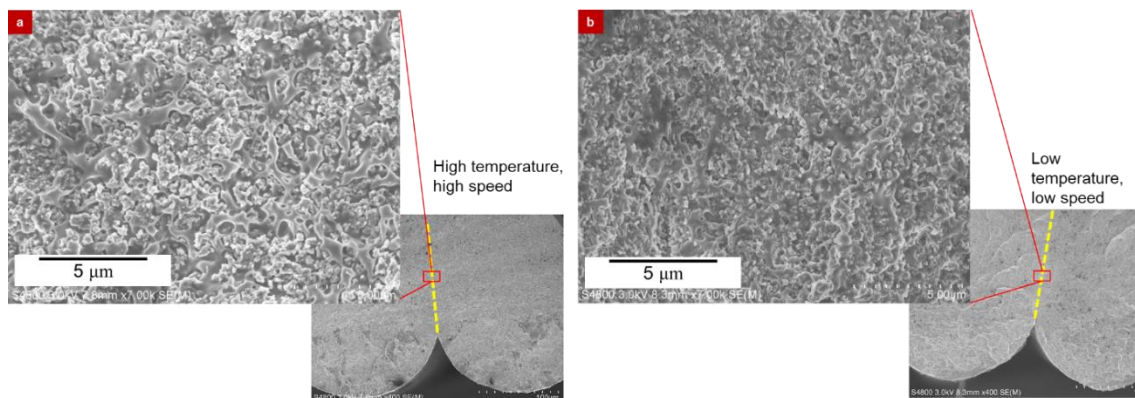


**Figure 3-9:** Scanning electron microscope images of the interface obtained after liquid nitrogen-assisted fracturing of a) a high temperature, high speed sample, and b) a low temperature, low speed sample.

Next, alteration in the distribution of carbon black at the interface was studied, which will alter the percolation network, change the contact area between adjacent carbon black particles relative to their sizes and increase resistance locally similar to constriction resistance observed in sintered materials. In composite filaments containing microparticles such as carbon black, the particles are typically suspended in the PLA matrix using coupling agents containing either silicon, titanium, or zirconium to improve adhesion between polymers and filler-particles and achieve homogeneous suspension. Since the conductive PLA adopted here is a proprietary blend of conductive carbon black in PLA, efforts to reverse engineer were minimized during this study. The EDS measurements in **Figure 3-10** show negligible amount of silicon, but no titanium (4.5 keV) and zirconium (2.05 keV) were detected; hence, no other element was used as a coupling agent. A line scan across the interface shows even distribution of oxygen and silicon as seen from the O/C ratio plot across the interface in **Figure 3-10b**.

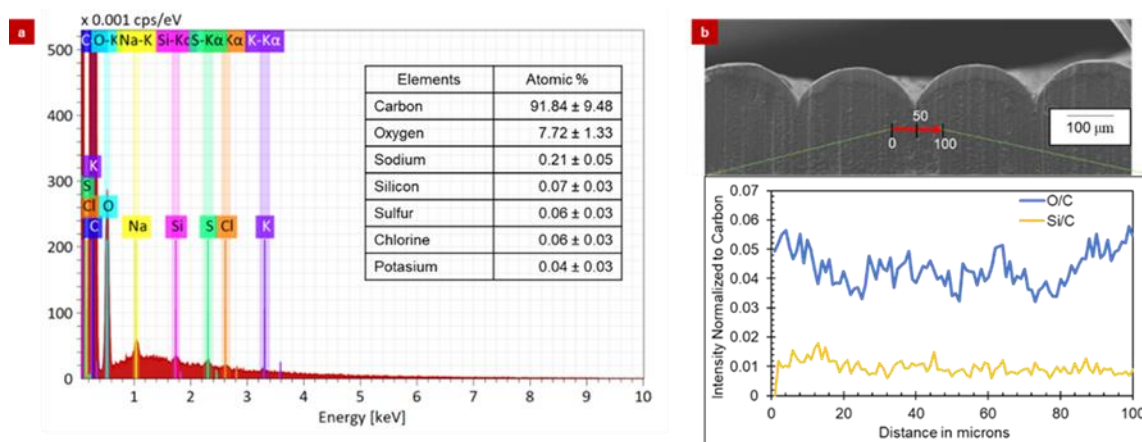


**Figure 3-10:** Studying the interface to identify surfactants (a) EDS spectrum of the carbon black doped PLA filament. (b) EDS line across the interface for a high temperature, high speed sample.

This shows that the interface does not show extensive oxidation at the interface.

Our group is currently working on using chemical characterization techniques such as FTIR and Raman spectroscopy to provide further insights to the root cause of increase impedance at the interface. Meanwhile, a parallel approach needs to be taken to reduce the interfacial impedance using additives such as surfactants for carbon black, metal nanoparticles, and electrically conductive thermoplastics. Such additives could not only reduce the Z/F ratio, but also address the observed change in resistivity with extrusion temperature.

### 3.4 Conclusion

In summary, using a hollow box structure that allows examining the interlayer bonds carefully the anisotropy in electrical conductance of MEAM prints arises due to the bond interfaces was demonstrated. Two types of samples were fabricated: Z-samples and F-samples measuring the impedance across and along the fiber orientation, respectively. Using these samples printed with three extrusion temperatures and four print

speeds, we have shown that the extrusion temperature has a significant impact on the electrical impedance arising due to the bond interfaces, while print speed has no noticeable impact. The impedance of F-samples also showed that the conductance of the extruded filament increased with the extrusion temperature. Taking a Z/F impedance ratio allowed compensating for such change in material property due to the extrusion temperature and teasing out the result that higher extrusion temperature leads to a lower interfacial impedance. The foundation for two types of future studies was laid out. One is a set of studies that allow measuring the empirical scaling laws for electrical impedance across bond interfaces and another is a set of studies that examine the root cause for higher impedance at the bond interface.

Assuming that the impedance of the fiber bulk is small compared to that of the interface, the interfacial impedance for the PLA-carbon black prints was found to scale linearly with the number of interfaces and the slope was dependent on the extrusion temperature. Studies of the morphology and elemental analysis of the bond interface using SEM and EDS warrant the need to use chemical characterization techniques that examine the distribution of carbon black. To investigate the interface further, mapping the chemical composition at the interface using infrared or Raman spectroscopy is suggested, or the distribution of the voids in the interface, which could cause anisotropy in the flow of charges. Thus, this study provides insights to predict electrical properties of MEAM prints based on design and print parameters.



## **CHAPTER 4**

### **HOT WIRE ANEMOMETER MADE COMPLETELY VIA MEAM**

#### **4.1 Introduction**

With the growth of material extrusion-based additive manufacturing (MEAM), which is commonly called 3D printing, it has become possible to print prototypes rapidly, and cost effectively. MEAM's advent into fields like electronics [5-10], RF electronic [11-14], microfluidics [15-19], medical [20-25], and robotics [26-28] is a testimony of its rapid growth. New possibilities are now in sight because of the ever-expanding capabilities of 3D printers and novel filaments available commercially. In Chapter 2, the characterization of microstructure and temperature dependence of resistance of two commercially available electrically conductive polylactic acid composites as-received and after MEAM [76]. A conductive PLA (c-PLA) showed a positive temperature coefficient of resistance between 0.03 and 0.01 °C<sup>-1</sup> before and after MEAM; this is high compared to that for metals that are commonly used in sensing applications (example: 0.004 °C<sup>-1</sup> for Pt). Similar electrical properties of c-PLA and metal counterparts make c-PLA an attractive filament for sensor development. Further, MEAM provides an advantage of printing a sensor integrated with fluidics; this eliminates the need for packaging.

SY Wu *et al.* [84] demonstrated basic microelectronic components like conductors, capacitors, and resistors with 3D printing and liquid metal paste filling techniques. The team developed a smart cap for monitoring the quality of milk by incorporating an LC circuit with it. The deterioration of milk is indicated by the change of the resonant frequency of the LC circuit. A 4.3% frequency shift was observed. Kari Anderson *et al.* [85] 3D printed an integrated system of 8 parallel fluidic channels that had a membrane insert containing cell cultures. The device demonstrated reusability, which is not an option in other drug studying devices. Though there is research that uses 3D printing in integrated systems, 3D printed parts are only an element of the whole system. In other words, they are not completely 3D printed.

In this paper, results from our simulation and experimental efforts on a completely 3D printed flow sensor operating based on the principle of hot wire anemometry are reported. The principle of Joule heating was used to heat a c-PLA wire packaged inside a fluidic capillary. The colder flow of nitrogen was expected to change the wire temperature, resulting in a change in the electrical resistance of the wire. Experimentally measured electrical and thermal properties of c-PLA were used in finite element simulations to predict the device's behavior. Furthermore, MEAM was used to print the simulated sensor design and characterize it using a nitrogen flow of 0-100 sccm.

## 4.2 Material and Methodology

### 4.2.1 Modeling and Simulation

The flow sensor was designed using Autodesk Fusion 360. As shown in **Figure 4-1a**, the flow sensor was 25 mm long, 10 mm wide, and 8 mm tall. A capillary 1 x 1 sq. mm was designed to run through the length of the sensor. A 0.3 mm thick heating

element with a 1 x 1 sq. mm was suspended across the capillary with a clearance of 0.3 mm below it and 0.4 mm above it. The sensor design was saved to a '.stl' file and imported into COMSOL Multiphysics 5.2a. The model geometry consisted of three domains: the conduit fluid, the body, and the sensor.

We modeled the body domain with the properties of ABS. The sensor domain was modeled with the properties of c-PLA. Material properties for ABS and cPLA were specified based on experimental data. For ABS, the heat capacity, density, and thermal conductivity were set to 1000 J/(kg·K) [86], 1050 kg/m<sup>3</sup> [87], and 0.29 W/(m·K) [87], respectively. For c-PLA, the density, heat capacity, and thermal conductivity were set to 1210 kg/m<sup>3</sup>, 1536 J/(kg·K), and 0.366 W/(m·K), respectively [80]. Relative permittivity, reference resistivity, and temperature coefficient of resistivity for the c-PLA were set to 9 [81], 0.018  $\Omega \cdot m$  at 298.15 K [76], and 0.02 K<sup>-1</sup> [76], respectively. The resistivity of the c-PLA was modeled linearly as a function of temperature. The convective heat loss from the overall geometry to the surrounding air (298.15 K) was modeled using an approximate heat transfer coefficient of 10 W/(m<sup>2</sup>·K). The electrical and heat transfer analyses were coupled through temperature values. The fluid domain was modeled as a weakly compressible, laminar flow of nitrogen with a no-slip boundary condition at the conduit walls. A mass flow boundary condition was specified at the inlet. A mesh convergence study showed that a fine mesh adequately predicted results within a reasonable time.

#### 4.2.2 MEAM for Empirical Experimentation

The model was imported to Simplify 3D as two different '.stl' files and then axially aligned so that they can be printed with two different filaments. The design was

then printed with 100% infill, no floor nor ceiling, 0.3 mm thick layers, single perimeter, and rectangular pattern, at a speed of 4800 mm/minute. The two filaments used were Proto-pasta c-PLA and MakerGear ABS. With ABS making up the body of the flowmeter and the channel, whereas heating element was printed using c-PLA. A MakerGear M2 V4 Rev E was used to print the flowmeter. The extruders were heated up to 230 °C and the heater bed taped with Kapton was heated to 120 °C. **Figure 4-3d** shows the fully printed flowmeter.

#### 4.2.3 Thermal Imaging

To visualize Joule heating, an open sensor with the heating element visible was printed. To reduce the contact resistance, conductive stainless-steel electrodes were soldered to the heating element as shown in **Figure 4-4a**. A source measuring unit (SMU) was hooked up to the electrodes to heat it by applying voltage. Kickstart 2.0.3 was used to manage the settings of the SMU using a computer. Keithley KUSB-488B was a necessary interface between the computer and the SMU. The magnitude and distribution of the temperature around the sensor was studied using an FLIR A325sc thermal camera. The accompanying FLIR Research IR software allowed controlling the camera using a computer. The camera was clamped on a tripod for stable imaging and the sample was made to stand erect and to ensure stability the sample was epoxied to a 3D printed block. The setup is shown in **Figure 4-4b**.

#### 4.2.4 Flow Calibration

A 0-120 sccm Brooks 1250-55 series rotameter was used to control the nitrogen flow to the sensor. The ¼” tubing from the regulated flowmeter was connected to a 21-gauge steel capillary, which was fixed to the channel using an epoxy; the connections

were leak tested with soapy water. Electrical contacts with the fully printed sensor were established as described above for the half-printed sensor. Electric potential of 12 and 15 V was applied across the sensor and the flow rate was incremented by 20 sccm every 90 s from 20 to 100 sccm. The first injection was done after 4 min to let the sensor heat to a steady temperature with a steady current flowing through it. The ambient temperature of the setup was 20 °C and the injected nitrogen was at 18 °C.

### 4.3 Results and Discussion

#### 4.3.1 Multiphysics Simulation

**Figure 4-1 (b-c)** shows the steady-state solution for temperature along the horizontal cross-section of the sensor and confirms the proper coupling between the electromagnetics, fluid dynamics, and heat transfer modules within our simulation efforts. Simulation results with low and high flow rates are presented in **Figure 4-1b** and **Figure 4-1c**, respectively. The simulations predict that the electric current density would be higher at the sensor bridge, which would result in comparatively higher Joule heating of the bridge. The nitrogen around the bridge, depending on the flow rate, will cool the bridge, which would then be detected by a change in resistance.

Further, the nitrogen that leaves the conduit will be hot compared to that entering. This is expected due to the drop in boundary layer thickness with an increase in the flow rate. **Figure 4-1d** and **Figure 4-1e** quantifies the relative change in temperature of the bridge and sensor resistance, respectively, as a function of the flow rate; results from simulations with 2.5, 3.2, and 3.9 V applied across the sensing element are presented. At either bias, the relative change in sensor resistance and bridge temperature could be approximated as a linear function of the flow rate with some error. The studies here were

limited to the use of 3.9 V to restrict the maximum temperature of the sensor to 50 °C, well below the glass transition temperature of PLA. As shown in **Figure 4-1f**, the use of higher voltage increased the exiting gas temperature by less than 5 K.

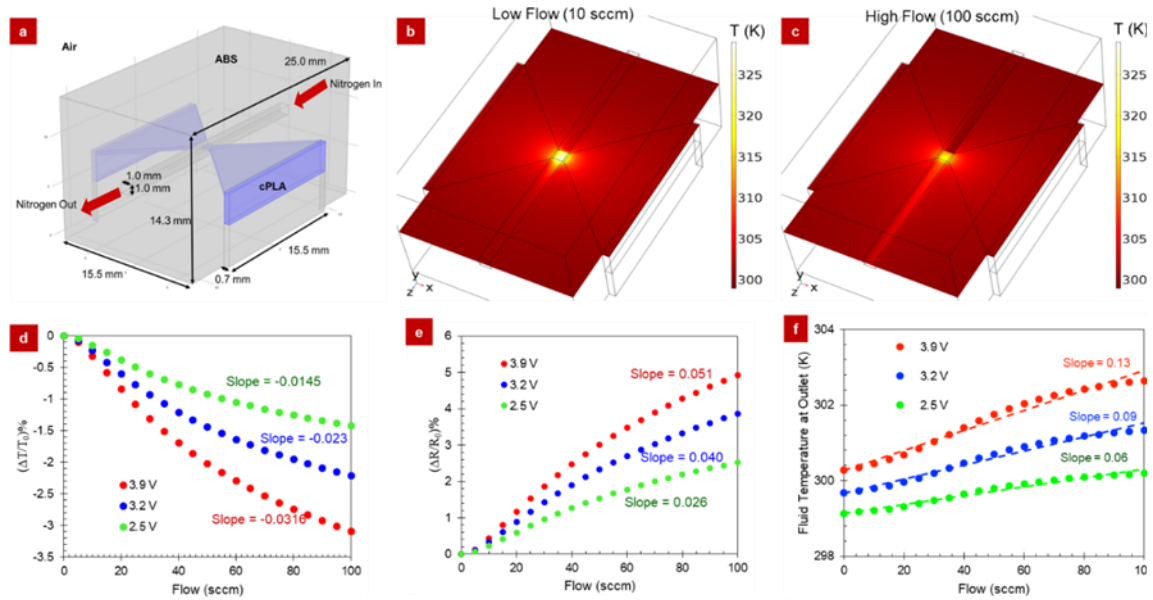


**Figure 4-1:** Steady-state simulation of the flow sensor design. (a) Sensor design simulated in COMSOL with the sensor consisting of ABS and c-PLA domains, surrounded by Air, and nitrogen flowing through the conduit. (b) The steady-state temperature distribution along the horizontal cross-section of the sensor with a 3.9 V applied across the sensor element and a 10 sccm of nitrogen flowing through the conduit. (c) A similar steady-state solution with 100 sccm of nitrogen flow. (d) The relative change in sensor wire temperature obtained as a function of the flow rate at different bias (3.9 V– red dots, 3.2 V– blue dots, and 2.5 V– green dots) applied across the sensor element. (e) The corresponding relative change in sensor resistance obtained at different flow rates. (f) The resulting fluid temperature at the outlet as a function of the flow rate and operational voltage. The dashed lines in (d-f) indicate a linear regression of the data with slope value indicated by text in respective color.

Further, transient simulations were used to predict real-time sensing characteristics. **Figure 4-2(a-b)** show that when the flow rate is fixed and the voltage applied across the sensing element is varied, the bridge temperature or the sensor resistance increases and plateaus at nearly the same time regardless of the voltage applied. The response time was defined as the time required in transient simulations to

achieve  $\geq 95\%$  of the change in resistance predicted via steady-state simulations. The response time was found to be  $\sim 10$  s. **Figure 4-2c** shows that the bridge temperature and sensor resistance at 10 s were linearly dependent on the voltage, 2.33 K/V and 3.92  $\Omega$ /V, respectively. **Figure 4-2d-e** show that when the voltage is fixed and the flow rate is varied, the bridge temperature or the sensor resistance plateaus at nearly the same time.

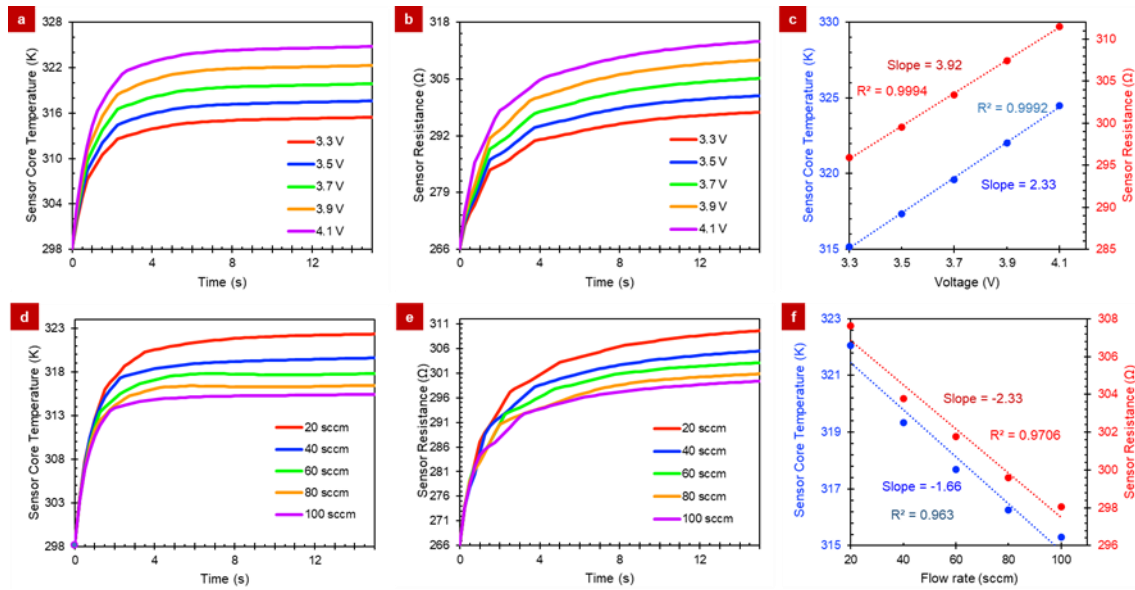


**Figure 4-2:** Transient simulation of the flow sensor. (a) The sensor core temperature and (b) the sensor resistance as a function of time for different operational voltages (3.3 V – red, 3.5 V – blue, 3.7 V – green, 3.9 V – orange, 4.1 V – magenta) and a fixed flow rate of 20 sccm. (c) The sensor core temperature (in blue) and sensor resistance (in red) at 10 s plot as a function of operation voltage. (d) The sensor core temperature and (e) the sensor resistance as a function of time for varying flow rates (20 sccm – red, 40 sccm – blue, 60 sccm – green, 80 sccm – orange, 100 sccm – magenta) and a fixed operational voltage of 3.9 V. (f) The sensor core temperature (in blue) and sensor resistance (in red) obtained at 10 s plot as a function of the flow rate. The dashed lines in (c and f) indicate a linear regression of the data with slope value indicated by text in respective color.

There is a time lag between the core temperature and the resistance plateauing because the temperature is measured only at the core, whereas the resistance is measured across the entire contact pad, and the contact pads are still heating up. **Figure 4-2f** shows

that the bridge temperature and sensor resistance obtained at 10 s was not exactly a linear function of the flow rate; however, a linear approximation showed a sensitivity of -1.66 K/sccm and -2.33  $\Omega$ /sccm. Instead, by plotting the % relative change in the resistance obtained at 10 s versus the flow rate as shown in **Figure 4-5**, a linear flow sensitivity of 0.036 sccm<sup>-1</sup> was predicted.

#### 4.3.2 Flowmeter Experimental Investigation

The 3D model parts assembled to print the flow sensor and a picture of a completely 3D printed flow sensor is shown in **Figure 4-3**.

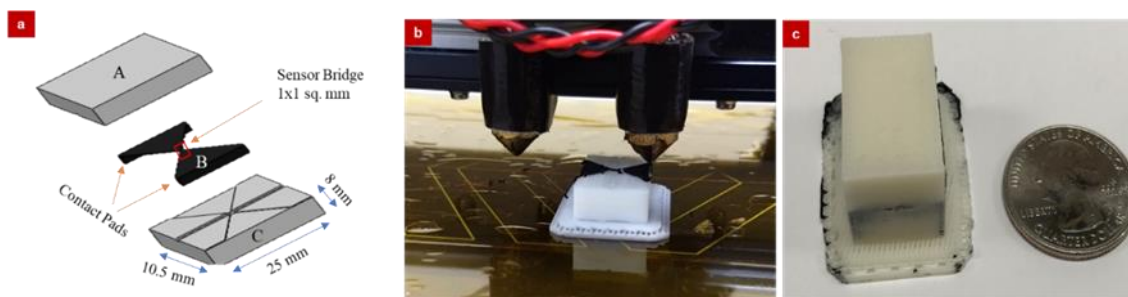


**Figure 4-3:** A completely 3D printed flow sensor. (a) Model parts that were imported into the 3D printer software (Simplify 3D). The non-conductive sensor top (A) contains a trench, 1 mm wide and 0.7 mm deep running along the length on the bottom face. The conductive sensing element (B) consists of a 1x1 sq. mm hot-wire. The non-conductive sensor bottom (C) also consists of a trench (1 mm wide and 0.3 mm deep). (b) 3D printing the sensor with MakerGear M2 V4 Rev. E with the left extruder printing cPLA and the right extruder printing ABS. The raft at the bottom ensured better adhesion to the print bed. (c) Completely 3D printed flow sensor alongside a US quarter.

Although the bed was lined with Kapton tape (1 mil thick) and heated to 120 °C, it was necessary to print the sensor with a raft (3 layers thick, 85% infill, and 3 mm offset from the part). The challenge during printing was to keep a continuous flow of c-PLA, which forms a relatively small volume fraction of the final print. The trick was to print a dummy c-PLA print next to the flow sensor. Another challenge was to prevent cross-



contamination of the nozzles, and thus create distinct ABS part without c-PLA traces and vice versa. This challenge was overcome by cleaning the nozzles in between prints.

For a proof-of-concept, the printed sensor without the cap (part ‘A’) as shown in **Figure 4-4a** and tested as shown in **Figure 4-4b**. This allowed us to use an IR camera to verify that the bridge shows significant Joule heating compared to the connector body. Upon application of voltage to the sensor, it takes less than 10 s to achieve a steady resistance without forced convection (shown in **Figure 4-4c**).

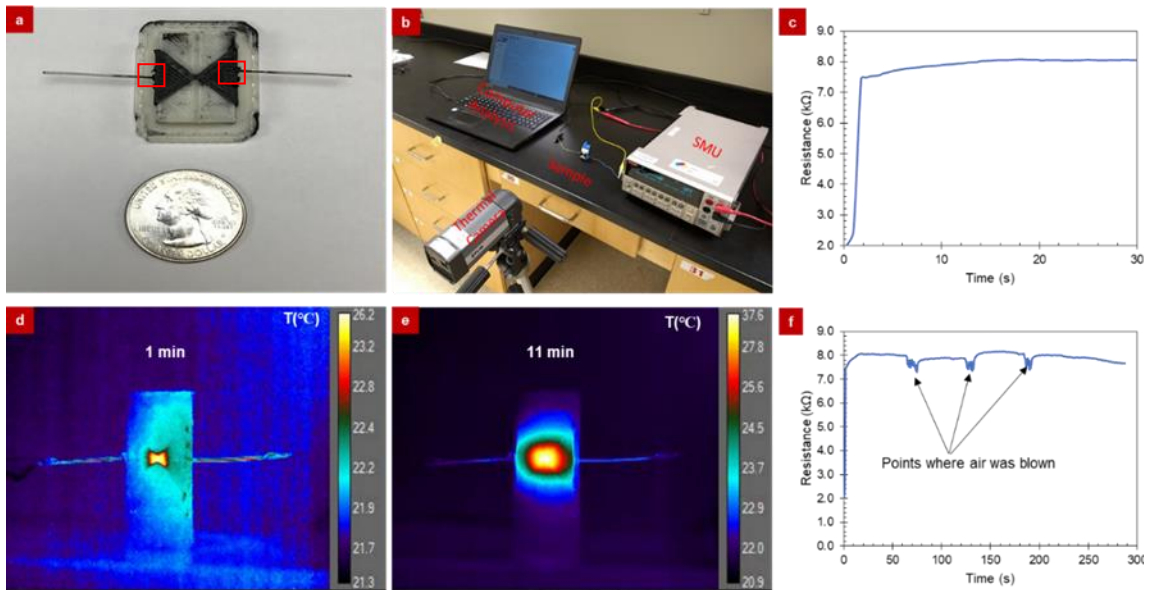


**Figure 4-4:** Thermal image observing the Joule heating of the flow sensor. (a) Half printed sensor with stainless steel electrodes providing electrical contact as pointed by the red squares. (b) Setup for thermal imaging with the FLIR A325sc thermal camera clamped on a tripod pointed to the half-printed flow sensor. The source-measurement unit (SMU) was used to supply bias and record the current across the sensing element. Image capture and analysis of thermal data was performed on a portable computer. (c) Resistance as a function of time shows that the resistance steadies out in less than a minute. Thermal image obtained (d) 1 minute, and (e) 11 minutes. (f) A proof-of-concept sensing shown notes the resistance while air was blown at specific time points.

A significant difference in resistance values between the simulation and experiment was noted. One factor could be the higher resistivity of the triangular contact

pads. Due to the layer-by-layer nature in which the contact pad was printed and the resulting inter- and intra-layer contact, resistances and porosity could attribute to the significant electrical resistance.

Regardless, the overall resistance of the contact pads was less than that of the wire as shown by the Joule heating observed with a FLIR camera. This points to either the wire dimension being smaller than the design, or a different resistivity than that measured in our last publication. The exact underlying cause for discrepancy in the device's resistance between simulation and the experiment remains a question and open for further investigation. Therefore, the use of voltages in the range of 7 V to 15 V was necessary. The anemometer consumed a power of 50 – 60 mW. The thermal camera recording confirming that the bridge temperature hits a steady state at about 2 min with application of 7 V. **Figure 4-4d** shows a thermal image at 1-minute confirming that significant Joule heating takes place in the bridge compared to the connectors. **Figure 4-4e** shows a thermal image recorded at 11 minutes showing that the bridge continues to be the hottest part reaching a maximum temperature close to 37 °C, and the connectors also heat up. **Figure 4-4f** shows that when air was exhaled over the sensor, the sensor resistance decreased. This provided proof of the principle to build and test the complete flow sensor. The heat transfer coefficient ( $h$ ) of the flowmeter was calculated theoretically and the results were verified. To calculate  $h$  in the cross flow over a rectangular wire, the following equation that is meant for cylindrical wires was appropriated:

$$Nu_{df} = \frac{hd}{k_f} = C \left( \frac{u_{\infty} d}{\nu_f} \right)^n Pr_f^{\frac{1}{3}} \quad \text{Eq. 4-1}$$

In **Eq. 4-1**,  $C$  and  $n$  are constants chosen based on the Reynold's number, which is given by the term  $u_{\infty} d / \nu_f$ ; where  $u_{\infty}$  is the freestream velocity of the gas through the

channel,  $V_f$  is the kinematic viscosity,  $d$  is the length of the sides of the wire,  $K_f$  is the thermal conductivity of air, and  $Pr_f$  is the Prandtl number for air, which is 0.7.

In this case, the Reynold's number turned out to be 108.1, which fell in the range that had a  $C$  and  $n$  value of 0.683 and 0.466, respectively. Since all the terms of the equation are known, the value of  $h$  can be determined by,

$$h = C \left( \frac{u_\infty d}{v_f} \right)^n \frac{Pr_f^{\frac{1}{3}} k_f}{d} \quad \text{Eq. 4-2}$$

$$h = 0.683 \left( \frac{1.65 * 0.001}{0.00001527} \right)^{0.466} * \frac{0.7^{\frac{1}{3}} * 0.024}{0.001} \frac{W}{m^2 K}$$

$$h = 130.57 \frac{W}{m^2 K}$$

The procured value of  $h$  can be verified against the theoretical calculation can be verified with the thermal camera readings by first solving for 'm' in the heat equation of a rod with a heat source, which is given by:

$$m = \sqrt{\frac{hP}{kA}} \quad \text{Eq. 4-3}$$

where  $h$  is the heat transfer coefficient;  $P$  is the perimeter of the hot-wire;  $k$  is the thermal conductivity of c-PLA; and  $A$  is the cross-sectional area of the hot-wire. Then,

$$m = \sqrt{\frac{120.5 * 4 * 10^{-3}}{0.13 * 1 * 10^{-6}}} = 1925.54$$

Solving for the differential equation describing the heat flow across a hot wire, we have:

$$\theta' = \frac{(\theta'_1 e^{2mL} - \theta'_2 e^{mL})e^{-mx} + (\theta'_2 e^{mL} - \theta'_1)e^{mx}}{e^{2mL} - 1} \quad \text{Eq. 4-4}$$

In this case,  $\theta_1 = \theta_2 = \theta$  and  $\theta = T_{end} - T_\infty - \frac{q}{km^2}$ ;

where,  $q$  is the power density of the wire.

Substituting the known values of the equation, we derive at a value of 34.81 °C, which is very close to the temperature observed with the FLIR thermal camera (i.e., 37 °C). The slight difference in the value of  $h$  that was theoretically derived and the value that produces a result closer to the empirical data can be attributed to the imprecision in the emissivity value set in the thermal camera. A total of three sensors were fabricated.

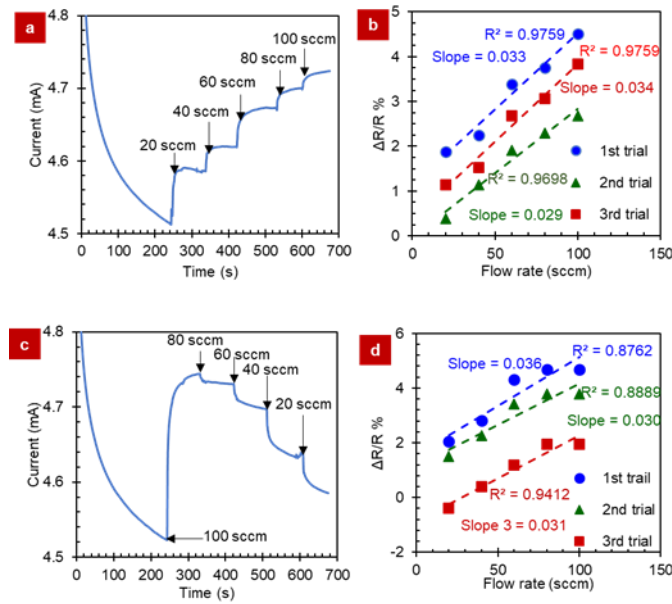


**Figure 4-5:** Flow sensing with the 3D printed sensor 1 at 12 V. (a) The current passing through the sensor during warm-up/stabilization with no flow and when the flow is stepped up to 100 sccm. (b) The relative change in sensor resistance recorded as a function of the flow rate from three different step-up trials (1st in blue circle, 2nd trial green triangle and 3rd trial in red square). The values used in the graph were obtained 45 s after the change in flow. (c) The current passing through the sensor during the stabilization phase with no flow and when the flow is stepped down from 100 sccm to 20 sccm. (d) The relative change in sensor resistance recorded as a function of flow rate from three different step-down trials (1st in blue circle, 2nd trial green triangle and 3rd trial in red square). Data provided in (a-d) was obtained using sensor 1. Similar data for sensors 2 is shown in **Figure 4-7** and **Figure 4-8**.

The results presented in the main text are the best obtained from one of the three tested sensors. Results from sensor 1 using 12 V are shown in **Figure 4-5** and the

increase in sensitivity with 15 V actuation bias is shown in **Figure 4-6**. Results of sensors 2 with actuation bias of 12 V and 15 V is shown in **Figure 4-7** and **Figure 4-8**.

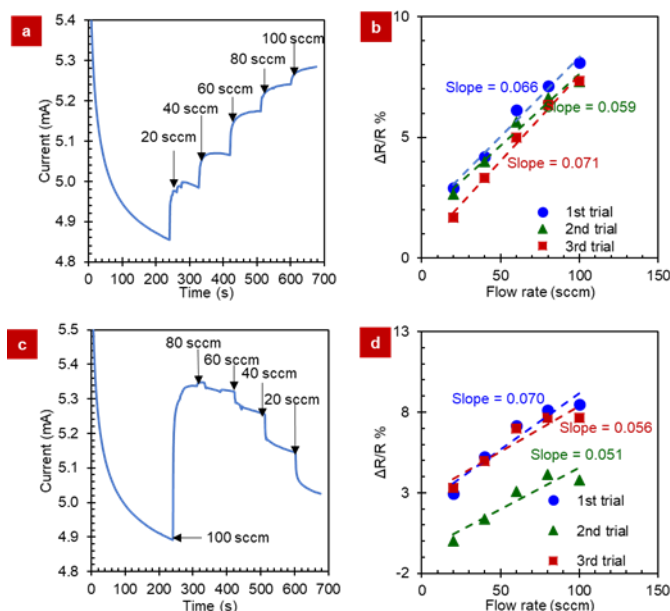


**Figure 4-6:** Flow sensing with the 3D printed sensor 1 at 15 V. (a) The current passing through the sensor during warm-up/stabilization with no flow and when the flow is stepped up to 100 sccm. (b) The relative change in sensor resistance recorded as a function of the flow rate from three different step-up trials (1st in blue circle, 2nd trial green triangle and 3rd trial in red square). The values used in the graph were obtained 45 s after the change in flow. (c) The current passing through the sensor during the stabilization phase with no flow and when the flow is stepped down from 100 sccm to 20 sccm. (d) The relative change in sensor resistance recorded as a function of the flow rate from three different step-down trials (1st in blue circle, 2nd trial green triangle and 3rd trial in red square). Data provided in (a-d) was obtained using sensor 1.

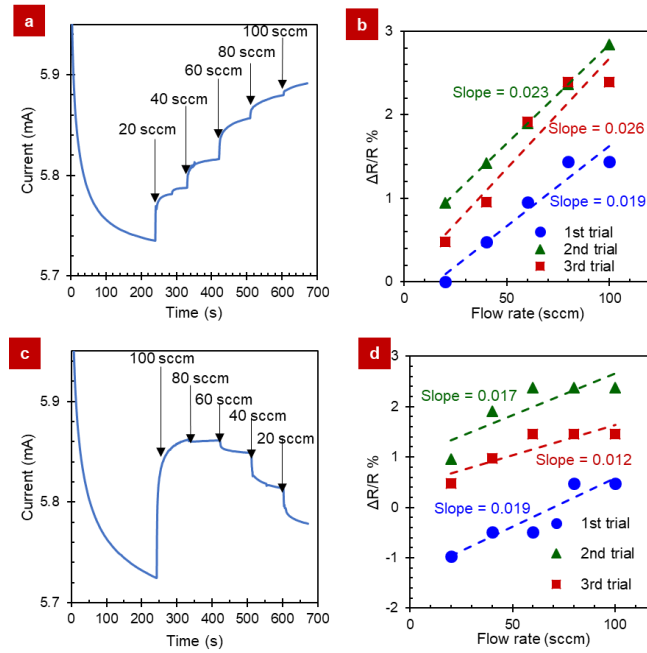


**Figure 4-7:** Flow sensing with the 3D printed sensor 2 at 12 V.

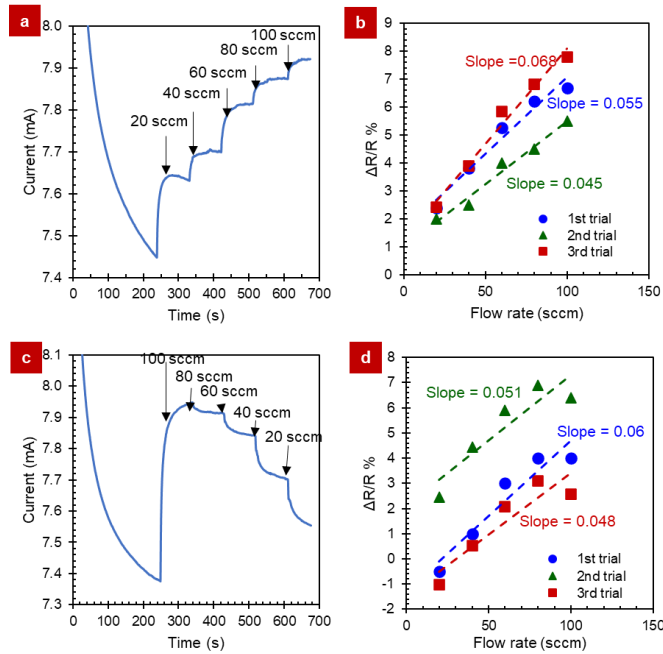


**Figure 4-8:** Flow sensing with the 3D printed sensor 2 at 15 V.

As can be seen, the application of voltage leads to a drop in the current. This is due to the positive temperature coefficient of c-PLA; when a potential is applied across

the sensor, it starts to heat up, further raising the resistance and decreasing the current. The sudden rise in the current level was seen upon change in nitrogen flow at times indicated by the arrows. The increase in current with flow rate was expected due to the increased cooling of the sensor and reduction in sensor resistance. To quantify, the resistance at 4 minutes (no flow, warm up stabilization) was considered as the reference and the relative change in resistance with respect to it ( $|\Delta R|/R\%$ ) was plotted against the nitrogen flow rate. The slope of this graph was inferred as the sensitivity of the flow sensor. **Figure 4-5b** shows the results for sensor 1 during three different trials when we ramped up the flow from 20 to 100 sccm. The relative change in resistance was found to be nearly a linear function of flowrate.

In anemometry, King's law describes the sensitivity as proportional to the square root of the flow velocity. The relationship is expressed as shown below:

$$E^2 = A + Bu^n \quad \text{Eq. 4-5}$$

where  $E$  is the applied voltage;  $A$  and  $B$  are constants; and  $u$  is the velocity of the gas flow. Using the experimental values,  $A$ ,  $B$ , and  $n$  were calculated to be 0.054, 0.001, and 0.682, respectively. In our study, since the flow rate was restricted to 100 sccm, the relationship between the flow rate and velocity seems to be linear, but when the obtained values are used for higher (until 300 sccm) values, it becomes clear that the linearity is the small part of a square root relationship between the flow velocity and sensitivity.

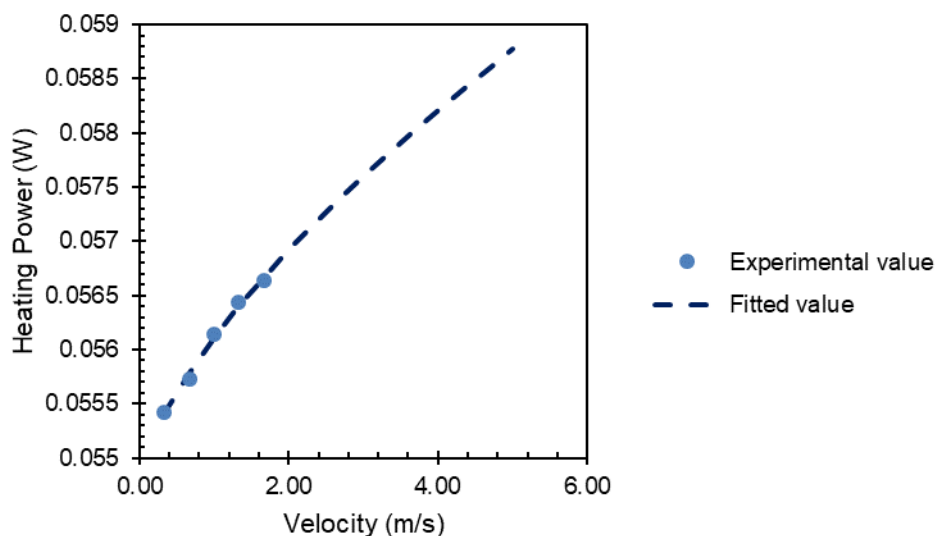


**Figure 4-9:** King's law relationship for the experimental value and the projected fitting value demonstrated.

An approximate sensitivity of  $0.032 \pm 0.003 \text{ sccm}^{-1}$  was found for the three trials.

This is very similar to the sensitivity of  $0.036 \text{ sccm}^{-1}$  obtained by simulation. **Figure 4-5c** shows the real-time response when the flow was ramped down from 100 to 20 sccm.

Initially when nitrogen is injected into the channel, the wire becomes cold and hence there is a spike in the current's increase. Every flow rate from then on is a decrease in the flow rate making the sensor hotter than it was previously, hence, the stair down effect.

**Figure 4-5d** shows the relative change in resistance recorded for three such ramp-down trials. Using the sensor, the difference between 80 – 100 sccm could not be differentiated; this is because the 90 s time interval between 100 sccm and 80 sccm set point was not enough for the sensor to equilibrate. However, below 80 sccm, the relative change in resistance was found to be a linear function of the flow rate with a sensitivity of  $0.032 \pm 0.003 \text{ sccm}^{-1}$  found over three trials for sensor 1 to have a response time of 18.5, 26.4,



40.7 for flows 40, 60, and 80, respectively, for a ramp-up and a response time of 29.0, 9.6, 29.61 for flows 60, 40, and 20, respectively, for a ramp-down.

To increase the sensitivity, the sensors were tested with higher voltages as suggested by the simulation results in **Figure 4-1d-e** and **Figure 4-2a-c**. Increasing the voltage  $\sim 17$  V on a sacrificial sensor led to heating the sensor close to the glass transition temperature, resulting in a disconnect at the bridge. Hence, the performances of sensors 1-3 at 15 V were characterized. **Figure 4-6** shows the performance of sensor 1 with 15 V in a similar manner as done with 12 V in **Figure 4-5**. **Figure 4-6a** shows the real-time response of the flow sensor with nitrogen injected at 20 sccm into the channel after 4 minutes and then ramped up to 100 sccm. **Figure 4-6b** shows the relative change in the resistance plot for sensor 1 during three different ramp-up trials. The linear sensitivity of relative change in the resistance was found to be between 0.059-0.071 sccm<sup>-1</sup>, which is nearly double than that obtained with 12 V. This is expected because the use of higher voltage is expected to lead to increased Joule heating and thus larger temperature drop (cooling) with gas flow. **Figure 4-6c** shows the real-time response when the flow was ramped down from 100 to 20 sccm. **Figure 4-6d** plots the relative change in the resistance recorded for three such ramp down trials.

Like **Figure 4-5**, with a 90 s equilibration time the sensor was unable to differentiate between 100 and 80 sccm due to the drastic flow change in this case. A linear flow rate sensitivity between 0.051 and 0.07 sccm<sup>-1</sup> was found below 80 sccm with a response time (95% change in resistance from its initial resistance) of 8.3, 36.4, 50.76 s for flows 40, 60, and 80 sccm, respectively, on the ramp-up and 64.7, 41.3, 31.1 s for flows 60, 40, and 20, respectively, for sensor 1. It is very interesting to observe that the

sensitivity is higher by a factor of 10 ( $\sim 0.1$ - $0.25$ ) of the sensors in simulation compared to the experimental data. However, in the simulation, the obtained sensitivity values were at lower voltages compared to the experimental results. The discrepancy is explained by the fact that COMSOL does not consider the anisotropic nature of 3D prints in its analysis.

**Table 4-1** shows a summary of the flow sensitivities recorded for sensors 1-3 with different tests. For a given sensor and operation voltage, the flow sensitivity for the ramp-up and ramp-down trials were statistically not very different. Sensor 1 was found to show better flow sensitivity with 12 V when compared to sensors 2 and 3, which seemed to give statistically similar responses ( $p = 0.23$  for ramp-up,  $p = 0.34$  for ramp-down). However, with 15 V the difference between the flow sensitivity for different sensors decreased; although mostly insignificantly different statistically, sensor 3 gave the lowest flow sensitivity. Most prominently, the flow sensitivity was found to increase with operational voltage, making it statistically similar ( $p = 0.1 - 0.43$ ) at 15 V, which may indicate an annealing behavior of the contact; however, the standard deviation in flow sensitivity was also found to increase. Thus, the higher operational voltages should be used with a caution to prevent melting of the bridge and achieving better measurement repeatability. In addition, a difference between the operational voltages required to produce similar results in the simulation and experimentally is seen. This can also be attributed to the non-Ohmic contacts and the porosity in the 3D printed contact pads, which may have led to a significant voltage drop. To the best of our knowledge of the existing literature available to us, this is the first demonstration of a completely 3D printed flow sensor.

**Table 4-1:** Flow sensitivity recorded for sensors 1-3 operate with 12 V or 15 V bias. Values represent average and standard deviation from results recorded in three different ramp-up or ramp-down trials. The p-values were calculated using an unpaired unequal variance t-test and represent the probability for the hypothesis that the flow sensitivities for the ramp-up and ramp-down trials are different. A p-value > 0.05 indicates the hypothesis is nullified.

	12 V		15 V	
	Ramp-up	Ramp-down	Ramp-up	Ramp-down
Sensor 1	$0.032 \pm 0.003$	$0.032 \pm 0.003$	$0.065 \pm 0.006$	$0.059 \pm 0.010$
	$p=0.897$		$p=0.406$	
Sensor 2	$0.014 \pm 0.009$	$0.020 \pm 0.005$	$0.056 \pm 0.012$	$0.053 \pm 0.006$
	$p=0.391$		$p=0.718$	
Sensor 3	0.023	0.016	$0.047 \pm 0.012$	$0.039 \pm 0.005$
	$p=0.084$		$p=0.375$	

The sensitivity and response times can be improved for a wide range of applications. The sensitivity may be increased by increasing the surface area of the heating element (using multiple bridges) and using conductive filaments with higher temperature coefficient of resistance. The response times can improve further by reducing the thermal time delay using conductive filaments with lower heat capacity. Further, the use of operational voltage can be reduced to 5 V using a low resistivity filament, which has a lower temperature coefficient of resistance to print the contact pads. Furthermore, the sensor design may be improved to address fluctuations in the gas flow direction, the temperature and humidity. In addition, the sensor may be adopted for sensing the flow of liquids. 3D printing will enable making such flow sensors on demand at a lower cost; the application of these flow sensors will be limited to lower operating temperatures and low flow rates. Using these flow sensors, there is a potential to develop integrated analytical

instrumentation such as a 3D printed gas chromatograph, where there is a need for tight fluidic integration of the components.

#### 4.4 Conclusion

In summary, a flow meter design was simulated using finite element modeling and experimentally verified. The steady-state simulations suggested a relative change in resistance with the flow rate between 0.027 – 0.051 sccm<sup>-1</sup>, depending on the operational voltage. Time-dependent simulations predicted a response time of 10 s to reach  $\geq 95\%$  of the steady-state values, suggesting the relative change in resistance to the flow rate of about 0.036 sccm<sup>-1</sup>. The Joule heating of the sensor was verified using an IR camera on an open channel flow meter design. The complete flow sensor with a closed capillary was successfully printed using intermediate cleaning of the nozzles. Three fully 3D printed sensors were characterized with a nitrogen flow ranging from 20-100 sccm.

Experimentally, a response time ranging from 9.6 to 40.7 s for 12 V and 8.3 to 64.8 s for 15 V was obtained with linear flow sensitivities ranging from 0.014 – 0.032 sccm<sup>-1</sup> with 12 V and 0.039 – 0.065 sccm<sup>-1</sup> with 15 V operation. To read the sensor accurately, an equilibration time of 45 s was necessary in most cases, and even more when using higher flow rates. The results show that 3D printed flow sensors hold potential for developing integrated analytical systems. Further investigations are warranted to investigate sensor designs that compensate for variations in temperature, humidity and direction of gas inflow, and improve the time-response (e.g. effect of the heating element's length and thickness). Triangular channels have been shown to be more effective in sensing so future studies can incorporate this design modification.

## **CHAPTER 5**

### **CHARACTERIZATION OF AN ELECTROTHERMAL CHEVRON GRIPPER FABRICATED BY EXTRUSION-BASED ADDITIVE MANUFACTURING**

#### **5.1 Introduction**

Ever since the invention of UNIMATE by General Motors, the usage of end effectors like pneumatic or motorized grippers has grown through optimization in design and material [88] for applications ranging from automated manufacturing to biomedical research. With the growth of Micro Electromechanical Systems (MEMS) in the last several decades, fabrication of actuators capable of controlled microscale motion is possible. Most MEMS actuators are structures that translate an input of electrical energy into mechanical motion. Depending on the working mechanism, micro-actuators are classified as, piezoelectric, electrostatic (capacitive), or electro-thermal. A piezoelectric actuator uses piezo ceramics to convert electrical energy into mechanical motion; an electrostatic actuator uses electrical input to create oppositely charged plates to attract each other. Electro thermal actuators either expand or contract when an electric potential is applied to them because of Joule heating. These three types of MEMS actuators have been used for gripping object from 100-200  $\mu\text{m}$  and achieving micron-scale displacements with high accuracy [89-91]. Various designs have been suggested and researched within each type of actuator. With the design for electrostatic actuators, there

are the comb [92], S-shaped [93], curved [94], and inchworm designs [95]. In the piezo-electric, there's bimorph [96] and expansion-based actuators [97]. Within the electro thermal type, there are the bimorphs [98] and solid expansion actuators [99]. Chevron type electro thermal actuators are extremely popular to produce high displacement with high resolution in comparison to their counterparts [100]. Micro-actuators are typically fabricated from silicon, but polymer (SU-8) based grippers have also been demonstrated for biological manipulation [101]. Although MEMS actuators have been widely successful, their production requires cleanroom facilities and a sizeable budget and yet only capable of producing 2.5D structures. With the advent of polymer additive manufacturing techniques like micro-stereo lithography, truly 3D structures are possible. Alblalaid *et al.* used projection stereo lithography of a liquid photopolymer and sputtered platinum thin film to achieve a chevron-type electro thermal gripper [102].

Recently, polymer additive manufacturing has been utilized for the realization of soft robots, which are less rigid and their designs mimic biological systems and organisms like worms, caterpillars, and octopus [103]. Based on the working principle, soft robotic grippers can be classified as pneumatic, hydraulic, or tendon based [104]. Pneumatic or hydraulic grippers use air or liquid pressure to actuate and thereby, hold or drop objects [105-107]. Similarly, tendon driven mechanism uses actual cables for actuation. All three types of actuators are extensively used in exoskeleton work for creating artificial muscle [108]. Material extrusion-based additive manufacturing (MEAM) has played a major part in the development of soft robotic grippers, specifically the pneumatic kind. Anver *et al.* used MEAM based thermoplastic polyurethane to fabricate a pneumatic-soft actuator [109]. Yap *et al.* also used MEAM method to make

pneumatic actuators from 3D printing material and methods and an important part of the testing was to measure failure by cyclic testing [110]. Drotman *et al.* design and reported a three pronged pneumatic actuator using a poly jet [105].

In the current literature on soft robotics, majority of the work has been done in developing pneumatic actuators. They are successful because of their tenderness and yet at the same time their ability to hold objects without damaging them. However, they are often slow to respond because of the higher volume change that is required for actuation [111] and require wiring. To our knowledge, there are no soft robotic elements that are MEAM using commercially available filament and electro thermally actuated. Shape memory polymer [112, 113], ionic polymer metal composites [114-116], and liquid crystal polymers [117-119] are thermally actuated but are used for biomedical applications and require extensive fabrication steps. Though most of the soft robotic work is done with soft polymers, there have been efforts to look for a compromise between the soft and rigid materials for creating compliant mechanism [111, 120]. In an interesting work where soft and rigid parts are combined, Elgeneidy *et al.* demonstrate a piezo-resistive sensor that was printed using conductive polylactic acid (c-PLA) inside a structure printed with NinjaFlex material that measures the strain of the external structure and demonstrate the sensor [121]. In this study, a chevron type electro thermal gripper is designed, Multiphysics simulation were performed on it, fabricated via MEAM, and characterized the displacement, actuation time and recovery. Thus, paving way for the development of altogether a new technology that evolves by the merger of the two different domains described in the previous paragraphs. The gripper is an electro-thermal actuator that relies on Joule heating for gripping that is light, inexpensive, performs the

action of gripping, has comparable output force, and the range of motion that is usually produced in a soft robotic actuator in proportion to its size. Our study will enable future researchers to use thermal actuation using conductive material for soft robotics or as the resolution of 3D printers improves, the actuator can be realized in a much smaller scale using MEAM.

## 5.2 Methodology

### 5.2.1 Modeling and Simulation

The CAD model of the gripper (see **Figure 5-1**) was designed in SolidWorks, converted to a .stl file, and imported into COMSOL. The gripper was partitioned into three electrically isolating ABS domains and one conductive PLA (c-PLA) domain. For ABS, the density, heat capacity, and thermal conductivity were set to  $1050 \text{ kg m}^{-3}$  [87],  $1000 \text{ J kg}^{-1}\text{K}^{-1}$  [86], and  $0.29 \text{ W m}^{-1}\text{K}^{-1}$  [87], respectively. For c-PLA, the density, heat capacity, and thermal conductivity were set to  $1210 \text{ kg/m}^3$ ,  $1536 \text{ J/(kg}\cdot\text{K)}$ , and  $0.366 \text{ W/(m}\cdot\text{K)}$ , respectively [80]. The relative permittivity, reference resistivity, and temperature coefficient of resistivity for the c-PLA were set to 9 [122],  $0.018 \text{ }\Omega\cdot\text{m}$  at  $298.15 \text{ K}$  (transient simulations only) [76], and  $0.02 \text{ 1/K}$  [76] respectively. Linear thermal expansion was modeled using a fixed coefficient of thermal expansion ( $171.2 \times 10^{-6} \text{ K}^{-1}$ ) for the c-PLA. COMSOL's Joule Heating and Thermal Expansion multi-physics interface was implemented, which conveniently included the Solid Mechanics, Heat Transfer in Solids and Electric Currents modules along with the proper couplings. Both ABS and c-PLA were defined as isotropic linear elastic materials. The Young's modulus (E) and Poisson's ratio ( $\nu$ ) were set to  $2 \text{ GPa}$  and  $0.36$  [51], respectively for ABS, and  $(1281 - 10.32 \cdot T) \text{ MPa}$  [80] and  $0.36$  [123], respectively, for c-PLA where T is temperature in  $^{\circ}\text{C}$ .



**Figure 5-1** shows the edge of the gripper body that was fixed in all directions and thermally insulated. The convective heat loss to the surrounding air (22 °C) was modeled using a heat transfer coefficient of 10 W/m<sup>2</sup>·K.

### 5.2.2 Fabrication by MEAM Sample

The design of the gripper was based on that of the conventional MEMS chevron thermal actuators as shown in **Figure 5-1a**. The design published by Alblalaih *et al.* was scaled up by 3 times to enable printing the hinges via MEAM [15]. The design consisted of conductive and non-conductive parts, which required a dual-extruder printer, MakerGear M3 V4 for printing conductive portions with c-PLA through a 0.5 mm diameter nozzle, and the non-conductive portions with ABS through a 0.35 mm diameter nozzle. The makers of the filament recommended the usage of two different nozzles. Using a smaller diameter nozzle for c-PLA resulted in improper extrusion of the filament. The two parts of the sample were designed as two different bodies in Fusion 360 and exported as two different '.stl' files to Simplify 3D. The appropriate extruders for the two filaments were assigned using the dual extrusion wizard. The sample was printed with a layer height of 0.3 mm, a rectangular layer pattern, a print angle of 90°, a bed temperature of 110 °C, an extrusion temperature of 230 °C, and a print speed of 4800 mm/min. The print angle was of paramount importance because the simulation results suggested that the lower resistance led to decreased response time and required lower actuation voltages. A print angle of 90° resulted in lower resistance.

### 5.2.3 Electrical Actuation by Source Measurement Unit (SMU)

Making electrical contacts that do not heat up significantly, as observed from the IR camera, was essential for proper operation of the gripper. Direct soldering of tinned

copper wire to c-PLA resulted in low adhesion strength. Sticking a hot wire into the c-PLA showed increased heating at the contacts and a drastically higher resistance.

Reduced contact resistance was found when using a layer of nickel paint (Super Shield™ – Nickel conductive coating) on the surface and then soldering a wire to the nickel layer (as shown in **Figure 5-1c**). The voltage required for gripper actuation was supplied by a source measurement unit (SMU), Keithley 2400, which allowed simultaneous measurement of the current or the resistance.

#### 5.2.4 Thermal Imaging

FLIR A325sc was used for thermal imaging of the sample. Thermal imaging was used to (1) ensure that the temperature of the chevrons in the gripper did not exceed 45 °C, which was a safety limit that was decided knowing that the glass transition temperature ( $T_g$ ) of PLA is ~60°C, (2) confirmed that the contacts did not heat up excessively upon application of voltage due to improper contact, and (3) study the heat flow in and around the chevrons.

Focus of the camera was vital for the accurate reading of temperature; best focus was achieved at 0.17 m from the sample as shown in **Figure 5-1c**. Temperature readings were collected from the FLIR camera using with a proprietary software, ResearchIR installed on a laptop. An emissivity value of 0.93 [124] was used. ResearchIR was also set a region of interest (ROI) encompassing the chevron and the shuttle where the maximum temperature was monitored.

The temperature, humidity, and airflow fluctuations in the lab environment drastically impacted the temperature measurements. Thus, a casing composed of aluminum-lined acrylic was made around the camera and the gripper.

### 5.2.5 Laser Doppler Vibrometer

A laser Doppler vibrometer (Polytec OFV 511 fiber interferometer) was used to measure arm displacement based on the phase difference between the emitted laser beam (620-690 nm) and the laser beam reflected from a retroreflector stuck to an arm of the gripper. As per the user manual, the vibrometer was set at 268 mm from the sample, as shown in **Figure 5-1c**, for effective measurement of the displacement.

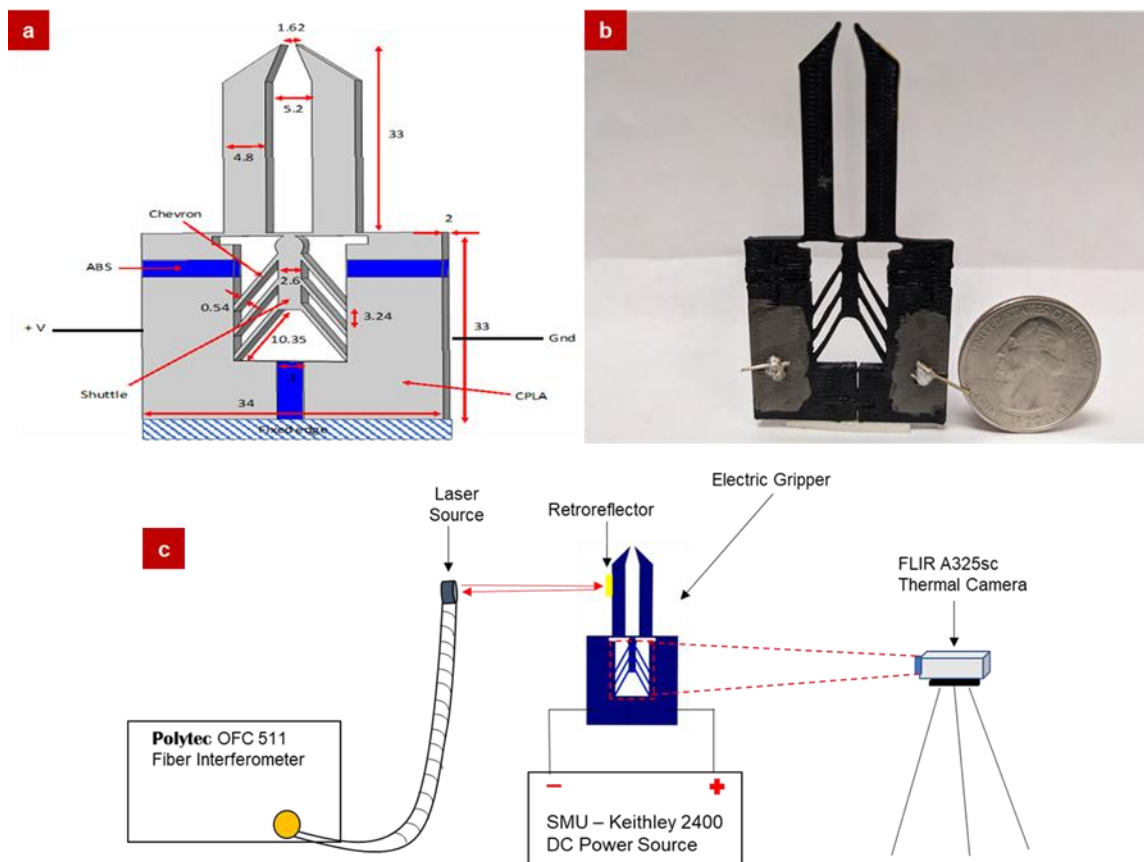


**Figure 5-1:** Gripper design and measurement setup. (a) Design and dimensions of the gripper; the grey colored parts were printed with c-PLA and the blue colored parts with ABS. The whole sample is ~ 6.6 mm tall and 3.4 mm wide. (b) A 3D printed electric gripper alongside a U.S. quarter dollar coin. The electrical contacts were achieved via nickel paint and soldering. (c) Test setup consisting of an SMU, laser Doppler vibrometer and a thermal camera was used to study the gripper actuation and recovery.

A retro-reflective tape glued to the tweezer arm was found to result in better reflectivity compared to generic reflective tapes. The experimental sequence consisted of turning of the IR camera to monitor the maximum temperature of the chevrons, 30 s later the vibrometer was initialized to record data, and 15 s later, the voltage was applied. Hence, a time lag of 30 s between the displacement and temperature curves was planned. The SMU was programmed to stop the application of voltage after a specified time. Finally, three minutes was given for the sample to cool down and zero displacement before the subsequent trials.

### 5.3 Results and Discussion

#### 5.3.1 Multiphysics: Steady-State Analysis

The steady-state finite element modeling was found to show that the gripper would actuate as desired, and that the resistivity plays a big role. As expected, the current density was found to be higher in the chevron beams as shown in **Figure 5-2a**. This resulted in the highest temperatures recorded in chevron and shuttle region as shown in **Figure 5-2b**. This confirms that the Solid Mechanics, Heat Transfer in Solids and Electric Currents modules were coupled during the finite element analysis. The highest temperature recorded in the chevron region during steady-state simulations was recorded as the potential applied across the gripper was increased. The power that results in Joule heating depends on the potential squared; thus, the dependence of temperature on the potential was expected to be parabolic. This was found to be true during the finite element simulation as shown in **Figure 5-2c**. The resistivity of a 3D printed part depends on the print parameters and the dimensions of the part. Thus, in finite element modeling, the resistivity of c-PLA defined at room temperature was varied to examine its impact on

the maximum temperature in the chevrons achieved via Joule heating and the resulting displacement at the tip. The maximum temperature reached during these simulations was capped below the glass transition temperature of c-PLA ( $T_g - 10 = 55\text{ }^{\circ}\text{C}$ ).

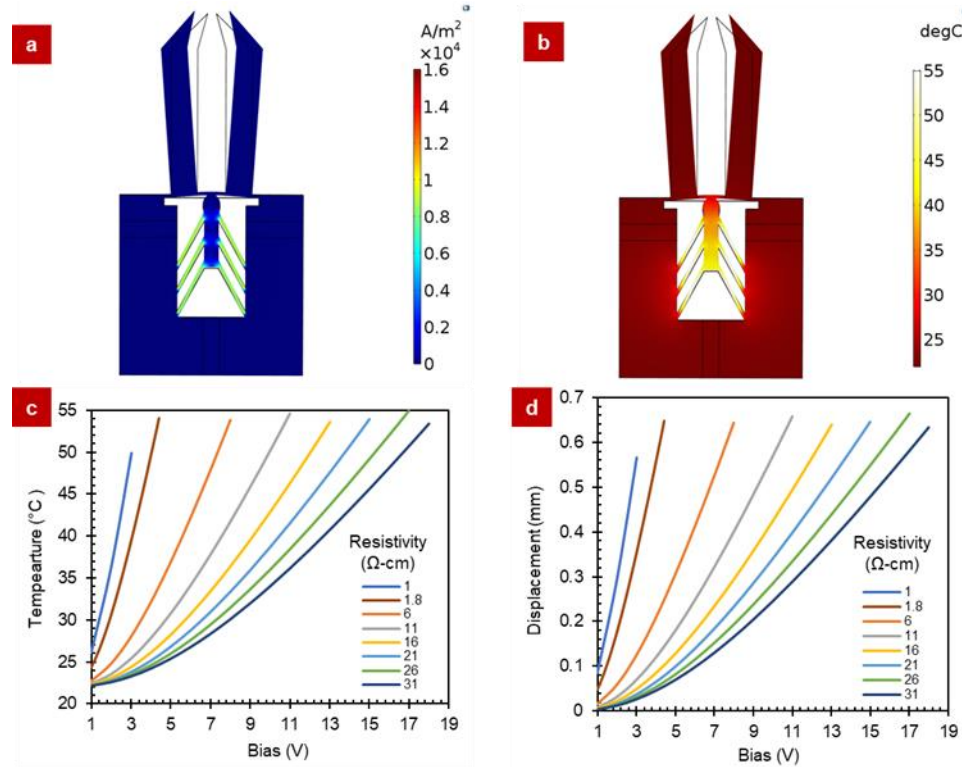


**Figure 5-2:** Gripper actuation demonstrated with steady-state solution. (a) Distribution of current density ( $\text{A/m}^2$ ) and (b) temperature ( $^{\circ}\text{C}$ ) across the gripper with the resistivity of c-PLA set to  $1.8\text{ }\Omega\text{-cm}$  and an actuation voltage of  $4.5\text{ V}$ . The arm movement is exaggerated  $10\times$  to aid visualization. (c) The maximum temperature achieved with variation in bias applied across the gripper. (d) Maximum displacement achieved with variation in bias applied across the gripper. The different curves in (c) and (d) represent solutions when the resistivity of c-PLA was set to  $1\text{ }\Omega\text{-cm}$  – blue,  $1.8\text{ }\Omega\text{-cm}$  – brown,  $6\text{ }\Omega\text{-cm}$  – orange,  $11\text{ }\Omega\text{-cm}$  – grey,  $16\text{ }\Omega\text{-cm}$  – yellow,  $21\text{ }\Omega\text{-cm}$  – light blue,  $26\text{ }\Omega\text{-cm}$  – green, or  $31\text{ }\Omega\text{-cm}$  – navy blue.

As expected, with lower resistivity values, lower actuation voltages were required for the maximum temperature in the chevrons to reach  $T_g$  and thus the maximum tip displacement, as shown in **Figure 5-2c** and **Figure 5-2d**. Therefore, to use lower actuation voltages, it is important to 3D print the grippers with lower electrical resistivity.

The gripper in this study were designed to be three times larger than that described by Alblalaid *et al.* [102] to accommodate the print resolution of the printed used here, yet the maximum gripper tip displacement (0.5 mm) was more than three times. This is possible because c-PLA has a larger coefficient of thermal expansion ( $171.2 \times 10^{-6} / \text{K}$ ) compared to silicon ( $120 \times 10^{-6} / \text{K}$ ).

### 5.3.2 Multiphysics: Transient Analysis

Transient finite element modeling was performed to understand the response and recovery of the maximum temperature in the chevron and the tip displacement as they were actuated with different voltages as shown in **Figure 5-3**. As expected, larger actuation voltages increase the heating rate and shorten the time to reach the desired tip displacement, as shown in **Figure 5-3a-b**. This confirms that useful displacements with reasonable actuation voltages can be achieved within a short period. For example, a displacement of 0.5 mm was reached in less than 2 s with 13 V, which a few household batteries can provide when placed in a series. However, the use of higher actuation voltages for longer durations could lead to heating beyond  $T_g$ . Therefore, to prevent parts from melting, the actuation voltage for practical operation should be maximized while limiting the times for which it is applied. The above discussed steady-state and transient results were found to be promising and inspired us to verify it experimentally.

### 5.3.3 Experimental Analysis: Proof of Concept

Three identical actuators were tested experimentally; it was possible to actuate all three by applying a voltage across the samples. However, electric potential was required to actuate the grippers than that proposed by simulations; this can be attributed to the significantly higher resistance between metal and plastic conductors, and the difference in

relativity values between experimental and simulation results. Furthermore, we compared the performance of the three actuators. For each actuator, the electric potentials required to produce a maximum temperature of 45 °C in the chevrons within 15, 10, and 5 s were

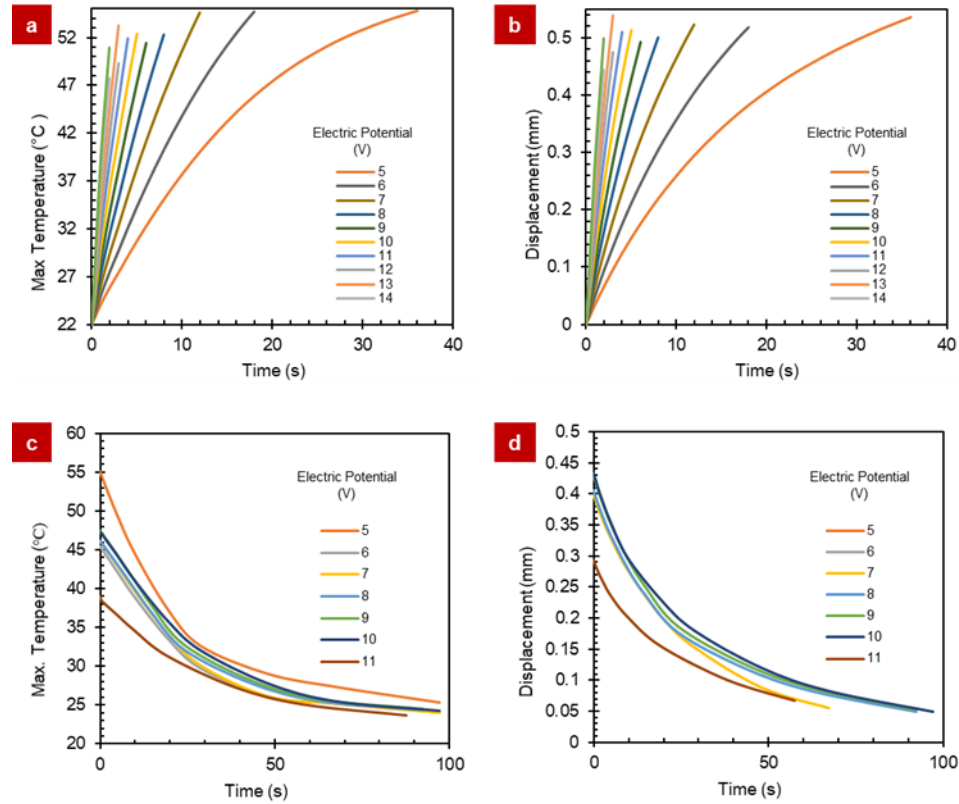


**Figure 5-3:** Transient simulation results for maximum temperature and displacement: (a) The maximum temperature in the chevrons, and (b) the tip displacement plot against time from when the potential was applied across the gripper. For (a) and (b), 5 V – orange, 6 V – dark grey, 7 V – brown, 8 V – navy blue, 9 V – green, 10 V – yellow, 11 V – light blue, 12 V – grey, 13 V – light orange, and 14 V – light grey. (c) The maximum temperature and (d) tip displacement plot against time from when the potential was turned off across the gripper after being heated to 45 °C using different voltages. For (c) and (d), 5V – orange, 6V – grey, 7V – yellow, 8V – blue, 9V – green, 10V – navy blue. Resistivity of c-PLA was set to 1.8  $\Omega$ -cm at 300 K.

were determined by trial and error. For example, in the case of actuator S1, it was found that 12.7, 13.8, and 17.9 V were required to reach a maximum temperature of 45 °C in the chevrons within 15, 10, and 5s, respectively, as shown in **Figure 5-4(d-f)** and the

corresponding tip displacements in the horizontal direction were recorded as shown in **Figure 5-4(a-c)**. A consistency was observed between maximum displacement and the corresponding temperature. A delay of 30 s between change in temperature and tip displacement seen in **Figure 5-4** was purposefully programmed into the experimental steps (see methods section above). Also, a variation was observed between the electric potential required amongst the different actuators to achieve a temperature close to 45 °C in the chevrons and the resulting tip displacement. This variation can be attributed to the differences in resistance of the 3D printed actuators and the residual stress in their mechanical structure. Regardless, the actuation time to reach 45 °C in the chevrons was found proportional to  $V_n$ , where  $n$  was between 2 and 2.5.

According to the transient simulations, the tip displacements achieved when the chevrons hit 45 °C were found constant irrespective of the actuation voltage. For example, as show in **Figure 5-3**, 5 V produces a tip displacement of ~341  $\mu\text{m}$  in 15 s, 6 V produces a tip displacement of ~357  $\mu\text{m}$  in 10 s, and 8 V produces a tip displacement of 353  $\mu\text{m}$  in 5 s. Experimentally, by comparing the tip displacements for 15 s and 5 s actuations, the faster actuations showed a smaller displacement. For instance, with the S1 actuator, when 12.7 V was applied for actuation in 15 s, a displacement of  $120.04 \pm 6.16$   $\mu\text{m}$  was obtained, but when 13.8 V and 17.9 V were applied for actuation in 10 s and 5 s, a displacement of  $97.05 \pm 6.81$  and  $88.86 \pm 6.16$   $\mu\text{m}$  was obtained, respectively.

To investigate this, the temperature profile during heating was investigated further. For differential actuation potentials, the temperature profile was found to be similar within the actuator when the maximum temperature in the chevrons was 45 °C (see **Figure 5-5**). Looking through the complete thermal camera recording, it was found



that the actuation in 15 s achieved a slightly higher temperature compared to when actuation was carried out in 5 s (see **Figure 5-6**). This explains the difference in tip displacement observed when actuation potentials varied.

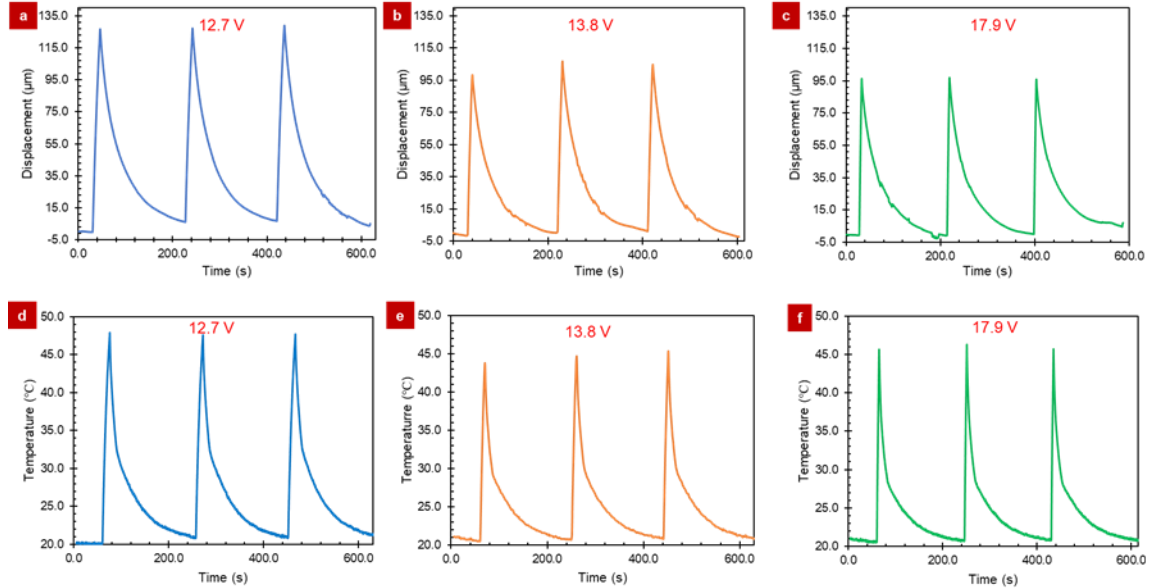


**Figure 5-4:** Displacement and temperature curve of the actuator (S1). (a) Tip displacement and (d) maximum temperature in the chevrons recorded when gripper was actuated using 12.7 V to achieve a response time of 15 s thrice (blue). Similarly, (b) tip displacement and (e) maximum temperature was obtained using 13.8 V to achieve a response time of 10 s (orange), and (c) tip displacement and (f) maximum temperature was obtained using 17.9 V to achieve a response time of 5 s (green).

To improve the simulations, the following things were are noted: (1) The displacements observed experimentally were smaller compared to simulation; this suggests that simulations were carried out with overestimated coefficient of thermal expansion. (2) The simulations predicted recovery times between 60 to 100 s, while experimentally recovery times were close to 180 s. This suggests simulations were done with overestimated coefficient of natural convection.

### 5.3.4 Hysteresis Study

Hysteresis can be a major issue in actuators. Here, the hysteresis in the 3D printed electro thermal actuators was analyzed by plotting the tip displacement against the maximum temperature observed in the chevron as shown in **Figure 5-12**.

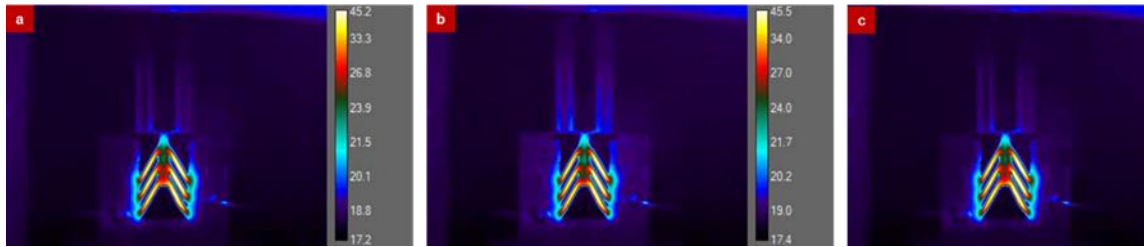


**Figure 5-5:** Temperature distribution at 45 °C for S3 with (a) 11.5 V, (b) 13.0 V, and (c) 17.5 V.

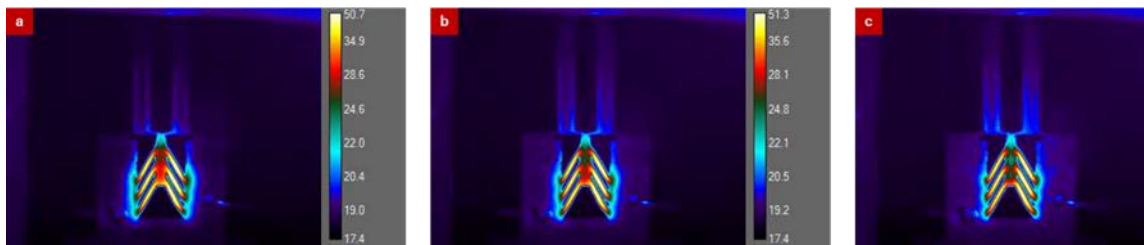


**Figure 5-6:** Maximum temperature overshoot observed for S3 with (a) 11.5 V, (b) 13.0 V, and (c) 17.5 V. Presented video frame observed right before turning off the power supply.

The tip displacement was found to be a linear function of the maximum temperature during actuation, as shown by red, green, or yellow circles in **Figure 5-7**. The linear trend of sensors S2 and S3 are shown in **Figure 5-8**, **Figure 5-9**, and **Figure 5-10**, respectively.

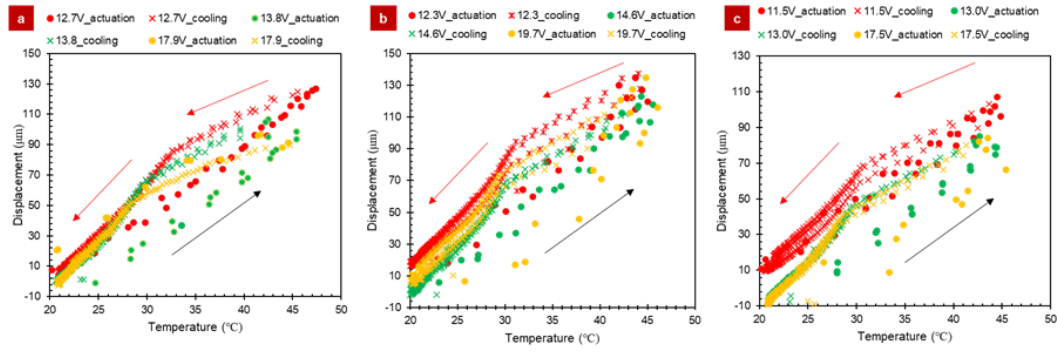


**Figure 5-7:** Hysteresis in electro thermal actuation. Displacement of single arm is plotted against the maximum temperature observed in the chevron of actuators (a) S1, (b) S2, and (c) S3. The solid circles denote the actuation (heating or opening) of the tweezer. The red, green, and yellow markers denote data when the tweezer was opened with response times of 15, 10, and 5 s, respectively. The corresponding voltages are annotated in the legend. The crosses denote the recovery (cooling or closing) of the tweezer for the corresponding actuation voltage and response times. The black arrow points to the trend in the actuation cycle and the red arrows point to the trend during the cooling cycle.

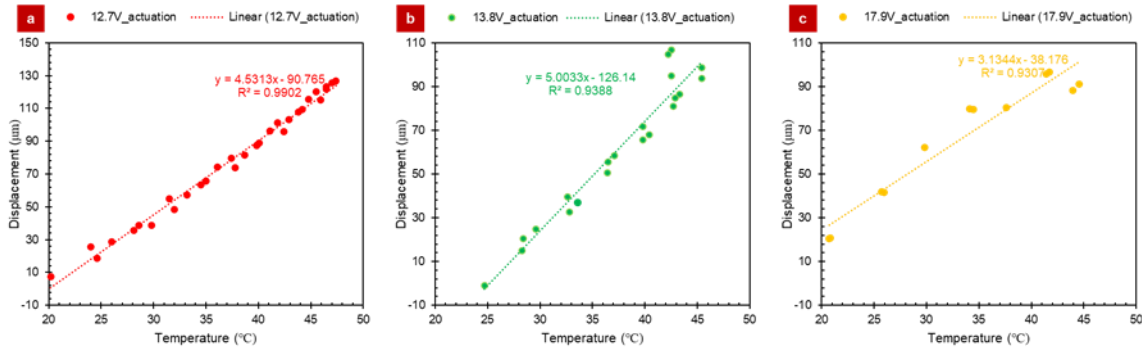


**Figure 5-8:** Linear trends in actuation for sensor S1. a) actuation in 15 s with a potential of 12.7 V, b) actuation in 10 s with a potential of 13.8 V, and c) actuation in 5 s with a potential of 17.9 V.

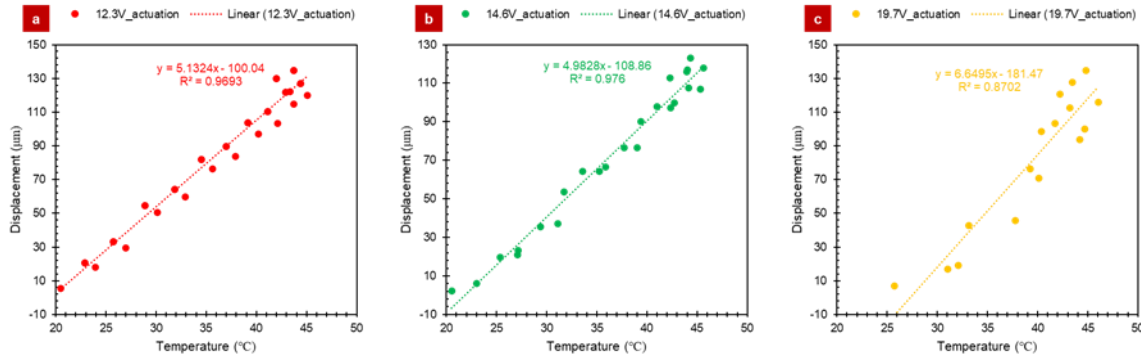


**Figure 5-9:** Linear trends in actuation for sensor S2. a) actuation in 15 s with a potential of 12.3 V, b) actuation in 10 s with a potential of 14.6 V, and c) actuation in 5 s with a potential of 19.7 V.

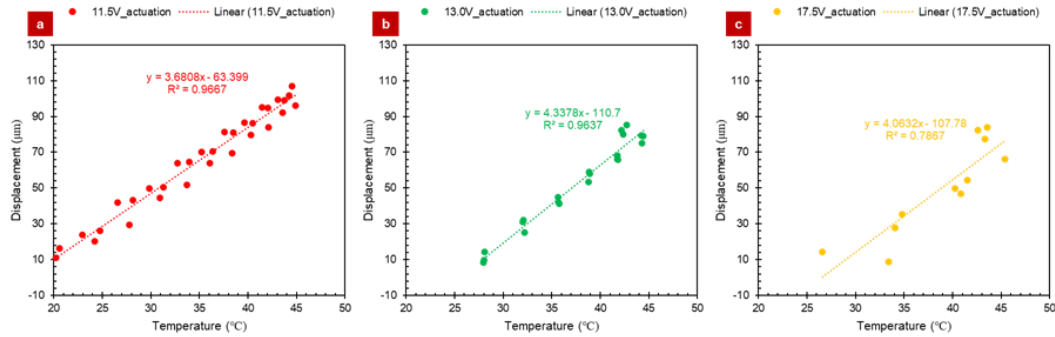


**Figure 5-10:** Linear trends in actuation for sensor S3. a) actuation in 15 s with a potential of 11.5 V, b) actuation in 10 s with a potential of 13.0 V, c) actuation in 5 s with a potential of 17.5 V.

The closing of the gripper during cooling depends on the primary mechanism of the heat conduction. In the case of chevrons, the Biot number ( $Bi = hL/k = 10 \text{ W m}^{-2} \text{ K}^{-1} * 0.011 \text{ m} / 0.366 \text{ W m}^{-1} \text{ K}^{-1}$ ) calculates to be 0.3, which indicates that the conduction of heat would be the primary mechanism of cooling. However, during cooling, the change in tip displacement with maximum temperature takes place in two distinct linear stages, with the second linear stage steeper than the first stage. The occurrence of two stages has to do with the thermal lag imposed by the thermal mass of the shuttle. When the cooling process begins, the maximum temperature, which is usually observed in the chevron,

drops quickly with the heat flowing to the shuttle and the body. The heat flow to the shuttle causes its thermal expansion as shown in **Figure 5-11**, thus reducing the rate at which the gripper closes. Hence, a difference is observed in the initial rate at which temperature and tip displacement decreases with time in **Figure 5-4**.

### 5.3.5 Application

Assuming the displacement of both arms of the gripper to be symmetrical, the total opening between the arms can be calculated as twice that of the tip displacement measured here. Tip displacements of  $\sim 90\ \mu\text{m}$  were achieved within 5 s. This translates to an opening of  $180\ \mu\text{m}$  between the arms. Though the gripper was not designed for a

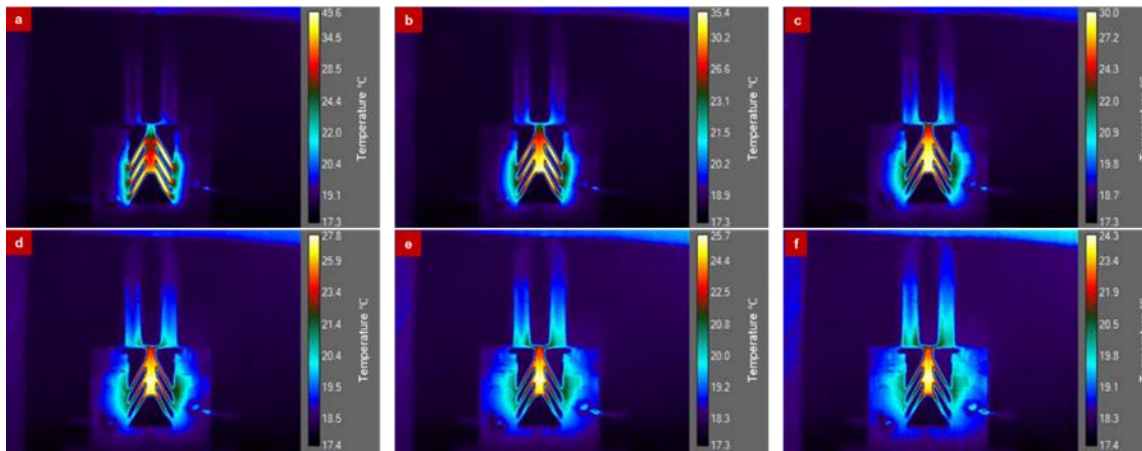


**Figure 5-11:** Thermal imaging of sample for S3 (a) at the beginning of the cooling phase, (b) 60 s into the cooling phase, and (c) 120 s into the cooling phase.

specific application, with the displacement that was achievable with the restrictions that were placed on the gripper, the gripper is foreseen to be used for handling glass beads [125], optical fibers [126], biological cells [127], and micro manipulation (i.e., a switch within an electrical system) [128].

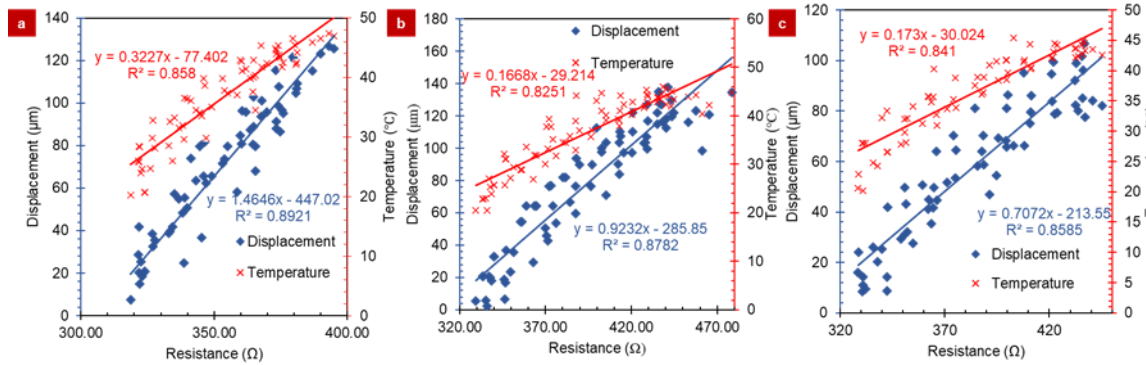


**Figure 5-12:** Displacement and temperature plotted against resistance for S1 (a), S2 (b), and S3 (c). Blue diamond represents displacement and the red crosses represent temperature.

A calibration graph was created by plotting the displacement and temperature against the resistance (**Figure 5-12**). As expected, there was a linear relationship between the displacement/temperature and the resistance. The calibration curves for all three sensors were plotted. The variation of the displacement with respect to the temperature shows a slope ranging from  $0.71 - 1.46 \mu\text{m}/\Omega$  and the temperature varies at a rate ranging from  $0.16 - 0.32 \text{ }^\circ\text{C}/\Omega$ . Independent of the voltage that was applied to the sensors, a linear relationship between resistance and displacement/temperature was observed as shown in **Figure 5-12**. Such a calibration curve would be unique to each actuator and could potentially be used for measuring the maximum temperature in the chevrons as opposed to a thermal camera such as that used in this study. Further, the resistance value could be used to avoid the temperatures in the chevrons from exceeding the  $T_g$  of the composite.

## 5.4 Conclusion

This study involves the fabrication of a MEAM chevron gripper inspired by MEMS design; the novelty of the study is to attempt a gripper that is electrothermally

actuated. Simulations helped validate the feasibility of the design prior to fabrication and characterization. Steady-state finite element analysis indicated that an increase in resistivity directly increased the required voltage for a fixed tip displacement or reduced the tip displacement for a given voltage, which indicated that part print settings would play a big role in tip displacement and actuation voltage. Transient finite element analysis showed that long recovery times, close to 120 seconds, were needed regardless of the actuation times ranging from 5 to 20 seconds.

Experimentally, the 3D printed gripper made with commercially available PLA-carbon black composite was able to achieve tip displacements of  $77.51 - 117.4 \mu\text{m}$  within 5 seconds for actuation voltages of  $17.5 - 19.5 \text{ V}$ . The simulation predicted that such displacements could be produced with voltages as low as  $3 \text{ V}$  that the discrepancy was found due to the difference in overall part resistance, coefficient of thermal expansion, and coefficient of convection. When tip displacement was plotted against the temperature, hysteresis was observed. The displacement varied linearly with respect to the temperature, but during recovery, there were two stages of linear cooling. The linear variation of the tip displacement with respect to the temperature points to a successful demonstration that the gripper works in accordance with the principles of linear thermal expansion. The two stages of recovery suggest that there could be a thermal lag between the tip displacement and the temperature of the shuttle, which must be overcome.

Furthermore, the thermal imaging of the gripper showed the cooling was faster during the initial 30 s and slowed down during the last 120 seconds. Overall, as with many soft actuators that are 3D printed, MEAM makes it extremely simple to design and fabricate. Future work can reduce the recovery time by optimizing the designing of a

shuttle with low thermal mass with faster cooling characteristics. Electro thermal actuation of MEAM grippers as studied here can be developed further for soft actuators with the introduction of more movable parts to increase the degree of freedom. With the ever-increasing resolution of MEAM technology and introduction of new materials, our work introduces actuators, which are faster and require less wiring/tubing. In conclusion, our work moves new pathways for hybrid, soft-rigid grippers that can be used for micromanipulation and in miniaturizing actuators that are 3D printed.



## **CHAPTER 6**

### **CONCLUSIONS AND FUTURE WORK**

#### **6.1 Conclusions**

Here, conductive filaments were characterized to enable sensors and actuators that are fabricated via MEAM. Two different commercially available conductive filament were characterized and use the most suitable filament for the fabrication of sensors and actuators was determined. The anisotropy in electrical impedance along and across the direction of the print was also studied. The role of interface in the anisotropy was examined. Our work will make a considerable impact in additive manufacturing as evidenced by four high quality publications resulting from this work.

First, the resistivity ( $\rho$ ) and temperature coefficient of resistance ( $\alpha$ ) for graphene PLA and carbon black PLA (c-PLA) was determined by performing impedance spectroscopy inside a convection oven. The c-PLA had a resistivity of 2.2-1.4  $\Omega$ -cm and  $\alpha$  between 0.03 and 0.01  $^{\circ}\text{C}^{-1}$ . In addition to comparable resistivity and temperature coefficient of resistance values comparable to its metal counterparts, a linear relationship was observed between resistance and temperature in the case of c-PLA. The study shows that c-PLA is more suitable for MEAM circuits, sensors, and actuators. The study of the microstructure also indicates that the reason for the presence of carbon black particles embedded in the polymer matrix within the percolation limits.

Secondly, from the above study with c-PLA, a hot-wire anemometer was fabricated to detect the flow of nitrogen through a channel. The flowmeter showed a flow sensitivity between  $0.014 - 0.032 \text{ sscm}^{-1}$  when operated at 12 V and  $0.039 - 0.065 \text{ sscm}^{-1}$  when operated at 15 V. The study shows that it is possible to fabricate a flowmeter that is completely MEAM. Because it was operable with voltages between 12 – 15 V with reasonable sensitivities, a functional flowmeter can be operated with household batteries.

Thirdly, a MEMS-inspired a robot end effector, which is actuated electrothermally designed and studied. Experimentally, a tip displacement of  $77.51 - 117.4 \text{ }\mu\text{m}$  was achieved within 5 seconds for voltages between 17.5 – 19.5 V. The discrepancies between the simulation and experimental values can be resolved by using accurate values of coefficient of thermal expansion and coefficient of convection. Using the work, the linear thermal expansion was shown to be used to fabricate a complete MEAM robot end effector. As with the flowmeter, here too, the nature of operational voltage show that they can be operated with household batteries.

Finally, the electrical properties of a single extrusion-wide wall were characterized. The study shows the anisotropy between the F- and Z- specimen with the resistance always being higher for Z- specimen compared to the F- specimen irrespective of the print speed. Examining both F- and Z-specimen show that the resistance of the “core” of any printed layer is lower than the resistance at the interfaces. This difference is an important insight that will allow for more accurate modeling and prediction in the future. Another insight provided by the study is the print speed did not influence the resistance of the sample as much as the temperature did as shown by the calculated p-values. It was also found that the impedance of the printed samples scaled linearly with

the number of interfaces and the slope was dependent on the extrusion temperature rather than the speed. It, therefore, can be deduced that the resistance can be optimized by simply varying the print temperature.

## **6.2 Future Work Recommendation**

The work presented here is novel and holds great potential for further optimization and development. The flowmeter discussed in Chapter 3 was designed to sense the flow of nitrogen gas at room temperature (20 °C). Further work is needed to understand the nitrogen temperature. Future work can consider the following questions: how would the anemometer perform if other gases are used? Would the signal-to-noise ratio improve if the design was modified to utilize differential hot-wire anemometer? Can the sensitivity of the anemometer be improved if the surface area of the hot-wire was increased?

The gripper discussed in Chapter 4 was successful in bringing MEMS-inspired design and electro thermal actuation for soft robotic applications. The time required for the actuator from being actuated to the point of returning to its default position is approximately 120 seconds. From studying the heat distribution, it was clear that the chevrons cooled conceivably faster than the shuttle because of smaller volumes of the chevrons. Changing the volume ratio between the chevron and shuttle would reduce the recovery time. Apart from being used as a robot end effector, the gripper can also be used for other electrical applications like switching. Furthermore, the gripper can be made to move inward by inverting the chevrons and the shuttle.

The characterization of the interface and anisotropy discussed in Chapter 5 was originally designed for appropriation of VOLCO: a MATLAB based code that simulates

and predicts mechanical performance of MEAM parts. The results show that the “core” of each layer exhibit lower resistance (or impedance) in comparison to the interface.

There are three directions these conclusions can lead research in the coming year: 1) the VOLCO code can be improved further to differentiate voxels that are considered “core” or interface. Once the distinction has been made, the “core” can be assigned with different electrical properties (i.e., half the resistance) than the interfaces. Subsequently, finite element modeling (FEM) can be used to predict the electrical performance of the MEAM parts; 2) though the study was intentionally kept simple to focus on a few print variables, having more data for variable layer heights and widths would provide more characterization; 3) the current studies are inconclusive about the reason for the high impedance at the interface, but it is open for further investigation. The current work contributes the field of additive manufacturing by enabling the fabrication of sensors and actuators completely via MEAM. The baseline experimental study for future researchers to develop VOLCO into a program that can predict electrical performance of MEAM parts for complex structures is provided through the study.

## BIBLIOGRAPHY

- [1] W. E. Forum, "A New Circular Vision for Electronics," United Nations, Switzerland, 01/2019 2019, vol. *Platform for Accelerating the Circular Economy*.
- [2] S. Danforth, "Fused Deposition of Ceramics: A New Technique for the Rapid Fabrication of Ceramic Components," *Materials Technology*, vol. 10, no. 7-8, pp. 144-146, 1995.
- [3] W. Macy and J. Orrock, "Engineering Product Solutions Enabled by Fused Deposition Modeling," in *International SAMPE Technical Conference*, 2013, pp. 44-58.
- [4] L. Novakova-Marcincinova and J. Novak-Marcincin, "Applications of Rapid Prototyping Fused Deposition Modeling Materials," in *Annals of DAAAM for 2012 & Proceedings of the 23rd International DAAAM Symposium*, 2012, vol. 23, no. 1, pp. 2304-1382.
- [5] M. Bahri, M. M. Hussain, T. Brahimi, and H. Dahrouj, "FDM 3D Printed Coffee Glove Embedded with Flexible Electronic," in *2017 Learning and Technology Conference (L&T)-The MakerSpace: from Imagining to Making!*, 2017: IEEE, pp. 49-53.
- [6] M. Brunelle, I. Ferralli, R. Whitsitt, and K. Medicus, "Current Use and Potential of Additive Manufacturing for Optical Applications," in *Optifab 2017*, 2017, vol. 10448: International Society For Optics And Photonics, p. 104480P.
- [7] J. F. Christ, N. Aliheidari, A. Ameli, and P. Pötschke, "3D Printed Highly Elastic Strain Sensors of Multiwalled Carbon Nanotube/Thermoplastic Polyurethane Nanocomposites," *Materials & Design*, vol. 131, pp. 394-401, 2017.
- [8] O. Diegel, S. Singamneni, B. Huang, and I. Gibson, "The Future of Electronic Products: Conductive 3D Printing?," in *Innovative Developments in Design and Manufacturing*: CRC Press, 2009, pp. 415-422.
- [9] G. L. Goh *et al.*, "Additively Manufactured Multi-Material Free-Form Structure with Printed Electronics," *The International Journal of Advanced Manufacturing Technology*, vol. 94, no. 1, pp. 1309-1316, 2018.
- [10] N. Tan, X. Gu, and H. Ren, "Design, Characterization and Applications of a Novel Soft Actuator Driven by Flexible Shafts," *Mechanism and Machine Theory*, vol. 122, pp. 197-218, 2018.

- [11] S. Aslanzadeh, H. Saghlatoon, M. M. Honari, R. Mirzavand, C. Montemagno, and P. Mousavi, "Investigation on Electrical and Mechanical Properties of 3D Printed Nylon 6 for RF/Microwave Electronics Applications," *Additive Manufacturing*, vol. 21, pp. 69-75, 2018.
- [12] D. Cadman, S. Zhang, and Y. Vardaxoglou, "Fused Deposition Modelling for Microwave Circuits & Antennas," in *2016 International Symposium on Antennas and Propagation (ISAP)*, 2016: IEEE, pp. 418-419.
- [13] I. T. Nassar, H. Tsang, K. Church, and T. M. Weller, "A High Efficiency, Electrically-Small, 3-D Machined-Substrate Antenna Fabricated with Fused Deposition Modeling and 3-D Printing," in *2014 IEEE Radio and Wireless Symposium (RWS)*, 2014: IEEE, pp. 67-69.
- [14] E. A. Rojas-Nastrucci, R. Ramirez, D. Hawatmeh, D. Lan, J. Wang, and T. Weller, "Laser Enhanced Direct Print Additive Manufacturing for mm-wave Components and Packaging," in *2017 International Conference on Electromagnetics in Advanced Applications (ICEAA)*, 2017: IEEE, pp. 1531-1534.
- [15] G. Gaal *et al.*, "Simplified Fabrication of Integrated Microfluidic Devices Using Fused Deposition Modeling 3D Printing," *Sensors and Actuators B: Chemical*, vol. 242, pp. 35-40, 2017.
- [16] D. Helmer, A. Voigt, S. Wagner, and B. Rapp, "Rapid Printing in PDMS-Fused Deposition Modeling (FDM) Meets Microfluidics," in *20th International Conference on Miniaturized Systems for Chemistry and Life Sciences. MicroTAS*, 2016, vol. 2016, pp. 168-169.
- [17] F. Li, N. P. Macdonald, R. M. Guijt, and M. C. Breadmore, "Using Printing Orientation for Tuning Fluidic Behavior in Microfluidic Chips Made by Fused Deposition Modeling 3D Printing," *Analytical chemistry*, vol. 89, no. 23, pp. 12805-12811, 2017.
- [18] A. M. Tothill, M. Partridge, S. W. James, and R. P. Tatam, "Fabrication and Optimisation of a Fused Filament 3D-Printed Microfluidic Platform," *Journal of Micromechanics and Microengineering*, vol. 27, no. 3, p. 035018, 2017.
- [19] H. Wang, S. Masood, P. Iovenitti, and E. C. Harvey, "Application of Fused Deposition Modeling Rapid Prototyping System to the Development of Microchannels," In *Biomems And Smart Nanostructures*, 2001, vol. 4590: International Society for Optics and Photonics, pp. 213-220.

- [20] B. W. Ang and C.-H. Yeow, "Print-It-Yourself (PIY) Glove: A Fully 3D Printed Soft Robotic Hand Rehabilitative and Assistive Exoskeleton for Stroke Patients," in *2017 IEEE/RSJ International Conference on Intelligent Robots and Systems (IROS)*, 2017: IEEE, pp. 1219-1223.
- [21] H. Candiotti *et al.*, "Fused Deposition Modeling Bioprinter," in *2013 39th Annual Northeast Bioengineering Conference*, 2013: IEEE, pp. 177-178.
- [22] J. S. Chohan, R. Singh, K. S. Boparai, R. Penna, and F. Fraternali, "Dimensional Accuracy Analysis of Coupled Fused Deposition Modeling and Vapour Smoothing Operations for Biomedical Applications," *Composites Part B: Engineering*, vol. 117, pp. 138-149, 2017.
- [23] E. Jabbari, D. N. Rocheleau, W. Xu, and X. He, "Fabrication of Biomimetic Scaffolds with Well-Defined Pore Geometry by Fused Deposition Modeling," in *International Manufacturing Science and Engineering Conference*, 2007, vol. 42908, pp. 71-76.
- [24] L. Konieczna, M. Belka, M. Okońska, M. Pyszka, and T. Bączek, "New 3D-Printed Sorbent for Extraction of Steroids from Human Plasma Preceding LC–MS Analysis," *Journal of Chromatography A*, vol. 1545, pp. 1-11, 2018.
- [25] G. I. Salentijn, P. E. Oomen, M. Grajewski, and E. Verpoorte, "Fused Deposition Modeling 3D Printing for (Bio) Analytical Device Fabrication: Procedures, Materials, And Applications," *Analytical chemistry*, vol. 89, no. 13, pp. 7053-7061, 2017.
- [26] M. Cader, "The Estimation Method of Strength for Technology-Oriented 3D Printing Parts of Mobile Robots," in *International Conference Automation*, 2017: Springer, pp. 367-379.
- [27] H. Klippstein, A. Diaz De Cerio Sanchez, H. Hassanin, Y. Zweiri, and L. Seneviratne, "Fused Deposition Modeling For Unmanned Aerial Vehicles (Uavs): A Review," *Advanced Engineering Materials*, vol. 20, no. 2, p. 1700552, 2018.
- [28] Y. Yang, Y. Chen, Y. Li, and M. Z. Chen, "3D Printing of Variable Stiffness Hyper-Redundant Robotic Arm," in *2016 IEEE International Conference on Robotics and Automation (ICRA)*, 2016: IEEE, pp. 3871-3877.
- [29] X. Wei *et al.*, "3D Printable Graphene Composite," *Scientific reports*, vol. 5, no. 1, pp. 1-7, 2015.
- [30] S. W. Kwok *et al.*, "Electrically Conductive Filament for 3D-Printed Circuits and Sensors," *Applied Materials Today*, vol. 9, pp. 167-175, 2017.

- [31] Y.-H. Lin, C.-Y. Yang, S.-F. Lin, and G.-R. Lin, "Triturating Versatile Carbon Materials as Saturable Absorptive Nano Powders for Ultrafast Pulsating of Erbium-Doped Fiber Lasers," *Optical Materials Express*, vol. 5, no. 2, pp. 236-253, 2015.
- [32] S. Reich and C. Thomsen, "Raman Spectroscopy Of Graphite," *Philosophical Transactions of the Royal Society of London. Series A: Mathematical, Physical and Engineering Sciences*, vol. 362, no. 1824, pp. 2271-2288, 2004.
- [33] A. Kiraly and F. Ronkay, "Temperature Dependence of Electrical Properties in Conductive Polymer Composites," *Polymer Testing*, vol. 43, pp. 154-162, 2015.
- [34] S. C. Joshi and A. A. Sheikh, "3D Printing In Aerospace and its Long-Term Sustainability," *Virtual and Physical Prototyping*, vol. 10, no. 4, pp. 175-185, 2015.
- [35] G.-S. Park, S.-K. Kim, S.-J. Heo, J.-Y. Koak, and D.-G. Seo, "Effects of Printing Parameters on The Fit of Implant-Supported 3D Printing Resin Prosthetics," *Materials*, vol. 12, no. 16, p. 2533, 2019.
- [36] A. Dawood, B. M. Marti, V. Sauret-Jackson, and A. Darwood, "3D Printing in Dentistry," *British Dental Journal*, vol. 219, no. 11, pp. 521-529, 2015.
- [37] Y. Xu *et al.*, "The Boom in 3D-Printed Sensor Technology," *Sensors*, vol. 17, no. 5, p. 1166, 2017.
- [38] M. Saari, B. Xia, B. Cox, P. S. Krueger, A. L. Cohen, and E. Richer, "Fabrication and Analysis of a Composite 3D Printed Capacitive Force Sensor," *3D Printing and Additive Manufacturing*, vol. 3, no. 3, pp. 136-141, 2016.
- [39] C. Shemelya *et al.*, "Encapsulated Copper Wire and Copper Mesh Capacitive Sensing for 3-D Printing Applications," *IEEE Sensors Journal*, vol. 15, no. 2, pp. 1280-1286, 2014.
- [40] M. Bodnicki, P. Pakuła, and M. Zowade, "Miniature Displacement Sensor," in *Advanced Mechatronics Solutions*: Springer, 2016, pp. 313-318.
- [41] E. Macdonald *et al.*, "3D Printing for the Rapid Prototyping Of Structural Electronics," *IEEE Access*, vol. 2, pp. 234-242, 2014.
- [42] J. van Tiem, J. Groenesteijn, R. Sanders, and G. Krijnen, "3D Printed Bio-Inspired Angular Acceleration Sensor," in *2015 IEEE SENSORS*, 2015: IEEE, pp. 1-4.
- [43] Y. Kim and K. Kim, "Near-Field Sound Localization based on the Small Profile Monaural Structure," *Sensors*, vol. 15, no. 11, pp. 28742-28763, 2015.



- [44] S.-Y. Wu, C. Yang, W. Hsu, and L. Lin, "RF Wireless LC Tank Sensors Fabricated by 3D Additive Manufacturing," in *2015 Transducers-2015 18th International Conference on Solid-State Sensors, Actuators and Microsystems (TRANSDUCERS)*, 2015: IEEE, pp. 2208-2211.
- [45] K. Kadimisetty *et al.*, "3D-Printed Supercapacitor-Powered Electrochemiluminescent Protein Immunoarray," *Biosensors and Bioelectronics*, vol. 77, pp. 188-193, 2016.
- [46] M. E. Staymates *et al.*, "Biomimetic Sniffing Improves the Detection Performance of a 3D Printed Nose of a Dog and a Commercial Trace Vapor Detector," *Scientific reports*, vol. 6, no. 1, pp. 1-10, 2016.
- [47] S. Leigh, C. Purssell, D. Billson, and D. Hutchins, "Using a Magnetite/Thermoplastic Composite in 3D Printing of Direct Replacements for Commercially Available Flow Sensors," *Smart Materials and Structures*, vol. 23, no. 9, p. 095039, 2014.
- [48] S. Krachunov and A. J. Casson, "3D Printed Dry EEG Electrodes," *Sensors*, vol. 16, no. 10, p. 1635, 2016.
- [49] I. Nassar, H. Tsang, and T. Weller, "3D Printed Wideband Harmonic Transceiver for Embedded Passive Wireless Monitoring," *Electronics Letters*, vol. 50, no. 22, pp. 1609-1611, 2014.
- [50] M. F. Afrose, S. Masood, P. Iovenitti, M. Nikzad, and I. Sbarski, "Effects of Part Build Orientations on Fatigue Behaviour Of FDM-Processed PLA Material," *Progress in Additive Manufacturing*, vol. 1, no. 1, pp. 21-28, 2016.
- [51] J. T. Cantrell *et al.*, "Experimental Characterization of the Mechanical Properties of 3D-Printed ABS and Polycarbonate Parts," *Rapid Prototyping Journal*, 2017.
- [52] J. Chacón, M. A. Caminero, E. García-Plaza, and P. J. Núñez, "Additive Manufacturing of PLA Structures using Fused Deposition Modelling: Effect of Process Parameters on Mechanical Properties and their Optimal Selection," *Materials & Design*, vol. 124, pp. 143-157, 2017.
- [53] I. Durgun and R. Ertan, "Experimental Investigation of FDM Process for Improvement of Mechanical Properties and Production Cost," *Rapid Prototyping Journal*, 2014.
- [54] B. Rankouhi, S. Javadpour, F. Delfanian, and T. Letcher, "Failure Analysis and Mechanical Characterization of 3D Printed ABS with Respect to Layer Thickness and Orientation," *Journal of Failure Analysis and Prevention*, vol. 16, no. 3, pp. 467-481, 2016.

- [55] Y. Song, Y. Li, W. Song, K. Yee, K.-Y. Lee, and V. L. Tagarielli, "Measurements of the Mechanical Response of Unidirectional 3D-Printed PLA," *Materials & Design*, vol. 123, pp. 154-164, 2017.
- [56] A. K. Sood, R. K. Ohdar, and S. S. Mahapatra, "Parametric Appraisal of Mechanical Property of Fused Deposition Modelling Processed Parts," *Materials & Design*, vol. 31, no. 1, pp. 287-295, 2010.
- [57] B. Tymrak, M. Kreiger, and J. M. Pearce, "Mechanical Properties of Components Fabricated with Open-Source 3-D Printers under Realistic Environmental Conditions," *Materials & Design*, vol. 58, pp. 242-246, 2014.
- [58] W. Wu, P. Geng, G. Li, D. Zhao, H. Zhang, and J. Zhao, "Influence of Layer Thickness and Raster Angle on the Mechanical Properties of 3D-Printed PEEK and a Comparative Mechanical Study Between PEEK and ABS," *Materials*, vol. 8, no. 9, pp. 5834-5846, 2015.
- [59] A. M. Abdelrhman, W. W. Gan, and D. Kurniawan, "Effect of Part Orientation on Dimensional Accuracy, Part Strength, and Surface Quality of Three Dimensional Printed Part," in *IOP Conference Series: Materials Science and Engineering*, 2019, vol. 694, no. 1: IOP Publishing, p. 012048.
- [60] N. Aliheidari, R. Tripuraneni, A. Ameli, and S. Nadimpalli, "Fracture Resistance Measurement of Fused Deposition Modeling 3D Printed Polymers," *Polymer Testing*, vol. 60, pp. 94-101, 2017.
- [61] O. Lužanin, D. Movrin, and M. Plančak, "Effect of Layer Thickness, Deposition Angle, and Infill on Maximum Flexural Force in FDM-Built Specimens," *Journal for Technology of Plasticity*, vol. 39, no. 1, pp. 49-58, 2014.
- [62] T. E. Shelton, Z. A. Willburn, C. R. Hartsfield, G. R. Cobb, J. T. Cerri, and R. A. Kemnitz, "Effects of Thermal Process Parameters on Mechanical Interlayer Strength for Additively Manufactured Ultem 9085," *Polymer Testing*, vol. 81, p. 106255, 2020.
- [63] T. Tajareernmuang, C. Sawangrat, and S. Jomjunyong, "Effect of Process Parameters to Flexural Strength of 3D Printed Anatomical Bone Part," in *IOP Conference Series: Materials Science and Engineering*, 2019, vol. 635, no. 1: IOP Publishing, p. 012034.
- [64] M. Q. Tanveer, A. Haleem, and M. Suhaib, "Effect of Variable Infill Density on Mechanical Behaviour Of 3-D Printed PLA Specimen: An Experimental Investigation," *SN Applied Sciences*, vol. 1, no. 12, pp. 1-12, 2019.

- [65] J. Thomas and J. Rodríguez, "Modeling the Fracture Strength Between Fused-Deposition Extruded Roads 16," in *2000 International Solid Freeform Fabrication Symposium*, 2000.
- [66] S. Garzon-Hernandez, D. Garcia-Gonzalez, A. Jérusalem, and A. Arias, "Design of FDM 3D Printed Polymers: An Experimental-Modelling Methodology for the Prediction of Mechanical Properties," *Materials & Design*, vol. 188, p. 108414, 2020.
- [67] A. Gleadall, I. Ashcroft, and J. Segal, "VOLCO: A Predictive Model for 3D Printed Microarchitecture," *Additive Manufacturing*, vol. 21, pp. 605-618, 2018.
- [68] M. Roy, R. Yavari, C. Zhou, O. Wodo, and P. Rao, "Prediction and Experimental Validation of Part Thermal History in the Fused Filament Fabrication Additive Manufacturing Process," *Journal of Manufacturing Science and Engineering*, vol. 141, no. 12, 2019.
- [69] M. P. Serdeczny, R. Comminal, D. B. Pedersen, and J. Spangenberg, "Experimental Validation of a Numerical Model for the Strand Shape in Material Extrusion Additive Manufacturing," *Additive Manufacturing*, vol. 24, pp. 145-153, 2018.
- [70] M. P. Serdeczny, R. Comminal, D. B. Pedersen, and J. Spangenberg, "Numerical Simulations of the Mesostructure Formation in Material Extrusion Additive Manufacturing," *Additive Manufacturing*, vol. 28, pp. 419-429, 2019.
- [71] H. Xia, J. Lu, S. Dabiri, and G. Tryggvason, "Fully Resolved Numerical Simulations of Fused Deposition Modeling. Part I: Fluid Flow," *Rapid Prototyping Journal*, 2018.
- [72] H. Xia, J. Lu, and G. Tryggvason, "Fully Resolved Numerical Simulations of Fused Deposition Modeling. Part II–Solidification, Residual Stresses and Modeling of the Nozzle," *Rapid Prototyping Journal*, 2018.
- [73] T. J. Coogan and D. O. Kazmer, "Bond and Part Strength in Fused Deposition Modeling," *Rapid Prototyping Journal*, 2017.
- [74] J. Allum, A. Moetazedian, A. Gleadall, and V. V. Silberschmidt, "Interlayer Bonding has Bulk-Material Strength in Extrusion Additive Manufacturing: New Understanding of Anisotropy," *Additive Manufacturing*, vol. 34, p. 101297, 2020.
- [75] J. Zhang, B. Yang, F. Fu, F. You, X. Dong, and M. Dai, "Resistivity And its Anisotropy Characterization of 3D-Printed Acrylonitrile Butadiene Styrene Copolymer (ABS)/Carbon Black (CB) Composites," *Applied Sciences*, vol. 7, no. 1, p. 20, 2017.

- [76] F. Daniel, N. H. Patoary, A. L. Moore, L. Weiss, and A. D. Radadia, "Temperature-Dependent Electrical Resistance of Conductive Polylactic Acid Filament for Fused Deposition Modeling," *The International Journal of Advanced Manufacturing Technology*, vol. 99, no. 5, pp. 1215-1224, 2018.
- [77] J. Allum, A. Gleadall, and V. V. Silberschmidt, "Fracture of 3D-Printed Micro-Tensile Specimens: Filament-Scale Geometry-Induced Anisotropy," *Procedia Structural Integrity*, vol. 28, pp. 591-601, 2020.
- [78] J. Allum, J. Kitzinger, Y. Li, V. V. Silberschmidt, and A. Gleadall, "Zigzag: Improving Mechanical Performance in Extrusion Additive Manufacturing by Nonplanar Toolpaths," *Additive Manufacturing*, vol. 38, p. 101715, 2021.
- [79] A. Gleadall, "Fullcontrol Gcode Designer-Open Source Software for Unconstrained Design in Additive Manufacturing." *Additive Manufacturing*, 46, p.102109, 2021
- [80] M. Al-Rubaiai, T. Pinto, D. Torres, N. Sepulveda, and X. Tan, "Characterization of a 3D-Printed Conductive PLA Material With Electrically Controlled Stiffness," in *Smart Materials, Adaptive Structures and Intelligent Systems*, 2017, vol. 58257: American Society of Mechanical Engineers, p. V001T01A003.
- [81] M. I. M. Ghazali, S. Karuppuswami, S. Mondal, A. Kaur, and P. Chahal, "Embedded Actives using Additive Manufacturing for High-Density RF Circuits and Systems," *IEEE Transactions on Components, Packaging and Manufacturing Technology*, vol. 9, no. 8, pp. 1643-1651, 2019.
- [82] H. Watschke, K. Hilbig, and T. Vietor, "Design and Characterization of Electrically Conductive Structures Additively Manufactured by Material Extrusion," *Applied Sciences*, vol. 9, no. 4, p. 779, 2019.
- [83] R. Freund, H. Watschke, J. Heubach, and T. Vietor, "Determination of Influencing Factors on Interface Strength of Additively Manufactured Multi-Material Parts by Material Extrusion," *Applied Sciences*, vol. 9, no. 9, p. 1782, 2019.
- [84] P. F. Flowers, C. Reyes, S. Ye, M. J. Kim, and B. J. Wiley, "3D Printing Electronic Components and Circuits with Conductive Thermoplastic Filament," *Additive Manufacturing*, vol. 18, pp. 156-163, 2017.
- [85] K. B. Anderson, S. Y. Lockwood, R. S. Martin, and D. M. Spence, "A 3D Printed Fluidic Device that Enables Integrated Features," *Analytical Chemistry*, vol. 85, no. 12, pp. 5622-5626, 2013.

- [86] R. Tsukuda, S. Sumimoto, and T. Ozawa, "Thermal Conductivity and Heat Capacity of ABS Resin Composites," *Journal of Applied Polymer Science*, vol. 63, no. 10, pp. 1279-1286, 1997.
- [87] C. Shemelya *et al.*, "Anisotropy of Thermal Conductivity in 3D Printed Polymer Matrix Composites for Space Based Cube Satellites," *Additive Manufacturing*, vol. 16, pp. 186-196, 2017.
- [88] K. Tai, A.-R. El-Sayed, M. Shahriari, M. Biglarbegian, and S. Mahmud, "State of the Art Robotic Grippers and Applications," *Robotics*, vol. 5, no. 2, p. 11, 2016.
- [89] L. Chen, B. Liu, T. Chen, and B. Shao, "Design of Hybrid-Type MEMS Microgripper," in *2009 International Conference on Mechatronics and Automation*, 2009: IEEE, pp. 2882-2887.
- [90] C.-S. Jeon, J.-S. Park, S.-Y. Lee, and C.-W. Moon, "Fabrication and Characteristics of Out-Of-Plane Piezoelectric Micro Grippers using MEMS Processes," *Thin Solid Films*, vol. 515, no. 12, pp. 4901-4904, 2007.
- [91] O. Millet *et al.*, "Electrostatic Actuated Micro Gripper using an Amplification Mechanism," *Sensors and Actuators A: Physical*, vol. 114, no. 2-3, pp. 371-378, 2004.
- [92] Y. Zhao and T. Cui, "Fabrication of High-Aspect-Ratio Polymer-Based Electrostatic Comb Drives using the Hot Embossing Technique," *Journal of Micromechanics and Microengineering*, vol. 13, no. 3, p. 430, 2003.
- [93] M. Shikida, K. Sato, and T. Harada, "Fabrication of an S-Shaped Microactuator," *Journal of Microelectromechanical Systems*, vol. 6, no. 1, pp. 18-24, 1997.
- [94] R. Legtenberg, J. Gilbert, S. D. Senturia, and M. Elwenspoek, "Electrostatic Curved Electrode Actuators," *Journal of Microelectromechanical Systems*, vol. 6, no. 3, pp. 257-265, 1997.
- [95] R. Yeh, S. Hollar, and K. S. Pister, "Single Mask, Large Force, and Large Displacement Electrostatic Linear Inchworm Motors," *Journal of Microelectromechanical Systems*, vol. 11, no. 4, pp. 330-336, 2002.
- [96] Q. Zhang, S. Gross, S. Tadigadapa, T. Jackson, F. Djuth, and S. Trolrier-McKinstry, "Lead Zirconate Titanate Films For D33 Mode Cantilever Actuators," *Sensors and Actuators A: Physical*, vol. 105, no. 1, pp. 91-97, 2003.
- [97] S. Koganezawa, Y. Uematsu, T. Yamada, H. Nakano, J. Inoue, and T. Suzuki, "Dual-Stage Actuator System for Magnetic Disk Drives using a Shear Mode Piezoelectric Microactuator," *IEEE Transactions on Magnetics*, vol. 35, no. 2, pp. 988-992, 1999.

- [98] H. Sehr *et al.*, "Time Constant and Lateral Resonances of Thermal Vertical Bimorph Actuators," *Journal of Micromechanics and Microengineering*, vol. 12, no. 4, p. 410, 2002.
- [99] J. T. Butler, V. M. Bright, and W. D. Cowan, "Average Power Control and Positioning of Polysilicon Thermal Actuators," *Sensors and Actuators A: Physical*, vol. 72, no. 1, pp. 88-97, 1999.
- [100] D. J. Bell, T. Lu, N. A. Fleck, and S. M. Spearing, "MEMS Actuators and Sensors: Observations on their Performance and Selection for Purpose," *Journal of Micromechanics and Microengineering*, vol. 15, no. 7, p. S153, 2005.
- [101] R. Mackay, H. Le, S. Clark, and J. Williams, "Polymer Micro-Grippers with an Integrated Force Sensor for Biological Manipulation," *Journal of micromechanics and microengineering*, vol. 23, no. 1, p. 015005, 2012.
- [102] K. Alblalaih, J. Overton, S. Lawes, and P. Kinnell, "A 3D-Printed Polymer Micro-Gripper with Self-Defined Electrical Tracks and Thermal Actuator," *Journal of Micromechanics and Microengineering*, vol. 27, no. 4, p. 045019, 2017.
- [103] J. Morrow, S. Hemleben, and Y. Menguc, "Directly Fabricating Soft Robotic Actuators with an Open-Source 3-D Printer," *IEEE Robotics and Automation Letters*, vol. 2, no. 1, pp. 277-281, 2016.
- [104] T. Shahid, D. Gouwanda, and S. G. Nurzaman, "Moving Toward Soft Robotics: A Decade Review of the Design of Hand Exoskeletons," *Biomimetics*, vol. 3, no. 3, p. 17, 2018.
- [105] D. Drotman, M. Ishida, S. Jadhav, and M. T. Tolley, "Application-Driven Design of Soft, 3-D Printed, Pneumatic Actuators with Bellows," *IEEE/ASME Transactions on Mechatronics*, vol. 24, no. 1, pp. 78-87, 2018.
- [106] F. Giorgio-Serchi, A. Arienti, and C. Laschi, "Underwater Soft-Bodied Pulsed-Jet Thrusters: Actuator Modeling and Performance Profiling," *The International Journal of Robotics Research*, vol. 35, no. 11, pp. 1308-1329, 2016.
- [107] F. Ni, D. Rojas, K. Tang, L. Cai, and T. Asfour, "A Jumping Robot using Soft Pneumatic Actuator," in *2015 IEEE International Conference on Robotics and Automation (ICRA)*, 2015: IEEE, pp. 3154-3159.
- [108] S. Li, D. M. Vogt, D. Rus, and R. J. Wood, "Fluid-Driven Origami-Inspired Artificial Muscles," *Proceedings of the National academy of Sciences*, vol. 114, no. 50, pp. 13132-13137, 2017.

- [109] H. M. Anver, R. Mutlu, and G. Alici, "3D Printing of a Thin-Wall Soft and Monolithic Gripper using Fused Filament Fabrication," in *2017 IEEE International Conference on Advanced Intelligent Mechatronics (AIM)*, 2017: IEEE, pp. 442-447.
- [110] H. K. Yap, H. Y. Ng, and C.-H. Yeow, "High-Force Soft Printable Pneumatics for Soft Robotic Applications," *Soft Robotics*, vol. 3, no. 3, pp. 144-158, 2016.
- [111] F. Schmitt, O. Piccin, L. Barbé, and B. Bayle, "Soft Robots Manufacturing: A Review," *Frontiers in Robotics and AI*, vol. 5, p. 84, 2018.
- [112] M. Behl, K. Kratz, J. Zotzmann, U. Nöchel, and A. Lendlein, "Reversible Bidirectional Shape-Memory Polymers," *Advanced materials*, vol. 25, no. 32, pp. 4466-4469, 2013.
- [113] D. Zhang, O. J. George, K. M. Petersen, A. C. Jimenez-Vergara, M. S. Hahn, and M. A. Grunlan, "A Bioactive "Self-Fitting" Shape Memory Polymer Scaffold with Potential to Treat Cranio-Maxillo Facial Bone Defects," *Acta biomaterialia*, vol. 10, no. 11, pp. 4597-4605, 2014.
- [114] J. J. Hubbard, M. Fleming, V. Palmre, D. Pugal, K. J. Kim, and K. K. Leang, "Monolithic IPMC Fins For Propulsion and Maneuvering in Bioinspired Underwater Robotics," *IEEE Journal of Oceanic Engineering*, vol. 39, no. 3, pp. 540-551, 2013.
- [115] K. J. Kim, D. Pugal, and K. K. Leang, "A Twistable Ionic Polymer-Metal Composite Artificial Muscle for Marine Applications," *Marine Technology Society Journal*, vol. 45, no. 4, pp. 83-98, 2011.
- [116] V. Palmre *et al.*, "An IPMC-Enabled Bio-Inspired Bending/Twisting Fin for Underwater Applications," *Smart Materials and Structures*, vol. 22, no. 1, p. 014003, 2012.
- [117] S. Palagi *et al.*, "Structured Light Enables Biomimetic Swimming and Versatile Locomotion of Photoresponsive Soft Microrobots," *Nature materials*, vol. 15, no. 6, pp. 647-653, 2016.
- [118] H. Wermter and H. Finkelmann, "Liquid Crystalline Elastomers as Artificial Muscles," *e-Polymers*, vol. 1, no. 1, 2001.
- [119] T. J. White and D. J. Broer, "Programmable and Adaptive Mechanics with Liquid Crystal Polymer Networks and Elastomers," *Nature materials*, vol. 14, no. 11, pp. 1087-1098, 2015.

- [120] R. J. Wood, S. Avadhanula, R. Sahai, E. Steltz, and R. S. Fearing, "Microrobot Design using Fiber Reinforced Composites," *Journal of Mechanical Design*, vol. 130, no. 5, 2008.
- [121] K. Elgeneidy, G. Neumann, M. Jackson, and N. Lohse, "Directly Printable Flexible Strain Sensors for Bending and Contact Feedback of Soft Actuators," *Frontiers in Robotics and AI*, vol. 5, p. 2, 2018.
- [122] J. Bjorgaard, M. Hoyack, E. Huber, M. Mirzaee, Y.-H. Chang, and S. Noghianian, "Design and Fabrication of Antennas using 3D Printing," *Progress In Electromagnetics Research*, vol. 84, pp. 119-134, 2018.
- [123] J. Torres, J. Cotel, J. Karl, and A. P. Gordon, "Mechanical Property Optimization of FDM PLA in Shear with Multiple Objectives," *Jom*, vol. 67, no. 5, pp. 1183-1193, 2015.
- [124] R. V. Morgan, R. S. Reid, A. M. Baker, B. Lucero, and J. D. Bernardin, "Emissivity Measurements of Additively Manufactured Materials," Los Alamos National Lab.(LANL), Los Alamos, NM (United States), 2017.
- [125] A. Vasudev and J. Zhe, "A Capillary Microgripper Based on Electrowetting," *Applied Physics Letters*, vol. 93, no. 10, p. 103503, 2008.
- [126] D.-H. Kim, M. G. Lee, B. Kim, and Y. Sun, "A Superelastic Alloy Microgripper with Embedded Electromagnetic Actuators and Piezoelectric Force Sensors: A Numerical and Experimental Study," *Smart materials and structures*, vol. 14, no. 6, p. 1265, 2005.
- [127] R. Zhang, J. Chu, H. Wang, and Z. Chen, "A Multipurpose Electrothermal Microgripper for Biological Micro-Manipulation," *Microsystem technologies*, vol. 19, no. 1, pp. 89-97, 2013.
- [128] F. Wang, C. Liang, Y. Tian, X. Zhao, and D. Zhang, "Design And Control of a Compliant Microgripper with a Large Amplification Ratio for High-Speed Micro Manipulation," *IEEE/ASME Transactions on Mechatronics*, vol. 21, no. 3, pp. 1262-1271, 2016.